In-situ studies of delta-ferrite/austenite phase transformation in low carbon steels

Salar Niknafs
University of Wollongong

IN-SITU STUDIES OF DELTA-FERRITE/AUSTENITE PHASE TRANSFORMATION IN LOW CARBON STEELS

A thesis submitted in fulfilment of the
requirements for the degree of

Master of Engineering by Research

From

University of Wollongong

by

Salar Niknafs BEng(Hon), MEng(Prac)

Materials Engineering

2007

CERTIFICATION

I, Salar Niknafs, declare that this thesis, submitted in fulfilment of the requirements for the award of Honours Master of Engineering by Research, in the Materials Engineering Discipline, University of Wollongong, is wholly my own work unless otherwise referenced or acknowledged. The document has not been submitted for qualifications at any other academic institution.

Salar Niknafs
August 2007

ACKNOWLEDGEMENTS

"If I have been of service, if I have glimpsed more of the nature and essence of ultimate good, if I am inspired to reach wider horizons of thought and action, if I am at peace with myself, it has been a successful day."

-- Alex Noble

I would like to acknowledge my supervisor Professor Rian Dippenaar, not only for his academic support, but for ensuring many a successful day. Many thanks to my colleagues, Sima Aminorroaya, Mark Reid and Dominic Phelan for offering me valuable advice throughout my research; and to my friends Behzad Fatahi and Hani Zahiri for their thoughtful criticisms.

Most importantly, I want to express my gratitude to my family, without whom this work could not have been achieved.

ABSTRACT

During continuous casting of steel, the delta-ferrite to austenite phase transition occurs following solidification in the meniscus region of the solidifying strand. It is of great industrial significance to gain a better understanding of the nature and mechanism of this reaction because product quality is in large measure determined by events occurring during and shortly following solidification. Moreover, the exact way in which delta-ferrite transforms to austenite may influence the subsequent transformation of austenite to ferrite, by which much of the mechanical properties of the steel is determined.

Relatively little attention has been devoted to the delta-ferrite to austenite phase transition in the past, in part because of the difficulty of making in-situ observations at the high temperature at which this phase transition occurs. The recent development of high-temperature laser-scanning confocal microscopy has provided new opportunities to observe in-situ high temperature phase transformations and this technique has been employed in the present study.

In order to limit grain boundary pinning by alloying elements and alloy compounds during growth of delta-ferrite grains and their influence on the δ-to-γ phase transition, the solid-state phase transformation was studied in low-carbon iron-carbon alloys. Experimental observations of the effect of cooling rate on the δ/γ phase transformation are discussed in terms of three different morphologies that have been observed.

At low cooling rates the newly formed austenite phase that nucleated at triple points grow by an advancing planar interface but at higher cooling rates the transformation occurs by a massive kind of transformation. The mechanisms of grain boundary movement also been investigated. Two types of grain boundary movement, continuous motion and staggered motion have been observed. Quantitative analysis of grain boundary movement show that at low cooling rates grain boundaries are stationary for a few seconds after the initiation of the phase transformation and then they progress exponentially. Computer simulations have been used in an attempt to better explain the experimental observations.

TABLE OF CONTENTS

Table of figures

Chapter 1- Introduction

Introduced commercially on a large scale around 1960, continuous casting is currently the predominant mode of solidification processing in industrial steelmaking. More than half of the continuous cast steel output is converted into flat products, cast as slabs and slab production dominates in industrialized countries. The most common continuous casting process features an upright positioned oscillating mould with powder as lubricant. In order to reduce production cost, reduce energy consumption and to design more environmentally friendly processes, near net shape casting processes have received much attention in resent years. For the production of flat products we saw the introduction on large scale, of thin slab casting technology and more recently, thin-strip casting techniques. In these new processes, the reduced strand thickness requires an increased cooling rate with a concomitant finer solidification structure. Of greater significance with respect to the present study, is the fact that the higher surface-to-volume ratios in the near net shape casting processes, require higher casting speeds, which in turn, increase the propensity to surface defects. Moreover, there are significant economic pressures to accomplish higher throughputs (achieved by higher casting speeds), thereby exacerbating the already difficult task of surface quality assurance. It is therefore vitally important to develop an improved understanding of the causes of defects in order to design effective counter measures. Of specific significance to the present study, is the occurrence of transverse surface cracks that appear during the straightening operation of slabs.

It is generally accepted that the surface quality of continuously cast steel slabs is a strong function of events occurring during the early stages of solidification in the meniscus region of the mould and the subsequent microstructural development in this region. Microstructural development is intimately linked to mechanical properties and the finding that transverse surface cracks are usually worse on the strand face that undergoes tensile strain during straightening (unbending) has prompted hot-ductility tensile tests of steels in the temperature range and at strain rates similar to those in a caster. Most steels exhibit a ductility trough with a minimum in ductility close to the Ae_3-temperature where weaker ferrite starts to form on austenite grain boundaries. Transverse cracks most often seem to initiate at the base of oscillation marks and/or other surface depressions and cracks are invariably inter-granular and follow along

boundaries of exceptionally large prior-austenite grains. The formation of oscillation marks in turn, is associated with the vertical oscillation of the water-cooled copper mould that causes significant changes in the local heat transfer, fluid flow and solidification in the meniscus region. Many theories have been advanced to explain the occurrence and exact mechanism of oscillation mark formation but it seems that the phenomenon is not completely understood as yet. However, there is little doubt that when deep oscillation marks form, the local heat transfer conditions are altered significantly and that transverse surface cracks, which subsequently develop in the slab, originate at the roots of oscillation marks. These oscillation marks can be quite deep and microscopic examination points to a very complex interaction between mould, meniscus and mould flux.

Convincing experimental evidence has been provided that transverse surface cracks follow soft ferrite films that outline very large prior austenite grains. Moreover, quantitative analysis, using micro-mechanical modelling techniques has shown that plastic deformation is concentrated in the ferrite films because the initial yield stress and the flow stress in ferrite are considerably lower than those of austenite in the range of the starting temperature for ferrite formation. Hence, cracks initiate in the ferrite films, leading to crack propagation. It was furthermore shown that the large austenite grains develop after the surface has completely solidified. Cracks along prior austenite grain boundaries are not inter-dendritic but they cut through pre-existing dendrite arms. It has been argued that the existence of abnormally large prior austenite grains is the key factor and a mandatory prerequisite for transverse cracking. However, very little information is available on the origins of these very large austenite grains and consequently, a better understanding of exactly how and when these large grains form would be a big step forward towards alleviating transverse surface cracking.

It is difficult to explain the development of large austenite grains at the roots of oscillation marks in low-carbon steel but there is reason to believe that large austenite grains may originate from large delta-ferrite grains. Earlier high-temperature laser-scanning confocal microscopy studies have indicated that the transformation of delta-ferrite to austenite commences at delta-ferrite triple points. Austenite then grows preferentially along the delta-ferrite grain boundaries. These delta-ferrite grains are

large, typically more than a millimetre in diameter at 1430ºC, and very large austenite grains are likely to grow from large delta-ferrite grains that have developed in the thin solidifying shell close to the meniscus, notwithstanding the fact that the surface grains that initially form on solidification may be small.

It appears that there is an intimate link between the occurrences of transverse surface cracks, oscillation marks and abnormally large austenite grains. It seems plausible that the abnormally large austenite grains could grow from large delta-ferrite grains. It is likely that very large delta-ferrite grains can form at the roots of oscillation marks where the local heat transfer rate is significantly reduced and hence, the localized area at the root of an oscillation mark will cool at a much lower rate. Hence, more time is spent at higher temperatures where delta-ferrite grains can grow very rapidly. The present study was therefore designed to study the delta-ferrite phase transformation as a function of cooling rate and to attempt to establish a link between delta-ferrite grain size and the size of the austenite grains that grow from delta-ferrite. The detailed approach which was followed is based on the knowledge that excessively large austenite grains at the roots of oscillation marks lead to the formation of transverse surface cracks, having evidence that the large austenite grains form in the solid state and is not related to dendrite growth and the fact that the heat transfer rate is significantly lowered in the vicinity of oscillation mark grooves.

In the present study, Laser-Scanning Confocal Microscopy has been used to simulate different cooling rates from the delta-ferrite to austenite region, as happens in the oscillating mould of a continuous casting machine. A careful choice of steel grade with no alloying additions ensured the elimination of grain boundary pinning due to the precipitates. Following equilibration in the delta-ferrite phase field, specimens (diameter 4mm and height 2 or 0.15 mm) have been cooled at cooling rates between 5ºC/min and 70ºC/min into the to austenite and eventually ferrite regions. Qualitative as well as quantitative analysis of the delta-ferrite to austenite phase transformation has been conducted and phase-field modelling techniques have been used in support of the experimental findings.

Chapter 2- Literature survey

2.1 Continuous casting

During the last few decades, continuous casting has gained increasing importance for the production of superior quality pre-forms for specific subsequent processing such as forging, rolling, extrusion and drawing. At around 1985, 50 percent of the crude steel production in the world was produced by continuous casting techniques, but today it is the major mode of solidification processing in industrial steelmaking. [1-3] Thin slab casting, one of the focus centres of continuous casting, is able to produce slabs from 5-9 centimetres thick, as opposed to conventional slab casting in which the final thickness of the product is about 25 cm. Large roughing mills are eliminated and slab production is integrated with sheet and strip rolling, thereby, greatly reducing reheating and overall energy requirements.

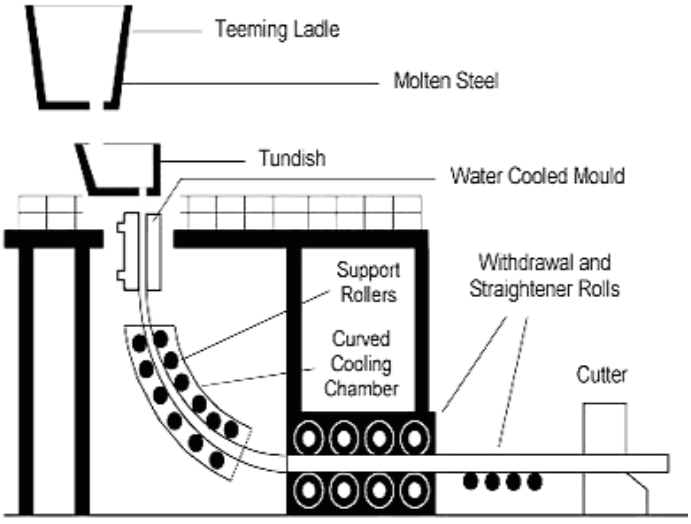

Figure 1 Slab casting process

In continuous casting, schematically shown in Figure 1, liquid steel is poured from a tundish at a controlled rate into a water-cooled copper mould where a thin solid shell forms. In order to enhance casting speed and to prevent sticking between the mould and the shell the mould is vibrated vertically (mould oscillation) throughout the casting sequence. When the liquid metal contacts the mould wall, the newly solidified

shell is sufficiently strong to maintain its shape and sustain the liquid core. Further solidification occurs in the secondary cooling zone which is positioned below the copper mould through which the mostly-liquid strand solidifies. The solid strand then goes through unbending and straightening sections. The fully solidified strand is finally cut into slabs.

2.2 Phase Transitions in Iron based Alloys

The main focus of this study is on the delta-ferrite to austenite phase transition. During this transition the structure of the iron lattice transforms from body centred cubic (B.C.C) delta ferrite into face centred cubic (F.C.C) austenite. The phase transition is accompanied by a change in volume and solute solubility and involves the movement of an interface between the parent phase and the precipitate. [4] In practice, phase transition morphology has a significant effect on the mechanical properties and the final quality of the product. For example during the casting process of peritectic grade Fe-C steels, a clear understanding of the mechanism of transformation and the effect of volumetric changes upon the stress that develops in the steel shell, are of vital importance. [4] Figure 2, the Fe-C phase diagram shows the phase transitions that can occur in this alloy system.

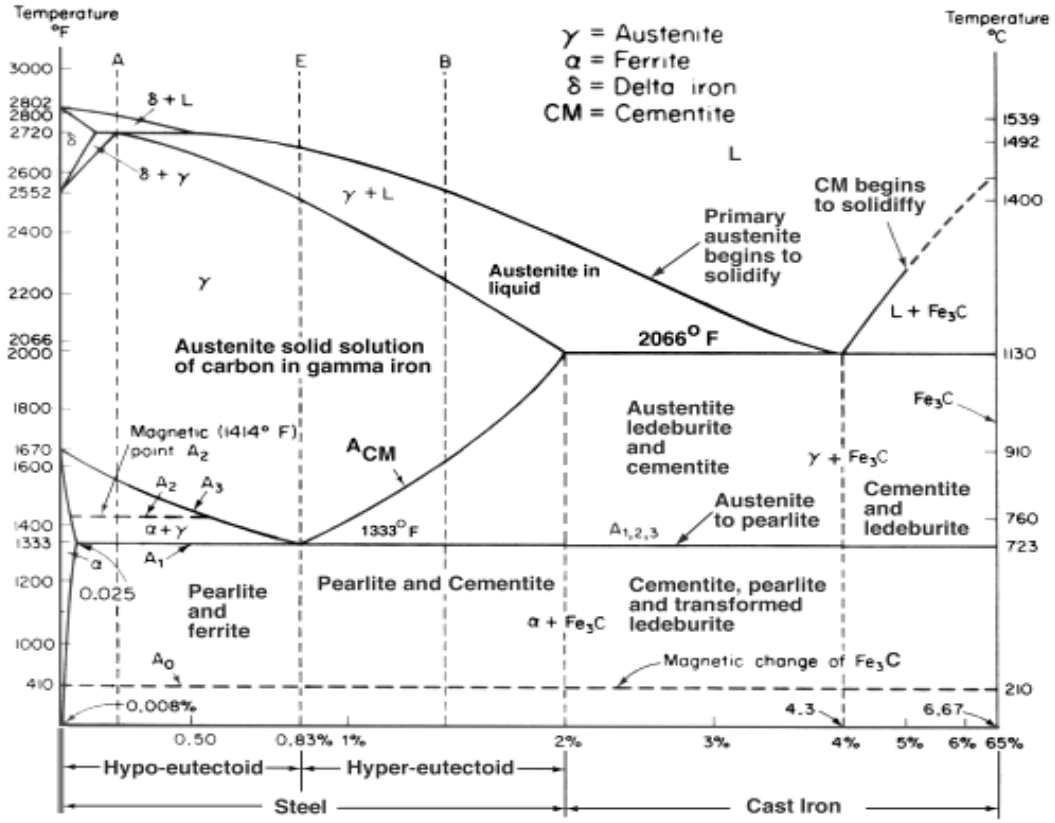

Figure 2 Iron-carbon phase diagram

2.2.1 Solidification

Solidification from the melt gives rise to a phenomenon which is of enormous technological importance. A huge range of mechanical properties of materials such as strength, ductility, hardness and toughness are significantly influenced by the mechanism and rate of solidification. It is during the vital stage of processing that shrinkage cavities and porosity can form, cracks can initiate, distortion of the solidifying shell can occur and oscillation marks can form.

In addition to the typical defects which may form as a result of inadequate solidification control, other surface defects such as slag entrainment and pinholes can also form and reoxidation of the molten steel can take place. [5] Figure 3 shows some of the imperfections that can form during solidification. The present discussion however will be confined to the delta-ferrite to austenite phase transition and aspects directly linked with this phase transformation.

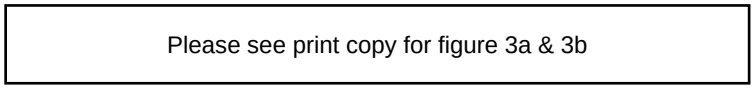

Figure 3 (a) solidification defects [6] (b) oscillation marks [7]

2.2.2 Delta-ferrite to austenite phase transition

The δ/γ phase transformation is of great practical significance in the continuous casting of steel. The transformation is accompanied by a change in volume, thermal expansion coefficient and creep behaviour which can lead to the formation of cracks and even breakouts. This transformation occurs in the primary cooling section of continuous casting system (in the water circulated copper mould); when the newly formed steel shell is still very thin. [4]

The mechanical properties of the final product are also influenced by the nature of the delta-ferrite to austenite phase transition, especially in the way the transformation alters the resulting grain size. The transformation can influence the subsequent austenite decomposition because the finer the austenite grains, the more austenite grain boundary area and the more preferred locations for the nucleation of alpha-ferrite grains. In addition to the nature of the delta-ferrite to austenite phase transformation, the thermo-mechanical processing route will also influence the size of austenite grains, thereby varying the mechanical properties of the final product. [8]

In thin-slab casting and especially in strip casting, it is difficult to control the microstructure of the final product by control of the thermo mechanical processing route. Accordingly, it has become very important to gain a better understanding of the mechanism and rate of the delta-ferrite to austenite phase transformation and what the impact of this phase transition is on product quality. [8]

Although the delta-ferrite to austenite phase transition clearly has a determining influence on product quality of continuously cast steel, the nature of this transition has not received much attention in the past. This is due, at least in part, to the subsequent austenite to alpha-ferrite phase transition which leads to a range of different structures depending on the cooling rate and casting conditions that conceal the preceding delta-ferrite transformation. Moreover, the δ-ferrite/γ phase transition occurs at high temperatures and is accompanied by the emission of infrared light from the heated sample which makes high resolution observations in the optical microscope very difficult. [4]

2.3 Oscillation Marks

Different types of defects such as oscillation marks, cracks and surface depressions can be found on the surface of steel slabs produced through the continuous casting route and most of these defects initiate in the early stages of solidification in the mould. Oscillation marks form perpendicular to the casting direction and are mostly parallel to each other. The presence of oscillation marks can result in quality problems in the final product, for example they are regions susceptible to the accumulation of inclusions and bubbles. It has also been shown [9-11] that surface depressions such as oscillation marks are the most preferred location for the initiation of transverse surface cracks; leading to breakouts in the most severe case. [12]

There have been numerous studies on the nature and occurrence of oscillation marks. For example Takeuchi [13] recommended techniques to predict and prevent breakouts that occur due to the thermal fluctuations around the oscillation marks. Thomas *et al.* [14] have shown that surface depressions and oscillation marks have a significant effect on decreasing the local heat transfer at the root of the oscillation marks. Emling *et al.* [15] suggested that on-line monitoring of the temperature fluctuations in the mould walls, using thermocouple signals can be a useful way to identify the presence of such surface defects. In current continuous casting practice a variety of early detection techniques have been implemented and it has become standard practice to monitor mould oscillation, mould temperature distribution and friction within mould.

2.3.1 Description of Phenomena

Figure 4 illustrates the suggested mechanism by which oscillation marks form. The solidifying steel shell moves vertically down the mould during the initial stages of solidification in a continuous casting machine. [14] In order to prevent sticking between the mould and the shell, the mould is oscillated vertically throughout the casting sequence (mould oscillation or oscillation cycles). Each oscillation mark results in a depression in the solidifying shell at a position close to, but below the meniscus, caused by oscillation cycles. There have been many attempts to describe the exact way by which oscillation marks form. These mechanisms include freezing and overflow of the meniscus [16-21], bending of the weak shell by the interaction between pressure in the liquid flux layers, the ferrostatic pressure [13, 22-27] and the thermal stresses in the solidifying shell. [28]

Please see print copy for figure 4

Figure 4 Schematic of initial solidification near meniscus [14]

During stable casting conditions, oscillation marks appear as shallow, equally-spaced horizontal depressions on the surface of the as-cast steel slabs or blooms. If the metal level is unstable due to the liquid turbulence or waves on the top surface, the oscillation marks will emerge non-uniformly and the solid surface may also contain more serious defects, such as ripples or deep depressions. [14] Some of the factors that control the depth of the oscillation marks are type and consumption of mold

lubricant, the choice of oscillation parameters, the steel composition and the casting speed. [29]

It is generally believed that negative strip is the main casting parameter that affects the formation of oscillation marks. Negative strip time refers to the period of time during which the mold is moving downwards faster than the strand; the remaining duration of the oscillation cycle is referred to as the positive strip period. For sinusoidal oscillations, negative strip time is calculated by equation1. [30]

$$t_n = \frac{1}{\pi f} Arc\cos\left(\frac{v_c}{\pi s f}\right) \quad \textbf{(1)}$$

t_n: The negative strip period *f: The frequency of oscillation*
V_c: The casting speed *s: The stroke*

It follows from equation (1) that:

$$s = \frac{v_c}{\pi f \cos(t_n \pi f)} \quad \textbf{(2)}$$

Any increase in the negative strip time or an increase in the casting speed will increase the depth of the oscillation marks. Therefore one possible solution to eliminate the severity of oscillation marks would be to reduce the negative strip period. However in practice it is not always possible to decrease the negative strip time without exacerbating other potential problems such as sticker breakouts. [12]

2.3.2 Abnormal Grain Growth and Oscillation Marks

Oscillation marks typically has a depth of 0.5 mm and a pitch of 1.5 cm. [31] Optical microscope studies of these surface depressions revealed that transverse surface cracks follow the boundaries of extraordinarily large prior-austenite grains which can be as large as 1 to 4mm in diameter. As shown in Figures 5 and 6, these transverse cracks follow prior austenite grain boundaries and that they can extend to a depth of 6mm below the surface. [32]

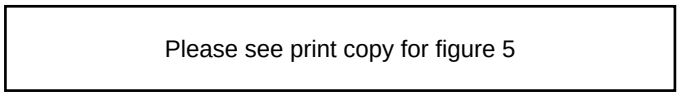

Figure 5 Abnormally large austenite grains along oscillation marks [11]
CD: Casting Direction OM: Oscillation Marks
(Oscillation marks are approximately 10mm apart)

Szekeres [11] refers to the coarse prior-austenite grains as "blown grains" and maintain that blown grains as the most important factor for the formation of transverse surface cracks, star cracks and crazing. Szekeres also shows that the formation of blown grains occurs mainly during or subsequent to the solid state δ to γ phase transformation and that solidification itself plays little, if any, role in the subsequent growth of austenite grains.

Although the exact mechanism by which oscillation marks from is not yet clearly understood, there is convincing evidence that deep oscillation marks alter the local heat transfer between the solidifying steel shell and the mold. There is also a large body of evidence in support of the premise that the cracks, which subsequently develop in the slab, initiate at the roots of oscillation marks. Accordingly to minimize the surface depressions of the final product in slab casting process, it is vital to have precise control during the early stages of solidification in the meniscus region of the mold. [33]

Figure 6 shows another example of a transverse surface crack that follows prior austenite grain boundaries.

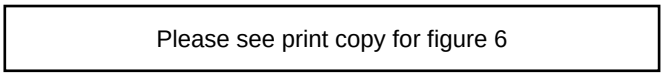

Figure 6 Transverse crack at the base of an oscillation mark on the as cast top surface of a 0.20%C steel slab. Etched in hot HCl [11]

Brimacombe *et al.* [34] provided a clear classification of the origin of cracks that can form in a continuous caster. McPherson *et al.* [35] and Wolf [5] further expanded our knowledge of the formation and propagation of transverse surface cracks. These cracks tend to be inter-granular and propagate along grain boundaries of abnormally large austenite grains. To study the growth rate of austenite grains, Maehara et al. [36] prepared cylindrical steel samples with different carbon contents. The samples were melted and cooled from 1580°C at the constant rate of 0.28°C/sec, water quenched after different times and the austenite grain size determined. Their results are reproduced in Figure 7.

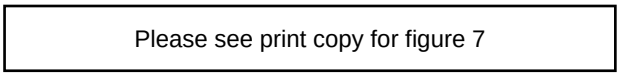

Figure 7 Grain growth of austenite grains during continuous cooling. The specimens were remelted at 1580°C, cooled to a given temperature at the rate of 0.28°C/S and then water quenched [36]

As the figure illustrates, abnormal growth of austenite grains occurs in the temperature range 1450°C to 1350°C. Additionally, the carbon content of the steel has a major effect on the growth rate of virgin austenite grains. Two important conclusions are evident:

- Very large austenite grains develop in steel of peritectic composition, evidently because austenite forms at higher temperatures in steel of peritectic composition.

- Very large austenite grains develop when a low carbon steel is held isothermally at 1450ºC, indicating that there is a relationship between δ-ferrite and austenite grain size.

In continuous casting the surface temperature of the strand is less than 1300°C when it exits the mould. It therefore seems as if blown grains develop while the surface of the strand is still in contact with the mold. There is also a possibility that mechanical or thermal strains may cause the virgin austenite grains to grow at temperatures below 1350°C. [11]

The proposed mechanism [11] by which blown grains lead to the formation of surface cracks is shown schematically in the Figure 8.

Please see print copy for figure 8

Figure 8 Schematic illustration of events in the formation of surface cracks related to blown grains during casting [11]

During the initial solidification stage, the small newly solidified grains form on the mould wall. In the regions where the temperature is higher than 1350°C, the grains begin to grow rapidly. Precipitates, liquid copper or solid sulphides form on the grain boundaries of the newly formed large grains. This allows micro-cracks to initiate. As the specimen is further cooled, nitride precipitates form. This is followed by the nucleation and growth of proeutectoid ferrite along austenite grain boundaries. [11] Stress induced by the unbending and straightening operations tend to concentrate in the softer ferrite layer along austenite grain boundaries and due to the stress concentration in this film of soft ferrite, micro-cracks propagate along the ferrite film. The most severe case is where a thin film of ferrite formed on the boundaries of large (or blown) austenite grains; the micro-cracks can then easily propagate intergranularly.

2.4 Theories on Grain Growth

This section aims to provide an overview of the current position of the research on the subject of different scenarios and mechanisms of grain growth especially in low and ultra low carbon steels. Some classical theories are being reviewed and both normal and abnormal grain growth will be considered.

2.4.1 Normal Grain Growth

The following section deals with important theories describing the process of normal grain growth. A brief overview will be presented on the developments since the early work of Burke and Turnbull in 1952.

2.4.1.1 The Burke and Turnbull Analysis

Theoretical dependency of grain growth (measured by the average grain size) on time was first deduced by Burke and Turnbull in 1952. [37] They suggested two possible mechanisms to decrease the free energy and to force the grain growth. The first potential mechanism states that some grains retain residual stress following

recrystallization. This leaves the chance for less strained grains to grow at the expense of stressed grains. The second mechanism suggests that any decrease in the area of grain boundaries, which leads to a decrease in the interfacial energy, can be a driving force. The justification for the second mechanism arises from research performed by Burke indicating that grain growth stops when grain boundary melting in induced. The mathematical formulation of this phenomenon is given by equation (3) were σ is the surface tension, V atomic volume, ΔF the change in Gibbs free energy and r_1 and r_2 are the radii of curvature of the grains between which the atoms are transferred. [38]

$$\Delta F = \sigma V\left(\frac{1}{r_1} - \frac{1}{r_2}\right) \textbf{(3)}$$

(Refer to appendix 1 for further discussion)

2.4.1.2 The Smith Analysis

In the analysis of the grain growth kinetics by Burke and Turnbull, geometrical effects were not taken into consideration. Smith [39] argued that when an individual grain in a polycrystalline matrix grows or disappears, the growth or disappearance affects adjacent gains and finally the effect echoes through the entire matrix of the polycrystalline substance.

Smith then puts forward Euler's equations for both two dimensional (2D) and three-dimensional (3D) structures, equations (4) and (5).

2D structure:	**F – E + V = 1**	**(4)**
3D structure:	**-C + F – E + V = 1**	**(5)**

In Equations 4 and 5, V is the number of vertices, E stands for edges (or sides), F is faces and C is cells (only in 3D structures).

In some structures (named topologically stable structures) the topological properties do not alter by small deformations. In order to characterize these stable structures the Z factor (vertex conservation number) is introduced which is the number of edges joined to a particular vertex. For a topologically stable two dimensional structure Z=3 which leads to the equilibrium angles being 120 degrees. The value of Z is equal to 4 for a three-dimensional system and results in an equilibrium angle of 109º28´ (the tetrahedral angle). The average number of edges per face, <N>, in a two-dimensional structure is 6. A polygon which is built totally according to the given values of equilibrium angle, average number of edges and 2D conservation number is topologically stable. As a result the polygon shows no tendency towards changes such as grain growth.

The relationship between the average number of edges per face <N> and the average number of faces per cell <F> is different in the case of 3D structures. In a three-dimensional structure these values are related as equation 6.

$$< F >= \frac{12}{6 - < N >} \qquad \textbf{(6)}$$

There is no solution for the equation 6 to build a polygon with the equilibrium angles of 109º28´ and planar sides. A 14-sided polygon is the closest shape to the topologically stable structure; however, faces must become curved to achieve the equilibrium angles of 109º28´. The curved faces then result in grain growth as they have a greater grain boundary area compared with plane sides. The relation between the number of the faces per grain and the resulting topological destination can be summarised as below:

$F > 14$ ➔ **Convex sides ➔ growth** (due to the out-ward surface tension forces)

$F < 14$ ➔ **Concave sides ➔ shrink** (due to the in-ward surface tension forces)

2.4.1.3 Mean Field Theories

Burke and Turnbull studied the movement of an individual grain boundary or a part of it to describe the grain growth phenomena, ignoring the effects of grain boundary movement on the boundary network. On the other hand Smith neglected the kinetic parts of the grain growth and analysed the topological aspects of the entire network to describe the growth or the shrinkage of the grains. Mean field theories have been developed to combine the previous theories described above in order to obtain a more precise explanation of grain growth process.

Hunderi and Ryum [40] and Atkinson [41] in developing a mean field theory argued that grain growth can be described as a change in grain size distribution, $f(R)$, as a function of time, as shown in Figure 9.

Please see print copy for figure 9

Figure 9 Grain growth as a change in gain size distribution as a function of time [41]

Figure 10 illustrates the assumed driving forces in the mean field theory, which lead to an increase in the average grain size of the grains within $f(R)$.

Please see print copy for figure 10

Figure 10 mechanisms of grain growth according to the mean field theory [41]

The concentration gradient (df/dR) is the first driving force for grain growth which is assumed to be a diffusion-like process and applies to the grains with a size greater than average ($\overline{R}$). Reducing the grain boundary area is the second driving force for grain growth which leads to grain boundary migration. The rate of this migration can be expressed by equation (7). [41]

$$v = dR/dt \qquad \textbf{(7)}$$

The overall flux of grains, j is given by equation (8). [41]

$$j = -D_d \frac{\partial f}{\partial R} + fv \qquad \textbf{(8)}$$

In equation 8, the effect of grain boundary mobility is taken into account via the diffusion coefficient (D_d). The overall flux of grains is also dependent on f_v, the distribution function which is a function of both time and the grain size (R). The development of f , the distribution function, with time leads to equation 9.

$$\frac{\partial f}{\partial t} = \frac{\partial}{\partial R}(-j) = \frac{\partial}{\partial R}\left(D_d \frac{\partial f}{\partial R}\right) - \frac{\partial}{\partial R}(fv) \quad \textbf{(9)}$$

Equation 9 represents the dependency of grain size on both drift velocity (due to the elimination of grain boundary area) and to the diffusion (due to the gradient df/dR). This equation forms the basis of different mean field theories.

2.4.1.3.1 Mean Field Theories based on the drift velocity term

Hillert [42] and Feltham [43] in their interpretation of the mean field theory focused on the drift velocity term of the equation 9 and ignored the diffusion term. As a result equation 9 can be simplified as below.

$$\frac{\partial f}{\partial t} + \frac{\partial}{\partial R}(fv) = 0$$

The distribution function can be determined experimentally and by using the simplified equation the drift velocity can be calculated. Another approach is to solve the equation for the distribution function, taking an expression for the velocity term.

Hillert [42] uses an expression for the drift velocity and solves the equation 9 for the distribution function. The expression he adopts for the boundary velocity is derived from the earlier work of Greenwood [44]. Hillert starts with the widely accepted assumption that the pressure difference between two adjacent sides of a grain boundary which is caused by its curvature is proportional to its velocity, equation 10. [42] In this equation, ρ_1 and ρ_2 are the principal radii of curvature and M is the proportionality constant which can be regarded as the mobility of the grain boundary.

$$v = M \cdot \Delta P = M\sigma \cdot \left(\frac{1}{\rho_1} + \frac{1}{\rho_2} \right) \qquad \textbf{(10)}$$

Using this equation, Hillert introduces the following expression for the average growth rate of all the particles of size R.

$$v = \frac{dR}{dt} = \alpha M \sigma . \left(\frac{1}{R_{cr}} - \frac{1}{R} \right)$$

α is a dimensionless constant, M is the grain boundary mobility and R_{cr} is the critical grain size. According to Hillert $\overline{R} = R_{crit}$ in a two-dimensional case whereas $\overline{R} = 8/9 . R_{crit}$ for a three-dimensional case. Eventually the grain size distribution takes the form of equation 11. [42]

$$P(u) = (2e)^{\beta} \frac{\beta u}{(2-u)^{2+\beta}} \exp\left(\frac{-2\beta}{2-u} \right) \qquad \textbf{(11)}$$

Where u is relative size and is equal to R/R_{crit} , β=2 in two dimensions and β=3 in three dimensions and e is an irrational constant. Figure 11 the plotted data of $P(u)$ (the relative frequency) vs. relative size (R/R_{crit}) shows the grain size distribution for both two-dimensional and three-dimensional structures. The position of the mean value $\overline{R}$ in the figure shows the values of $\overline{R} = R_{crit}$ in a two-dimensional and $\overline{R} = 8/9 . R_{crit}$ for a three-dimensional case. [42]

Please see print copy for figure 11

Figure 11 Gain size distribution in two and three dimensional systems [42]

In contrast to Hillert, Feltham [43] uses equation 9 to calculate the grain boundary drift velocity, equation 12. He assumes that the distribution function $f(R,t)$ is not

depended to time and is log-normal when plotted as $R/\overline{R}$. C_1 in equation 12 is a constant.

$$v = \frac{C_1 \overline{R}}{R} \ln\left(\frac{R}{\overline{R}}\right) \qquad \textbf{(12)}$$

2.4.1.3.2 Mean Field Theories based on diffusion term

While Hillert and Feltham focused on the drift velocity term in equation 9, Louat concentrates on the diffusion term of the equation. [45] Assuming that the diffusion coefficient D_d is independent of grain radius, R, equation 9 can be simplified as:

$$\frac{\partial f}{\partial t} = D_d \frac{\partial^2 f}{\partial R^2}$$

If the diffusion coefficient is also independent of t, the distribution function under the boundary conditions $f(0,t) = f(\infty,t) = 0$ can be computed as equation 13.

$$f(R,t) = \frac{C_2 . R . \exp\left(\frac{-R^2}{4D_d t}\right)}{D_d t^{3/2}} \qquad \textbf{(13)}$$

The time dependence of the total number of grains has been computed by integration of equation 13 for all possible values of R, equation 14.

$$N(t) = C_3 t^{-1/2} \qquad \textbf{(14)}$$

Based on equation 14, Louat discusses the parabolic growth of grains by time.

2.4.1.4 The Rhines and Craig analysis

Rhines and Craig [46] took into account the geometrical evolution of grains as well as changes in the size of the grains during grain growth. They argued that grain growth occurs in two stages, “steady state grain growth” is the stage in which the grains grow

without changing their geometrical form. This is followed by a period in which the grains change their geometry and become equiaxed. During the initial stage of growth, grains tend have a 14-sided polygon geometry, previously identified by Smith as the best suited to construct a three-dimensional space-filling grain structure under equilibrium conditions.

Rhines and Craig also introduced two new theoretical concepts in their description of the steady state grain growth: the structural gradient ω and the sweep constant θ.

The structural gradient (ω) is defined as below:

$$\omega = \frac{M_v S_v}{N_v}$$

S_v is the total grain boundary surface area per unit volume, N_v the number of grains per unit volume and M_v is the total grain boundary curvature per unit volume. M_v can be obtained by integrating the mean curvature at every point over the total area of grain boundary, equation 15.

$$M_v = \int_{S_v} \frac{1}{2}\left(\frac{1}{r_1} + \frac{1}{r_2}\right) dS_v \qquad \textbf{(15)}$$

Rhines and Craig argue that the structure gradient remains constant during the initial stage of grain growth due to the fact that the grain topology remains the same. Their experimental results which were extracted from serial sectioning of aluminium samples are shown in Figure 12.

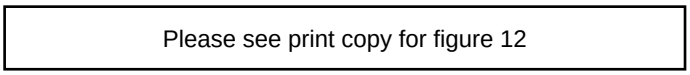

Figure 12 Plot of M_vS_v vs N_v for steady state grain growth in aluminium [46]

Rhines and Craig [46] further argued that grain growth can be characterized by the topological changes within the grain structure. In order for these changes to occur, the grain boundaries need to sweep through the structure. They defined θ (the sweep constant) as the number of grains lost when the grain boundary moves entirely through a unit volume of the polycrystal, during grain growth. Rhines and Craig suggest that, when an average single grain disappears in the system and the grain structure re-adjusts to the equilibrium, the volume swept by the grain boundaries in the system remains the same. The importance of this concept is that, knowing the sweep constant and from the sweep volume, it would be possible to calculate the number of grains that disappear. However, Doherty [47] argues that θ can not be constant. He suggests an alternative definition for the sweep constant, θ^* as the number of grains lost when the grain boundary moves through a volume of material equal to the average grain size. Hunderi and Ryum [40] argue that Doherty's definition is more realistic.

Since the introduction of the new theoretical concepts (ω and θ) by Rhines and Craig followed by their kinetic analysis, they found a growth exponent *n* of 3, different to the values of 2 obtained by Burke and Turnbull [37], Hillert [42], Feltham [43] and Louat [45]. The growth exponent of 3 results in a linear relation between the average grain volume ($1/N_v$) as a function of time during grain growth, Figure 13.

Please see print copy for figure 13

Figure 13 Plot of grain volume ($1/N_v$) against time of annealing for aluminium showing a linear relationship [46]

Due to the fact that Rhines and Craig considered not only the grain boundary movement during the grain growth, but they also took into account the topological aspects of grains during growth, their theory seems to be more complete than the earlier suggestions. However, the deduction of growth exponent 3 by Rhines and Craig has not yet been investigated by other experiments and there appear to be some errors in their analysis.

2.4.2 Abnormal Grain Growth

Although the mechanism by which some grains grow excessively is different from normal grain growth, there has been much less theoretical analysis of the nature and kinetics of abnormal grain growth. Detert [48] proposed that abnormal grain growth is the rapid increase in the size of a few grains in the recrystallised microstructure where the grain topology is not time-invariant and the grain size increases at a rate considerably higher than the arithmetic mean. Some of the major theoretical contributions on this subject are briefly reviewed.

2.4.2.1 The Gladman Analysis

Gladman [49] deals with the energy changes accompanying grain growth in a grain matrix with a dispersion of precipitate particles. In his analysis he takes into account the energy decrease of the system due to the lowering of the total grain boundary area as well as the energy increase resulting from the unpinning of the grain boundaries.

Gladman defined the term critical particle radius, r_p^*, where R is the radius of a growing grain, R_0 is the average grain size and f_v represents the combination of the two energy contributions (total energy for lowering of the total grain boundary area and for unpinning of the grain boundaries) per pinning particle.

$$r_p^* = \frac{6R_0 f_v}{\pi}\left(\frac{3}{2} - \frac{2R}{R_0}\right)^{-1}$$

He then predicts that in a system without particle pinning, all the grains with a R/R_0 ratio larger than 1.33 will show normal grain growth. Gladman then argues that abnormal grain growth can initiate from a totally pinned structure. When a situation of pinned microstructure is the dominant case, the critical radius as given by equation 14 will be larger than the average radius of the particles in the matrix, hindering the grain growth. When the particle radius increases (ie. During the coalescence of the second phase) at a specific instant, the average particle size reaches the critical radius, leading to abnormal grain growth.

2.4.2.2 The Hillert Analysis

Hillert [42] states that, in the absence of second-phase particles, abnormal grain growth will occur in a matrix that contains grains that are sufficiently large with respect to the average grain size: if such grains are larger than $2\overline{R}$ in a two-

dimensional structure or $\frac{9}{4}\overline{R}$ in a three-dimensional structure, abnormal grain growth will occur.

Hillert uses the Zener back stress factor (*S*) to take into account the pinning effect of second-phase particles. *S* is defined as virtual stress, acting against the movement of the grain boundaries.

$$S = z\sigma \approx \frac{3f_v}{4r}\sigma$$

Where f_v represents the volume fraction of the particles, *r* is the radius of the particles (taking the reasonable assumption of spherical morphology) and *z* is a factor which depends on the number and size of the second-phase particles and is independent of the grain boundary curvature. In agreement with Zener's calculation, Hillert assumes that *z* is independent of the grain boundary curvature. Hillert then argues that abnormal grain growth will occur when the Zener back stress is sufficiently decreased due to dissolution or coalescence of the second phase particles. The following three conditions have to meet before abnormal grain growth will occur.

- The pinning effect caused by second-phase particles has made normal grain growth impossible. (Refer to Appendix 2 for more information on the mechanism of second-phase particles on grain boundary pinning)
- The average grain size ($\overline{R}$) must be smaller than $\frac{1}{2z}$.
- At least one grain considerably larger than $\overline{R}$ must be present in the microstructure.

A schematic representation of the kind of grain growth that is expected to occur depending on the value of Z is shown is Figure 14.

Please see print copy for figure 14

Figure 14 Schematic representation of the type of grain growth and average grain size depending on the value of Z [42]

2.4.2.3 The Thompson Analysis

Thompson *et al.* [50] dealt with grain growth in a matrix consisting of boundaries with uniform grain boundary energies. Thompson argues that an abnormally large grain within a matrix of normal grains will not grow abnormally, but is reduced in size so as to fit into the normal grain size distribution. This argument is in conflict with Hillert's analysis since he suggested that large grain ($R > 2\overline{R}$ in a 2D structure or $R > \frac{9}{4}\overline{R}$ in a 3D structure) will initiate abnormal grain growth and eventually consume the normal grains. According to Thompson, the growth rate of the large grains (relative to the critical grain size) can be expressed by equation 16.

$$\frac{d\rho}{dt} = -\frac{\mu\sigma}{2R^{*}R_{crit}}(\rho - 2)^2 \qquad \textbf{(16)}$$

R^{*} is the radius of the large grain, R_{crit} is the critical grain size and $\rho = \frac{R^{*}}{R_{crit}}$.

Based on equation 16, the relative growth rate for abnormally large grains of size R^{*} is always negative, except when $R^{*} = 2R_{crit}$, at which the growth rate will be zero. As a result, all grains larger than $2R_{crit}$ decrease their size until the condition: $R^{*} = 2R_{crit}$

is present. At this point the grain shrinkage stops. Thompson states that his result was perfectly present in Hillert's analysis; however, Hillert followed a flawed reasoning by deducing that the larger grains would grow abnormally instead of decreasing their size.

2.4.3 Summary of grain growth theories

In the section 2.5 different theories on the normal as well as abnormal grain growth has been explained. Division of the grain growth mechanism into normal and abnormal grain growth has now been widely accepted. Most theories on the normal grain growth suggest parabolic grain growth kinetics. One exception to this agreement is proposed by Rhines and Craig [46] that suggest a linear relation between average grain volume and time. However, this controversy seems to have resulted from incorrect theoretical analysis. As a whole, Burke and Turnbull and Hillert analyses remain the most predominant theories to interpret the experimental normal grain growth behaviour, with both predicting parabolic growth kinetics.

In the case of abnormal grain growth, recent computer simulations have questioned earlier theoretical analysis of Gladman and Hillert. Nevertheless, the idea that abnormal grain growth initiates from pinned microstructure remains valid.

2.5 The effect of specimen thickness on the grain size

Beck et al. [51] were the first to relate the effect of specimen thickness to the grain growth. They observed that the grain growth of high purity aluminium grains dies away when the grain size is roughly equal to the specimen thickness. They termed this as a "specimen thickness effect", Figure 15. Later work on α-brass confirmed the same behaviour.

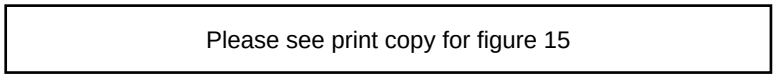

Figure 15 Maximum grain size attainable by gradual grain growth in high purity aluminium, as a function of specimen thickness showing "specimen thickness effect". (a) Specimens not etched before annealing. Empty circle: specimen extremely deeply etched before annealing [52]

Mullins [52] argued that the effect cannot be due to the inhibition arising from a dispersed second phase but is caused by the grain boundary's local curvature and the inequalities in the surface-free energy of the grains. Figure 16 shows a thin specimen consisting of two grains separated by a single boundary (thermal grooving has been ignored in this case). Assuming that the surface free energy values for the two grain follows the relation: $\gamma_+ > \gamma_-$, the boundary and the surface normal form the angle θ.

If there is a curvature on the grain boundary then θ will have a non-zero value. The grain boundary attempts to straighten up and the result is the consumption of the grains of higher surface-free energy by the grain of lower surface-free energy.

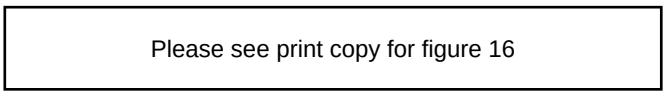

Figure 16 Migration produced by unequal surface-free energies [52]

Mullins [52] has also shows that thermal grooving will not interfere with abnormal grain growth driven by surface free energy differences of adjacent grains.

2.6 Previous work on the delta-ferrite to austenite phase transition

This section aims to provide an overview of the current position of the research on the subject of delta-ferrite to austenite phase transition especially in low and ultra low carbon steels. Yin *et al.* [32] were the first to use laser scanning confocal microscopy to study in-situ the δ-ferrite/γ-austenite phase transition. They state that during the cooling from the delta-ferrite region, austenite nucleates at triple points of δ-ferrite grain boundaries. The austenite phase then spreads over all the δ-ferrite grain boundaries and forms a thin layer on both sides of the original δ grain boundary as shown in Figure 17.

Figure 17 Formation of austenite at a δ-ferrite triple point and at a δ-grain boundary. The samples were cooled at a rate of 2ºC/min cooling rate [32]

Yin *et al.* also argue that during the delta-ferrite to austenite transformation, the δ/γ interphase boundaries are always planar or curved. A summary of the nucleation and growth of austenite in the delta-ferrite matrix observed by them at cooling rates less than 7°C/min is shown in Figure 18.

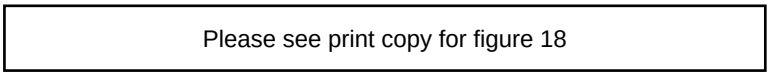

Figure 18 Schematic diagram of the nucleation and growth of the austenite phase in the δ-ferrite matrix at cooling rates <7ºC/min [32]

Yin *et al.* then took into account the effect of thermal diffusion in their observations by comparing the characteristics of the δ/γ interphase boundary during the δ to γ and also during the γ to δ phase transformation. They found that the carbon content in delta-ferrite phase decreases during the delta-ferrite to austenite phase transformation, as shown in Figure 19.

Please see print copy for figure 19

Figure 19 Comparison of the carbon distribution at the front of δ/γ interphase boundaries between during δ/γ and during γ/δ phase transformation [32]

This results in an increase in the temperature of the phase transformation, $T_c(\delta)$ as a function of distance from the δ/γ interface, Z, as shown in Figure 20. Thus, the gradient of $T_c(\delta)$ at the interface can be described as $m(\delta).G_c(\delta)$ where $m(\delta)$ in the mass percent of δ-phase and $G_c(\delta)$ is the temperature gradient based on the carbon content. Alternatively, the real temperature profile in the δ-phase, $T_\delta(\delta)$, can be different to $T_c(\delta)$, leading to a different real temperature gradient, $G(\delta)$, at the δ/γ interphase boundary. [32]

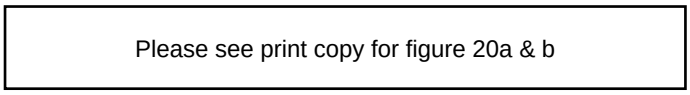

Figure 20 Comparison of the temperature profile and constitutional supercooling at the front of δ/γ inter-phase boundaries during δ to γ transformation and during γ to δ transformation [32]

According to Yin *et al.* where $G(\delta)$ is smaller than $m(\delta).G_c(\delta)$, undercooling is present in front of the δ/γ phase transformation interface, resulting in an unstable interface. During the austenite to delta-ferrite phase transformation the situation is the opposite. Firstly, the carbon content increases in the austenite phase as the distance, Z, increases, which results in a decreasing $T_c(\gamma)$ and consequently a lower value of $m(\gamma).G_c(\gamma)$. Secondly, this endothermic transformation leads to a lower $T_\gamma(\gamma)$, giving a large G(γ) at the δ/γ interface. Therefore the value of $m(\gamma).G_c(\gamma)$ will be smaller than G(γ) and hence no constitutional supercooling will exists. [32]

Phelan and Dippenaar [53] also used a laser scanning confocal microscope to study the microstructure of δ-ferrite and the δ to γ phase transition. They cycled a low-carbon, silicon-killed steel repeatedly through the δ/γ phase transformation and observed a network of sub-boundaries within δ grains following this treatment. The sub-boundary network they observed is reproduced in Figure 21. They argued that the sub-boundaries form by a process of polygonization when a stress field is imposed as a result of the volume change during the δ to γ phase transition.

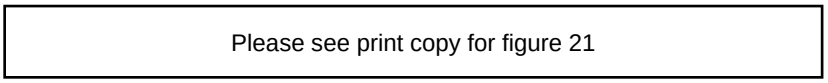

Figure 21 Delta-ferrite sub-boundary microstructure observed with LSCM [54]

Phelan and Dippennar [53] then argue that the transformation of delta-ferrite to austenite initiates at delta-ferrite triple points and austenite grows preferentially along the delta-ferrite grain boundaries. Up to this point these observations are in agreement with the observations of Yin *et al.* However Phelan *et al.* observed subsequent growth of austenite along the sub-boundaries as shown in Figure 22. Yin *et al.* did not observe this phenomenon but Phelan points out that Yin has used aluminium killed steels in which it is very difficult to observe sub-boundaries. For this reason, they may not have observed this phenomenon. As shown in Figure 22, the transformation of δ-ferrite to austenite initiates at delta-ferrite triple points. Austenite then grows preferentially along the delta-ferrite grain boundaries forming a type of "film", frame (a). The subsequent growth of austenite along the delta-ferrite sub-boundaries is shown in frames (b) and (c).

Please see print copy for figure 22a, b, c & d

Figure 22 Transformation of delta-ferrite to austenite in Si-killed steel [4]

Yin *et al.* [32] proposed that once the austenite has nucleated and grown into the matrix, the growth occurs by the propagation of a planar δ/γ front, which eventually turns into an unstable growth front, thereby leading to the finger-like austenite structure. On the other hand, Phelan *et al.* [53] argued that the presence of a finger-like structure is more likely to have resulted from preferential growth of austenite along the delta-ferrite sub-grain boundaries such as those depicted in Figure 21.

Liu *et al.* [55] made in-situ observations of the δ-ferrite to γ phase transformation on the surface of low carbon steels containing phosphorous at two different cooling rates, 19.8ºC/min and 600ºC/min. Three kinds of low-carbon steel: Low Phosphorus Steel (LPS), Medium Phosphorus Steel (MPS) and High Phosphorus Steel (HPS) were investigated and the microstructures they observed are summarized in Table 1.

Table 1 Nucleation sites and morphology evolution of austenite cells during the δ-ferrite/γ phase transformation [55]

Please see print copy for table 1

They also assessed the effect of phosphorous on the delta-ferrite to austenite phase transformation and the total time for the δ to γ transformation to go to completion is shown in Figure 23 for different cooling rates and steels evaluated. It follows that the phosphorous content of the steel has a significant influence on the starting and finishing temperature of the δ to γ transition.

Please see print copy for figure 23

Figure 23 The observed starting and finishing temperature of the δ / γ transformation for the LPS and MPS samples at various cooling rates [55]

Liu *et al.* then calculated the redistribution of solutes during the δ/γ transformation using a mathematical model. The calculation was carried out by a direct finite difference method. Figure 24 shows the calculated transformation process he concluded based on the observed data for the starting temperature of the δ/γ transformation.

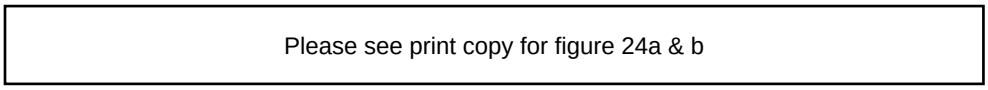

Figure 24 The observed and calculated temperatures of the δ/γ phase transformation. (a) Low cooling rate; (b) High cooling rate [55]

This is evidently reasonable agreement between the calculated and experimental values.

Chapter 3 – Experimental Procedure

3.1 Review of Experimental Techniques

A series of techniques has been employed for the study of delta-ferrite to austenite transformation phenomena. Confocal Scanning Laser Microscope (CSLM) has been used for in-situ observation of phase transformation morphology. A better perception of solid-state phase transformation has been achieved through the use of MICRESS, a phase field modelling package.

3.1.1 MICRESS, phase field software

MICRESS (the MICRostructure Evolution Simulation Software) is a software package for the calculation of microstructural development in time and space, during phase transformations. The software is based on the phase-field concept and its development started in 1995. The MICRESS, phase-field software has been employed for the simulation of microstructural evolution during phase transformations. Using the software, the effect of different microstructures and cooling rates on the phase transformation kinetics has been examined. Moreover, applications such as solidification, solid-state phase transformations, grain growth and recrystallization have also been studied.

3.1.2 Laser Scanning Confocal Microscopy

A Laser Scanning Confocal Microscope (LSCM) was used to directly observe delta-ferrite to austenite phase transformations. With the aid of a He-Ne laser with a wavelength of 632.8nm, magnifications up to 1350x and a resolution of 0.25μm can been obtained. The heat source of the furnace is a 1.5kW halogen lamp which heats the sample by radiation. The gold- coated ellipsoidal chamber concentrates the heat

on the surface of the specimen. Figure 25 shows the schematic representation of the LSCM chamber.

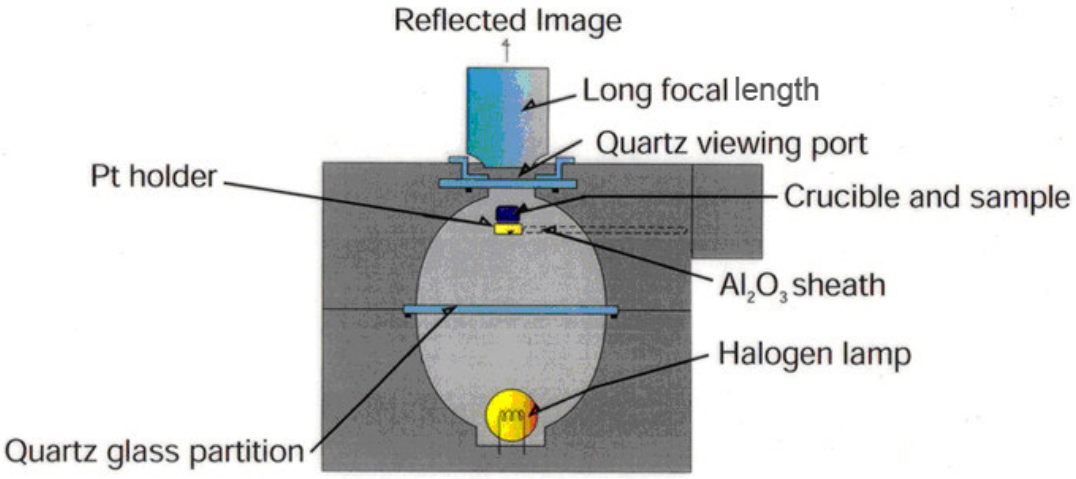

Figure 25 Schematic representation of the LSCM chamber

A high purity Argon atmosphere is maintained in the chamber to avoid oxidation of the samples at high temperature. The composition of the inert gas flowing in the microscope chamber is shown in Table 2.

Table 2 Composition of Inert Gas

Compound	**Ar**	**O_2**	**N_2**	**H_2O**
Vol %	99.999	<1ppm	<5ppm	<2ppm

To reduce trace compounds to levels lower than present in the inert gas, a Super-Clean™ gas filter was used. The purity of the carrier gas after flowing through this gas purifier is better than 99.9999% pure.

The sample is placed on a cylindrical alumina crucible with a diameter of 5mm. A specimen holder with a B-type thermocouple attached to it holds the crucible and measures the temperature, Figure 26.

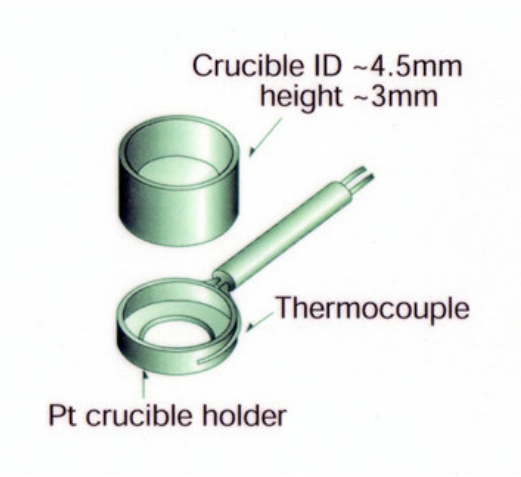

Figure 26 Schematic representations of the CSLM holder and crucible

3.2 Preparation of Confocal Microscopy Samples

The specimens used in this investigation were prepared from cylindrical specimens, prepared in a laboratory scale vacuum induction melting furnace. [56]

In order to eliminate the prevailing grain-boundary-pinning effect of alloying elements during phase transition and grain growth, masking the morphology of transition and growth, additive elements and impurities were kept as low as possible. However, in order to reduce the formation of iron oxides, aluminium was introduced to the melt as a deoxidizer. Table 3 shows the chemical composition of the specimens used in this investigation.

Table 3 Chemical composition of specimens

Specimen	Elements, wt%									
	C	**P**	**Mn**	**Si**	**S**	**Ni,Cr, Mo, Cu,Sn**	**Al**	**Nb**	**Ti,V**	**N**
A	0.05	0.002	<0.01	<0.005	0.002	<0.002	0.016	<0.001	<0.003	0.0015

CSLM samples were sectioned from the cylindrical samples as shown in Figure 27.

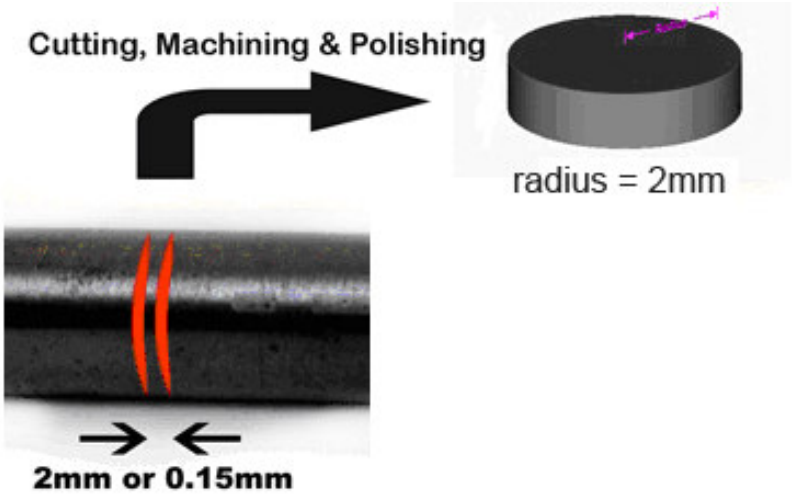

Figure 27 Sample preparation

Cylindrical CSLM samples with two different geometries were machined from cylindrical specimens using an Accutum 3500 cutting machine. Geometrical details of such specimens are shown in Table 4.

Table 4 Geometry of CSLM specimens

Sample Geometry			
Group	**Diameter (mm)**	**Height (mm)**	**Volume (mm^3)**
1	4	2	~ 25.13
2	4	0.15	~ 1.88

Preparation followed by mounting the specimen in a mixture of Bakelite and conductive PolyFast for group 1 specimens and sticking onto a brass holder using Buehler Lakeside cement for group 2 specimens. The specimens were ground using 800, 1200, 2400 and 4000 abrasive papers, and polished using 6µm alumina. All samples were then polished on 1µm diamond paste immediately before insertion into the microscope.

3.3 Procedure of the high temperature CSLM experiments

A Laser Scanning Confocal Microscope (LSCM) was used to directly observe the surface of a sample undergoing the delta-ferrite to austenite phase transformation.

This equipment allows the observation of such transformations at high temperatures and during controlled thermal cycles. Information from the literature indicated that abnormal austenite grain growth occurs during continuous cooling from around 1450 to 1350°C.

Figure 28 illustrates the surface topology of the narrow-face of an industrially produced steel slab. A profilometer was used to obtain traces of the surface topography showing the presence of 3 oscillation marks in this sample. [57]

Please see print copy for figure 28

Figure 28 Surface topography of a slab sample containing 3 oscillation marks [57]

According to the Fourier Law of heat conduction a temperature gradient within a body causes heat energy to flow from the region of high temperature to the region of low temperature following the equation below:

$$q_x = K_T \frac{\Delta T}{x}$$

q_x = *Heat transfer rate or flux* K_T = *Thermal conductivity constant*

ΔT = *Temperature difference* x = *Distance or length*

Due to the increased local heat conduction distance at oscillation marks, a lower heat flux is expected in the zone where oscillation marks form. In order to simulate this local change in heat transfer rate, six different cooling rates were imposed on the steel

samples and the morphology of the delta-ferrite to austenite phase transformation was observed. The specific cooling rates used in each case are shown in the Table 5.

Table 5 Cooling rates imposed on the steel samples in this study

Sample geometry group	Cooling rate	
	(ºC/Min)	(ºC/Sec)
1	5	0.083
1	10	1.66
1 & 2	15	0.25
1 & 2	30	0.5
1	40	0.66
1 & 2	70	1.16

The heat treatment cycles imposed on samples in the LSCM are shown in Table 6.

Table 6 CSLM time-temperature profile

CSLM time - temperature profile				
Step No.	**Step Time (min)**	**Temperature (°C)**	**Total Time (min)**	**Heating rate (°C/min)**
0	0	100	0	0
1	1	150	1	50
2	15	150	16	0
3	15	1445	31	90
4	10	1445	41	0
5	28	1305	69	-5
	14		55	-10
	9.3		50.3	-15
	4.6		45.6	-30
	3.5		44.5	-40
	2		43	-70
6	10	1305	79	0
			65	
			60.3	
			55.6	
			54.5	
			53	
7	20	100	Step 6 times + 20	-62.5
8	10	100	Step 7 times + 10	0

For the matter of clarification, the heat treatment procedure for one of the cooling rates (70ºC/min) is shown in Figure 29.

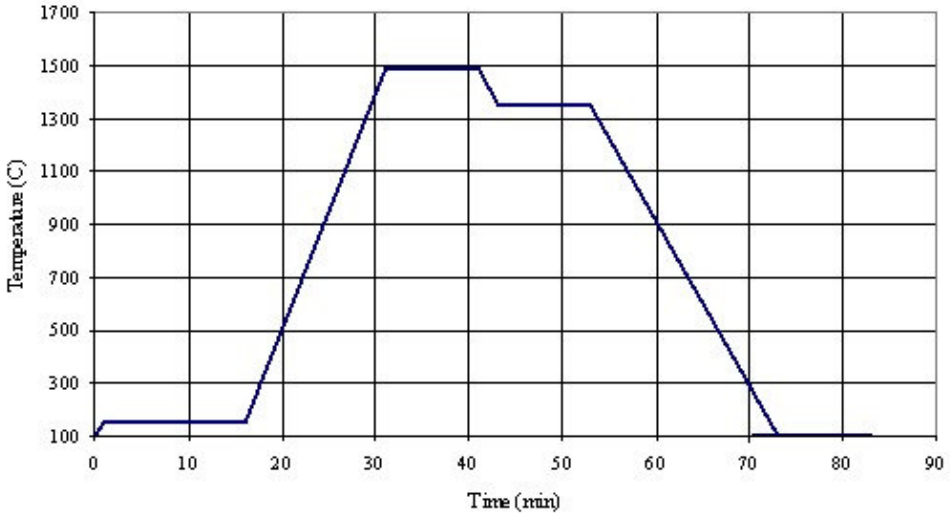

Figure 29 Heat treatment procedure at the cooling rate of 70ºC/min

As shown in Table 6, the samples were heated to 150ºC and kept for 15 minutes. The samples were then heated to delta-ferrite region and kept for 10 minutes to homogenise the structure. 6 different cooling rates from 5ºC to 70ºC has been imposed on the samples.

3.4 Typical delta-ferrite microstructure

Figure 30 shows a typical microstructure of δ-ferrite observed at 1414ºC, consisting of grain boundaries, sub boundaries and prior grain boundary grooves.

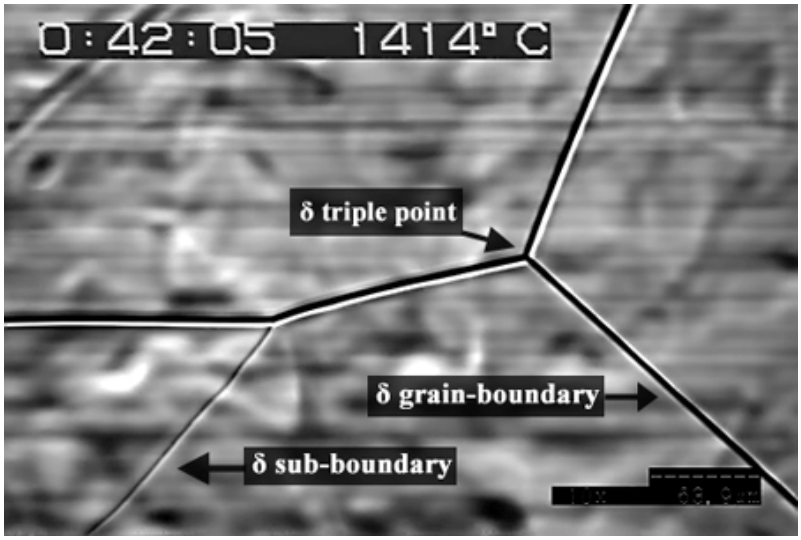

Figure 30 Delta-ferrite structure consisting GBs and sub-GBs

Figure 31 shows an austenite structure at 809ºC following transformation from δ-ferrite to austenite of a sample that was annealed at 1450ºC. A typical austenite grain boundary triple point is shown. Also shown in the photograph are the prior δ-ferrite boundary grooves. These grooves formed due to thermal etching of δ-ferrite grain boundaries; but apart from showing the original position of the δ-ferrite grains, these grooves have no crystallographic significance.

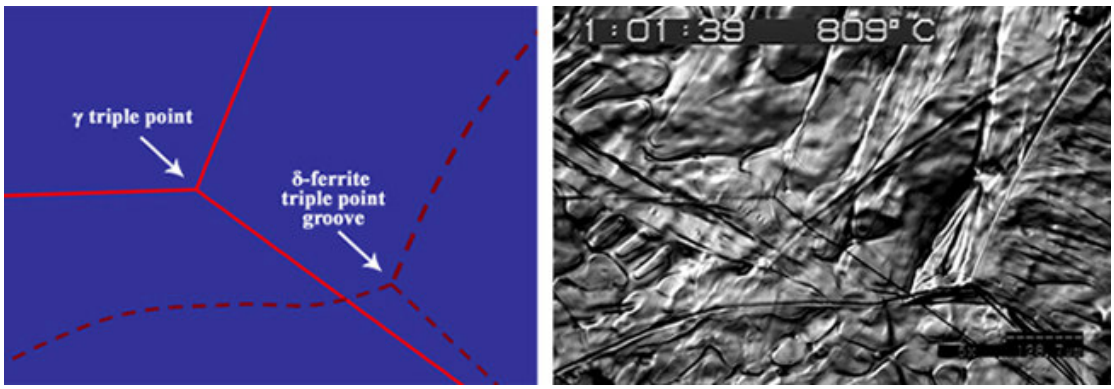

Figure 31 Austenite structure cooled from delta-ferrite region, consisting of γ-GBs and prior δ-ferrite GB grooves

3.5 Qualitative observations of phase transformation Morphologies

On heating to about 1450ºC, delta-ferrite grains form and grow, as shown in Figure 32.

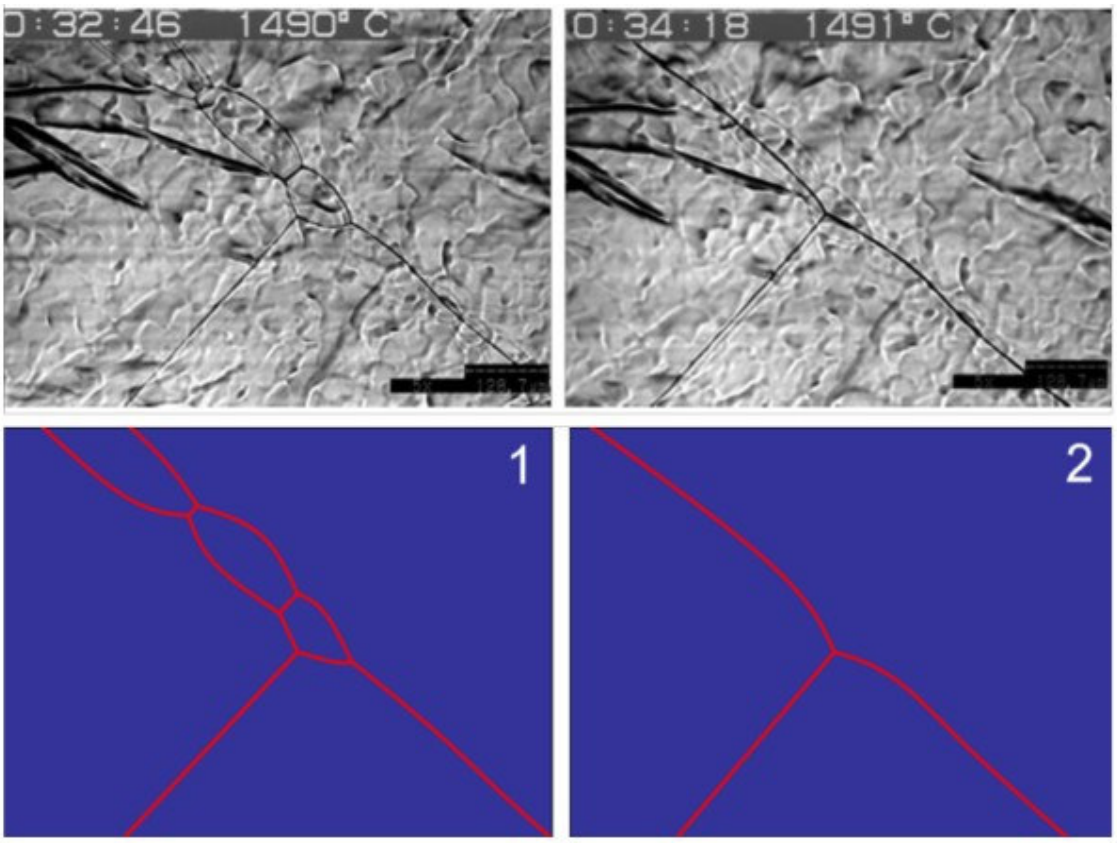

Figure 32 Disappearance of small grains. Temperature= 1492ºC. The snapshots were taken within 92 seconds (The numbered photos schematically represent the grains and their associated grain-boundaries)

Thermal grooves are also present in the delta-ferrite microstructure. They form as a result of minimizing the surface energy and appear as thick black lines along the grain boundaries. The formation of these grooves is due to the fact that grain boundaries have an interfacial energy associated with them. This leads to the diffusion of atoms from grain boundaries to the adjacent surface regions. Thermal grooves have a 'V' shape cross section which scatters the reflected light and develop high contrast with the adjacent areas. The 'V' notch becomes deeper and appears thicker and darker as the specimen is being kept in high temperature, Figure 32.

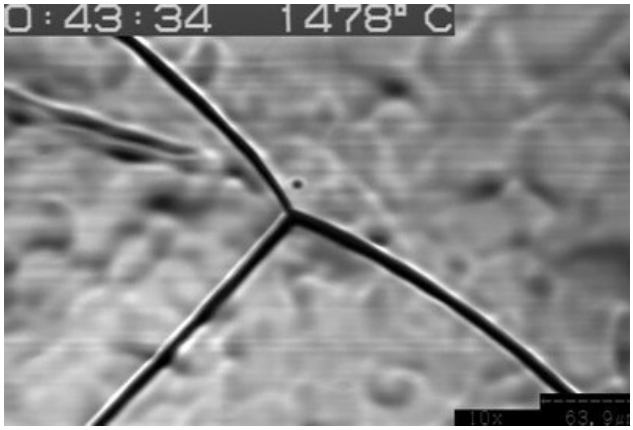

Figure 33 Development of thermal grooves along the grain boundaries at high temperatures

A schematic illustration of the cross section of a thermal groove is shown in the Figure 34.

Please see print copy for figure 34

Figure 34 Schematic representation of a thermal groove around grain boundaries [4]

Chapter 4 - Results and Discussion

The δ to γ phase transformation has been observed on the surface of a large number of specimens. In an attempt to simulate the reduced heat flux at the roots of oscillation marks during the continuous casting of steel, identical specimen were cooled at five different cooling rates (5, 10, 15, 30 & 70 ºC/min) while the morphologies of the delta-ferrite to austenite phase transformation were observed in-situ. Other interesting observations in the course of this phase transition such as the motion of delta ferrite triple points and the mobility of the interface will also be discussed.

4.1 Group 1 - 5°C/min cooling rate

The heat treatment of samples in this group is shown in Figure 35. Following the formation of a stable δ-ferrite structure, samples were cooled at a rate of 5ºC/min.

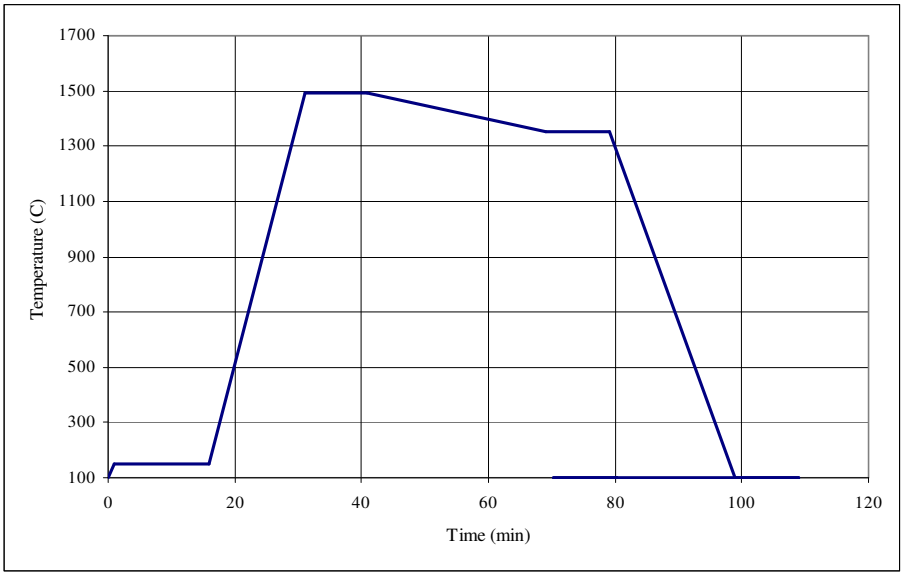

Figure 35 Heat treatment procedure

4.1.1 Motion of delta-ferrite grain boundaries

We have observed that delta-ferrite grain boundaries sometimes move in a staggered manner, but under a different set of conditions they move continuously. The staggered motion is inevitable and is due to the formation of thermal grooves and

anchoring/liberating behaviour of its associated grain boundaries. On the other hand, continuous motion is due to the initiation of the δ/γ phase transformation in the bulk which results in a disturbance in the local equilibrium of the triple points and its allied grain boundaries.

4.1.1.1 Stop-start motion (staggered motion) of delta-ferrite grain boundaries

As the grain boundaries undergo staggered motion, the thermal grooves remain as troughs on the surface in the previous location, as shown in Figure 36.

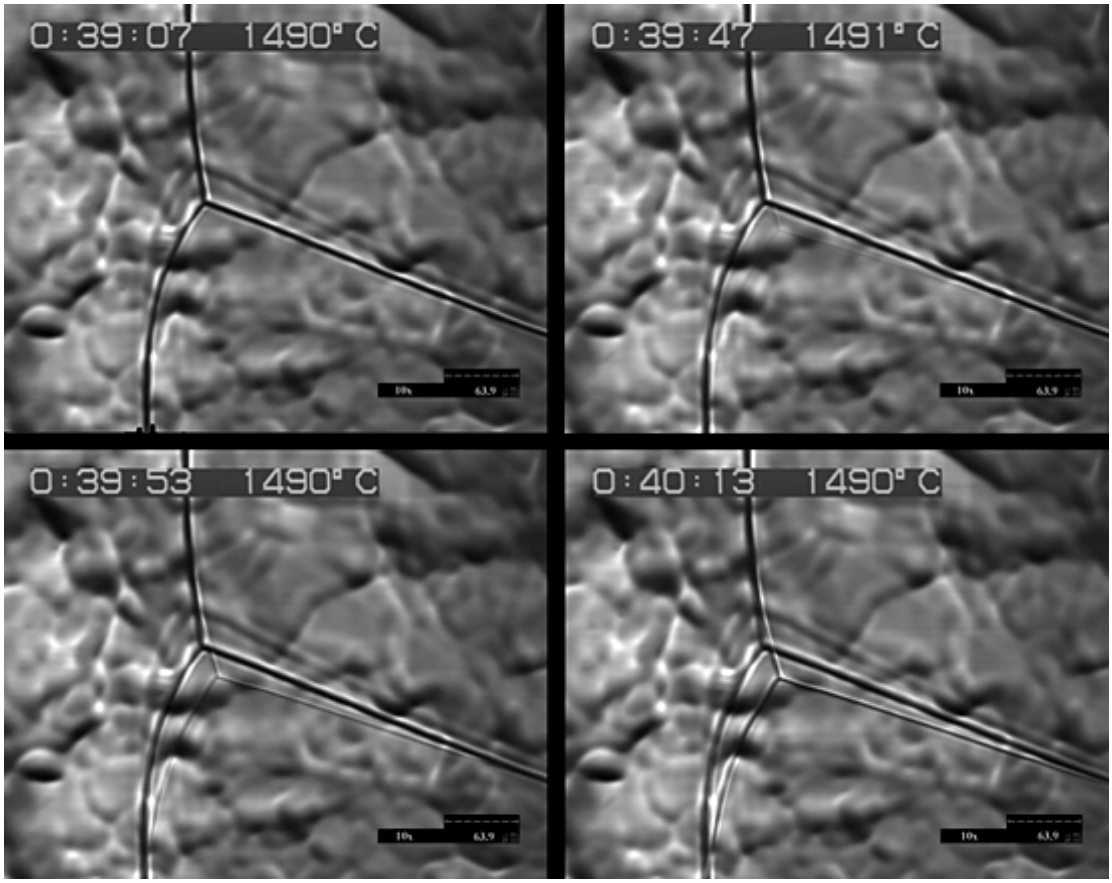

Figure 36 Stop-start motion of delta-ferrite triple point

The staggered movement of grain boundaries continue until local equilibrium at the triple junction is achieved. When local equilibrium of three grain boundaries at a triple point is attained, it can mathematically be described by the Herring equation. For the triple junction depicted in Figure 37 [58]:

$$\sum_{j=1}^{3}\left\{\sigma_j \hat{b}_j + \left(\frac{\partial \sigma_j}{\partial \phi_j}\right)\hat{n}_j\right\} = \vec{0}$$

Please see print copy for figure 37

Figure 37 Geometric parameters associated with boundaries adjoining a triple junction [59]

$\hat{n}$ *: Unit normal*	x *: Dihedral angle*
$\hat{b}$ *: Unit direction*	σ_j *: Excess free energy of the* j^{th} *boundary*

Adams *et al.* [59] state that based on the Herring equation for uniform grain boundaries in local equilibrium, the dihedral angles are 120° and $f_i = \sigma K_i$. Reaching the dihedral angles of 120° in the ideal situation can provide local equilibrium in the triple point region. This results in establishing stationary grain boundaries and accordingly stable triple points. The formation of a thermal groove can also anchor the grain boundary as shown schematically in Figure 38.

Please see print copy for figure 38

Figure 38 Grain boundary anchoring at a notch [52]

The critical angle (θ_0) is the angle between the normal to the free surface and the normal to the wall of the notch which indicates when pinning is energetically favourable. According to Mullins [52], when a grain boundary sits within the critical angle it will be anchored to the notch. This is due to reducing the length of the grain boundary and consequently reducing the free energy of the system; otherwise the grain boundary would be forced to lengthen in order to move. Conversely a boundary lying outside the critical area (between the lines a & b in the Figure 38) will escape from the notch and reduce its length.

4.1.1.2 Continuous motion of delta-ferrite grain boundaries

It has frequently been observed that in some cases the motion of delta-ferrite triple point and its associated grain boundaries evolve from a staggered motion into a consistent continuous movement, Figure 39. It is notable that the velocity of such movement is significantly greater than the preceding stop-start behaviour.

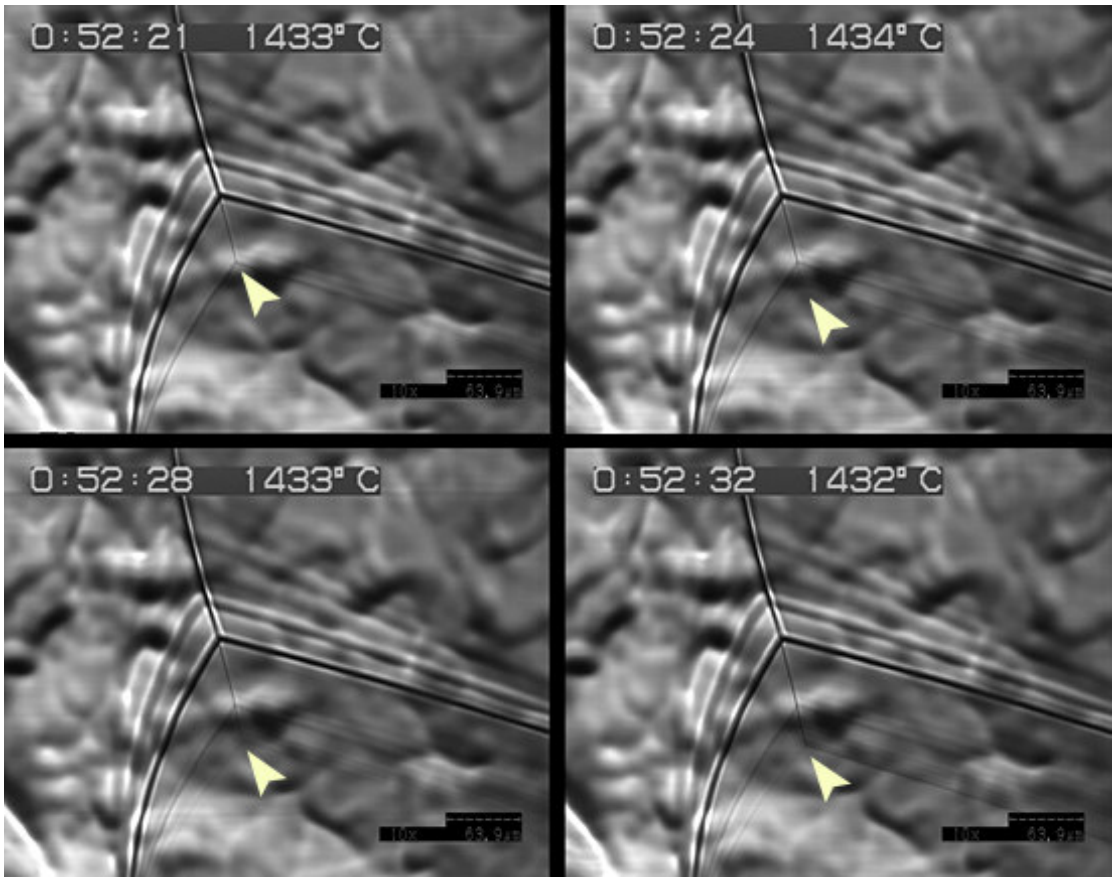

Figure 39 Continuous motion of delta-ferrite triple point before δ-ferrite/γ phase transformation

There is a possibility that the consistent continuous movement is due to the unequal surface-free energies and abnormal grain growth of adjacent austenite grains. Notably, abnormal growth of austenite grains has been observed in our experiments and will be discussed later.

4.1.1.3 Quantitative analysis of triple-point movement

In an attempt to better understand the dynamics of the irregular or continuous movement of δ-ferrite grain boundary triple points, the displacement of triple points have been recorded as a function of time as shown in Figure 40. In this instance, a triple point remained stationary for 120 seconds, then moved very rapidly to a position of 25μm away, remained stationary for another 160 seconds and suddenly moved a further 25 μm away. This process repeated itself for 860 seconds, at which time the triple point then got unpinned and moved away in a continuous motion.

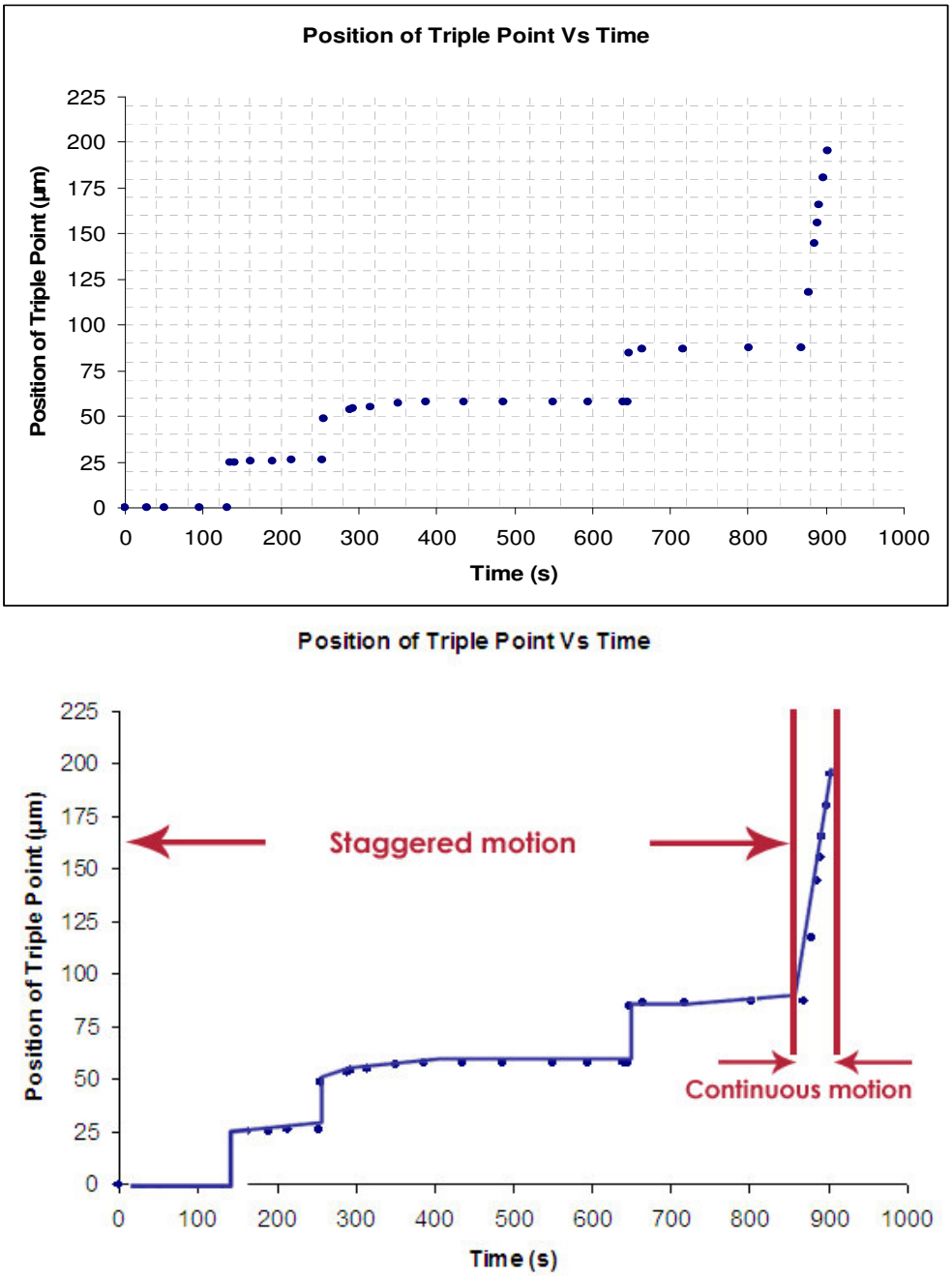

Figure 40 Movement of the delta-ferrite triple point, both staggered and continuous motion are evident

The rate of propagation of the delta-ferrite triple point during the period of continuous motion is approximately constant (3.3µm/s) as shown in Figure 41.

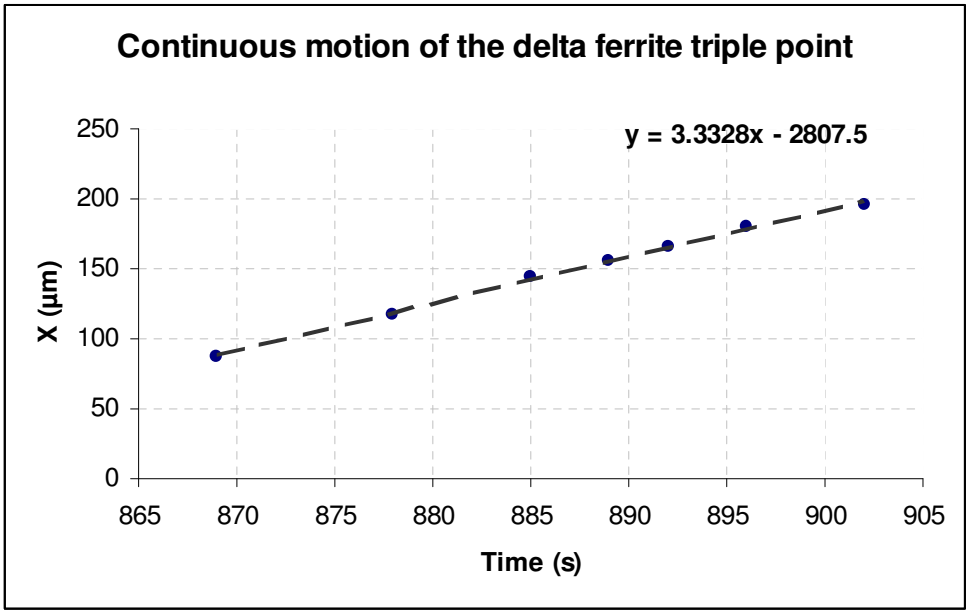

Figure 41 Progression of the delta-ferrite triple point during the period of continuous movement at the cooling rate of 5ºC/min

Repeating the experiment of cooling steel samples of the same composition from the delta-ferrite to austenite at a cooling rate of 5ºC/min, a new behaviour of grain boundary movement has been observed. Figure 42a illustrates the surface specimen at 1436ºC, consisting of three delta-ferrite grains and a stable triple point, undergoing the cooling rate of 5ºC/min. As cooling continues the triple point moves to a new place, showing a consistent continuous motion, Figure 42b. On further cooling the delta-ferrite triple point suddenly jumps to another position and then the transformation, Figure 42C. Additional cooling has shown that the austenite nucleates from this new location which proves that it is indeed the delta-ferrite triple point. The velocity of this rapid triple point movement is about 57µm/s which is significantly greater than 3.3µm/s, as calculated for consistent continuous motion.

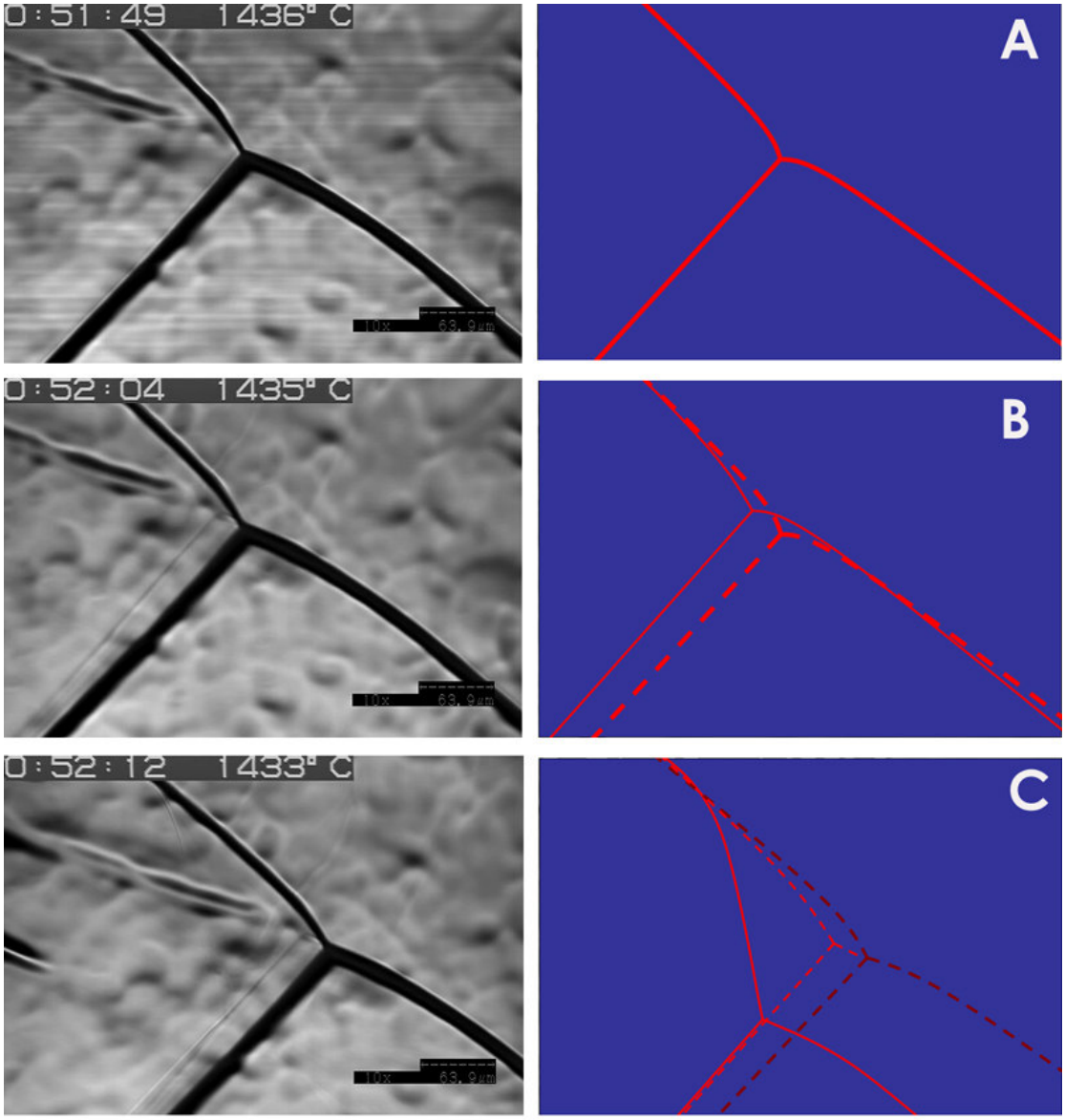

Figure 42 Delta-ferrite structure consisting of 3 grains and a triple point. Dash-line represents delta-ferrite grain boundary grooves while the solid lines are grain boundaries. (a) Delta-ferrite triple point before consistent continuous movement (b) Consistent continuous movement (c) Rapid movement

Previously it has been shown [60] that a temperature gradient is present in the LSCM samples and the bottom of the cylindrical specimen is colder than the top surface. Due to this thermal gradient, it is likely that the austenite grains nucleate at the bottom of the samples on cooling, before the transformation starts on the top (observed) surface. If this were true, then as the newly formed austenite grains develop along the anchored grain boundaries beneath the triple point, the local equilibrium at the delta-ferrite triple point on the surface will be disturbed, based on the Herring's equation, Figure 43.

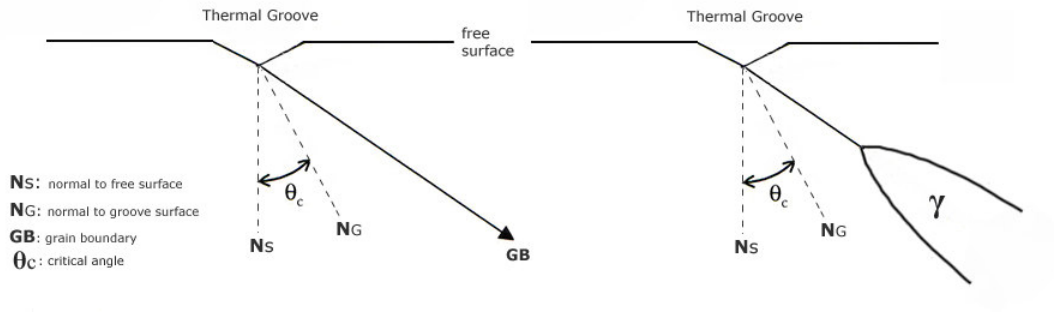

Figure 43 Unpinning effect of delta-ferrite triple points leading to rapid motion of the delta-ferrite triple point

Where N_S is the normal to the free surface, N_G is the normal to the notch surface and θ_C represents the critical angle.

Another interesting observation during the continuous motion of a triple point was that the relative position of the grain boundary changed during the movement of the triple point.

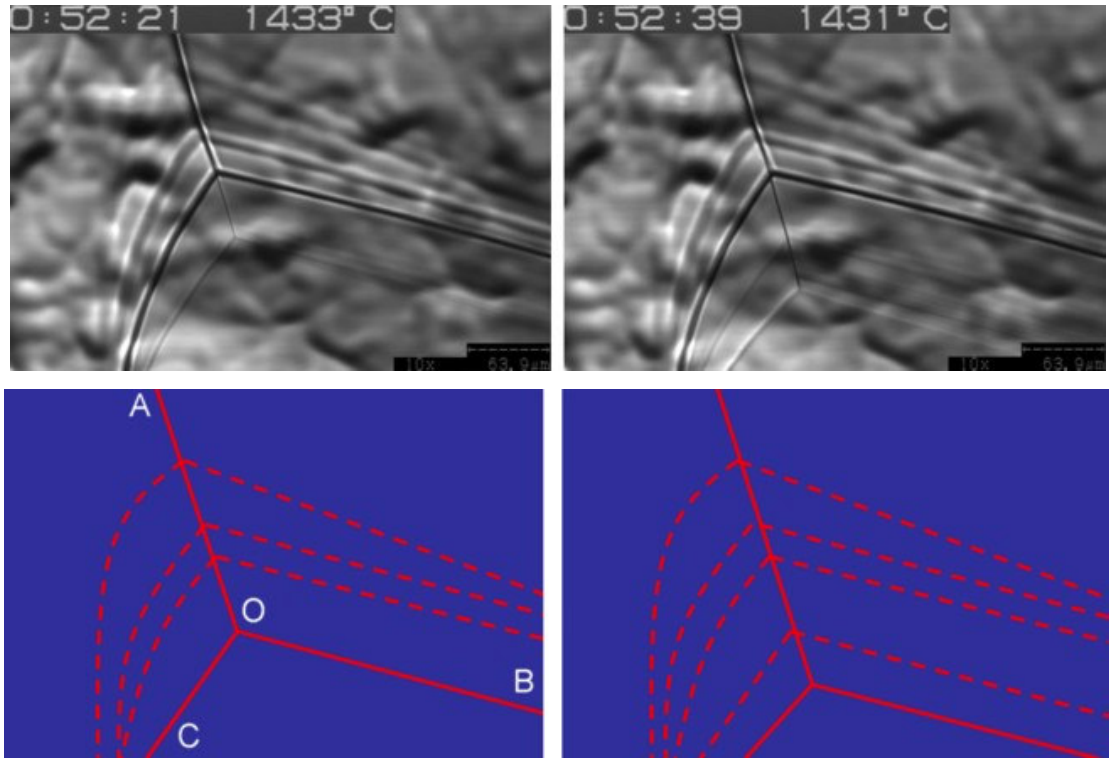

Figure 44 Continuous movement of a delta-ferrite triple point in the direction AO

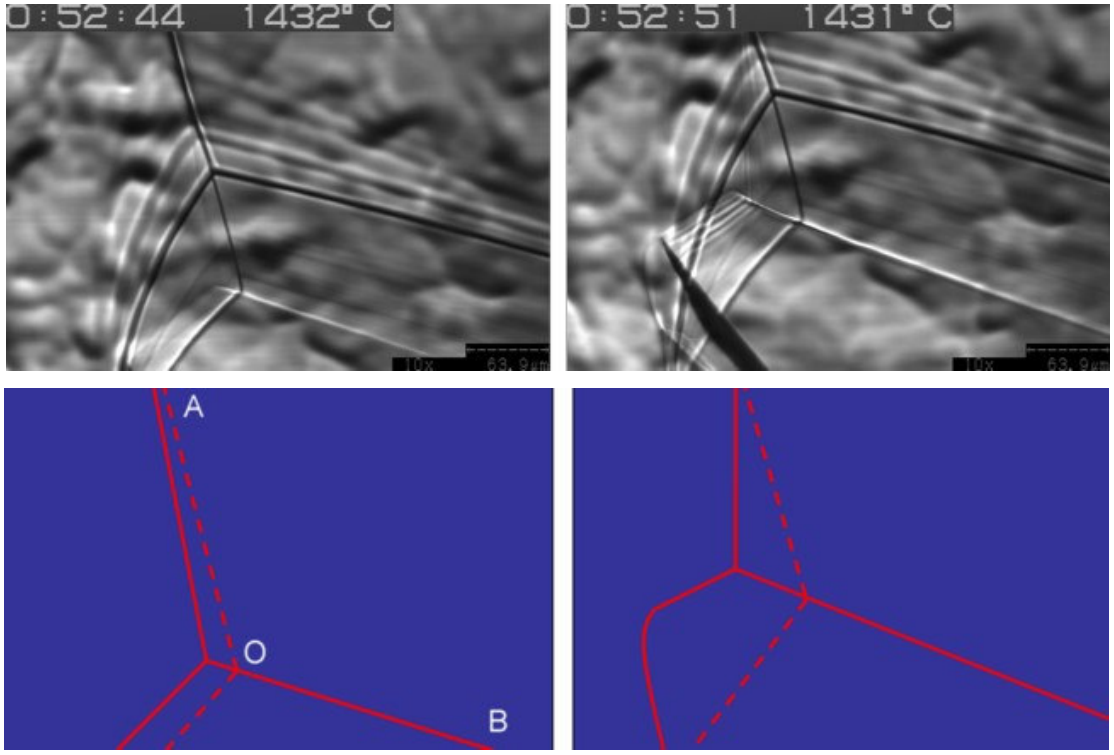

Figure 45 Change in the direction of a delta-ferrite triple point from AO to BO direction, 23 seconds after the start of continuous motion

The continuous movement of the triple point O, in the direction AO is shown in Figure 44. After 23 seconds, the triple point movement suddenly changed from AO to BO as shown in Figure 45. The observation could possibly be explained by a 3D effect which causes grain boundaries beneath the surface to alter the two-dimensional grain boundary arrangement on the top (observed) surface.

4.1.4 The delta-ferrite to austenite phase transformation morphology

The first nucleus of an austenite grain forms as specimen is cooled from within the delta-ferrite field into the delta-ferrite plus austenite two phase region. However it frequently happens that immediately before an austenite nucleates at a triple point, the δ-ferrite triple point moves rapidly away from the anchored position to a new position where the new austenite phase grows. This sudden movement of the triple point is depicted in Figure 46 where the initiation of the delta-ferrite to austenite phase transformation at a cooling rate of 5ºC/min is clearly shown. The nucleation of

austenite at delta-ferrite triple points has frequently been observed at low cooling rates (5ºC/min) as shown in this example.

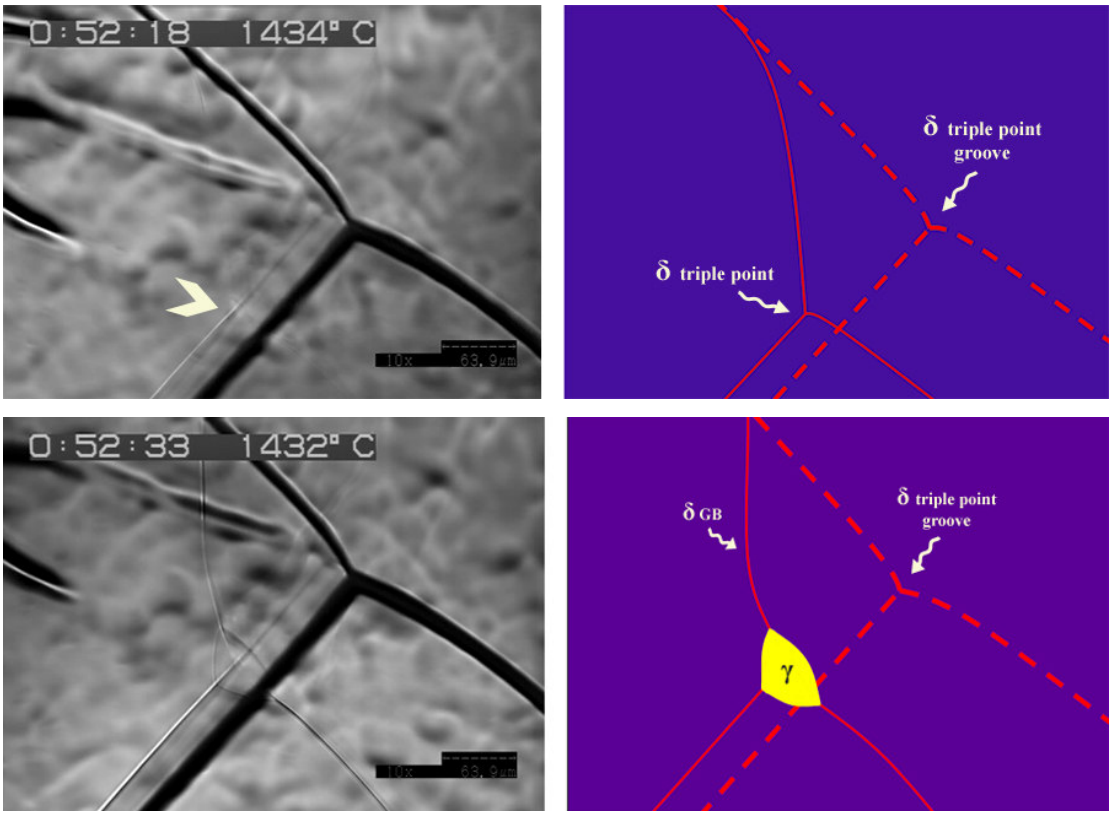

Figure 46 The delta-ferrite to austenite phase transformation morphology at a cooling rate of 5°C/min

Austenite nuclei precipitate (when they became thermodynamically stable) at δ-triple points mostly assuming a trihedral shape. The γ-phase then gradually grows along δ grain boundaries and into the matrix with a slightly curved but planar growth front. The δ-ferrite/γ phase transformation front does not seem to progress at a uniform rate during the phase transformation. Real-time observations of the moving δ/γ interface are depicted in Figures 47 and 48. The arrows point to the δ/γ interface being followed. Also shown in these figures, are the time of observation and the distance that the interface moved. The relative positions of this interface as a function of time are better shown in Figure 49. It is evident that following a sudden movement of the interface, it remains stationary for about 300 seconds before it takes off and progresses at a rate of approximately 2.5µm/s.

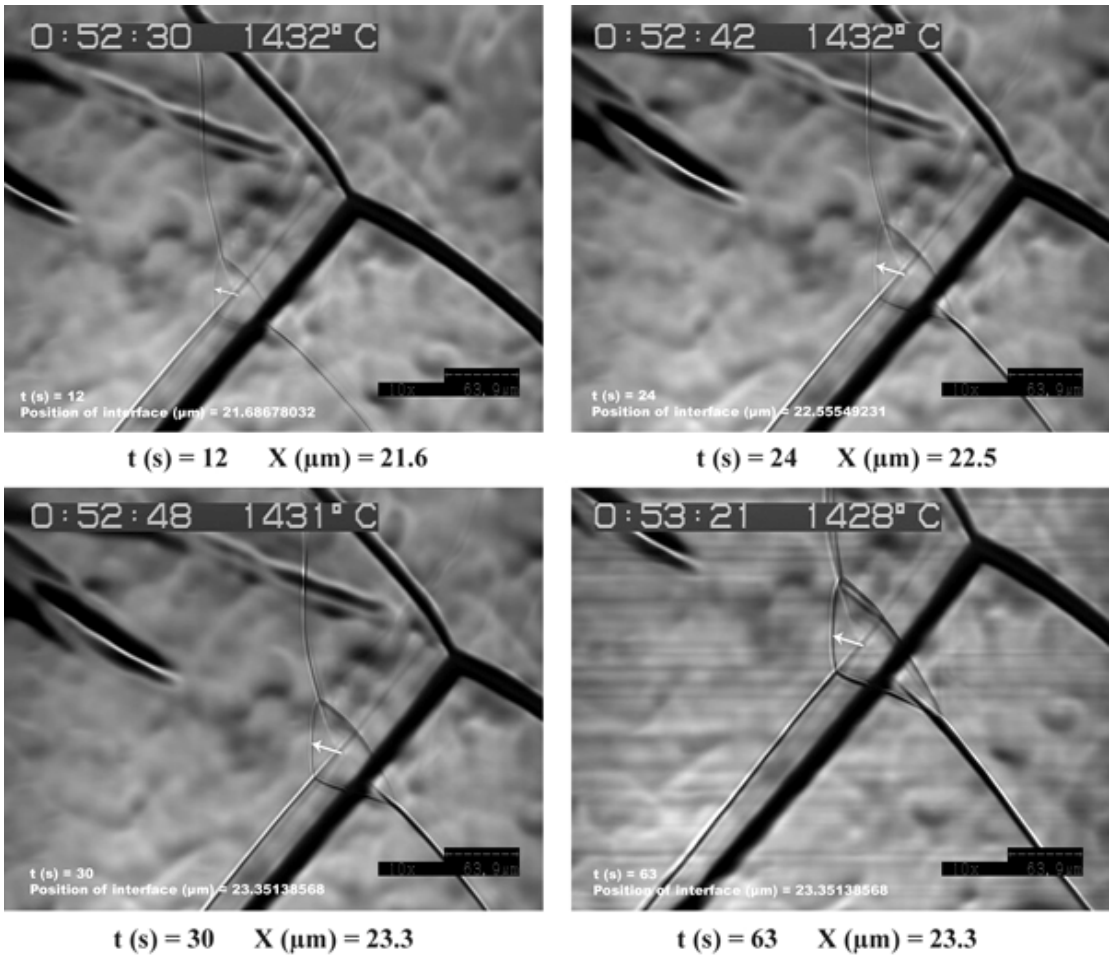

Figure 47 The first stage of the δ-ferrite/γ phase interface development during the growth of the newly-formed austenite nucleus

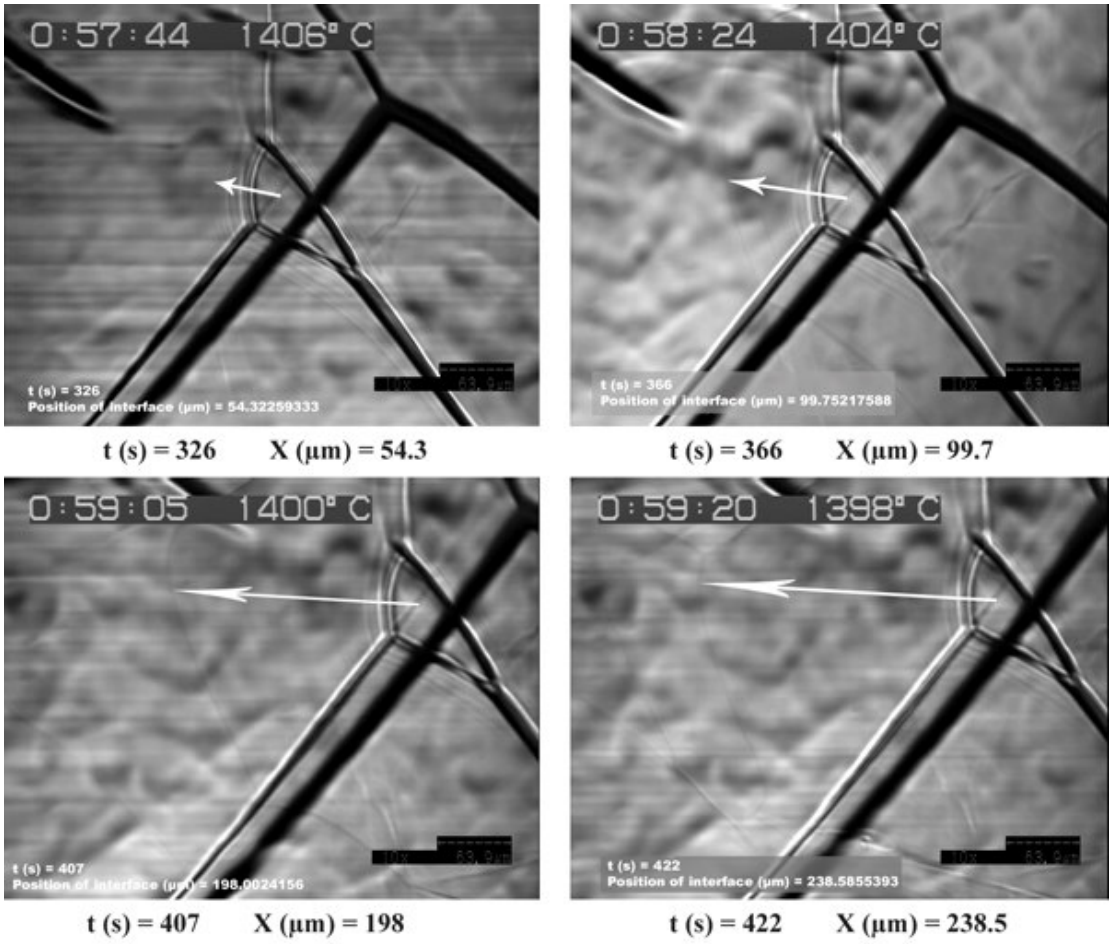

Figure 48 The second stage of the δ-ferrite/γ phase interface development as the austenite grain grows

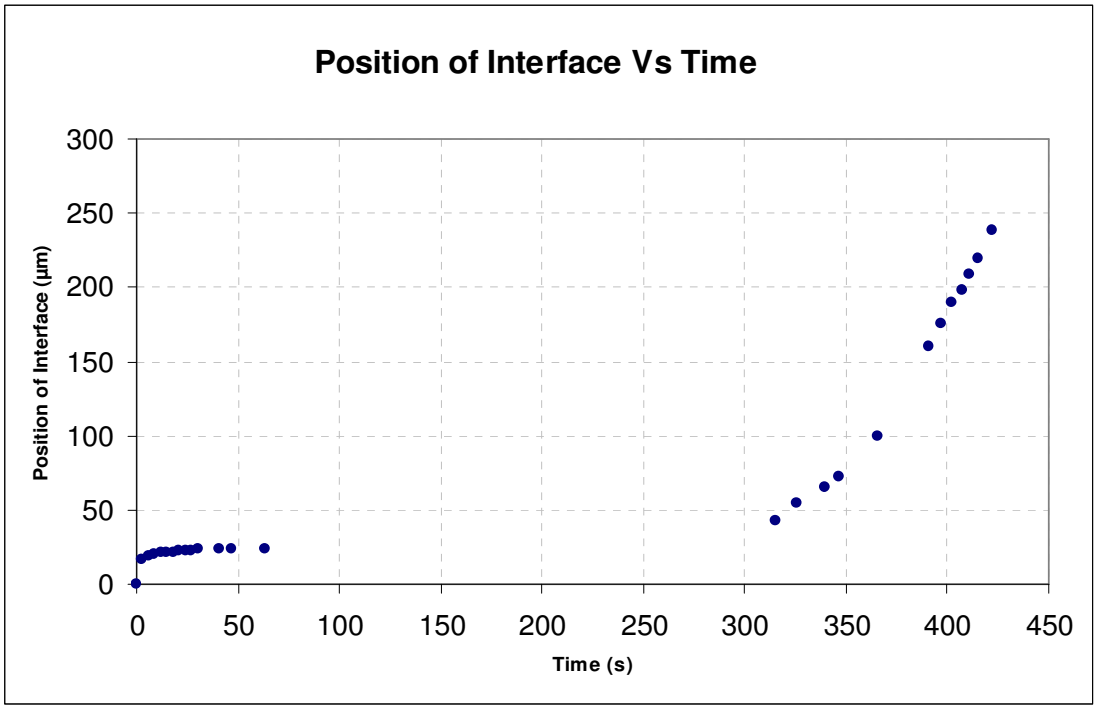

Figure 49 The progression of the δ-ferrite/γ phase transformation interface at a cooling rate of 5°C/min

Figure 50 shows the propagation velocity of the δ/γ interface of a newly formed γ grain into the δ-ferrite matrix. During the first stage, the propagation velocity reduces to a plateau about 10 seconds after initiation of the δ/γ phase transformation. The interface then remains stationary for about 315 seconds until the δ/γ interface starts to move again.

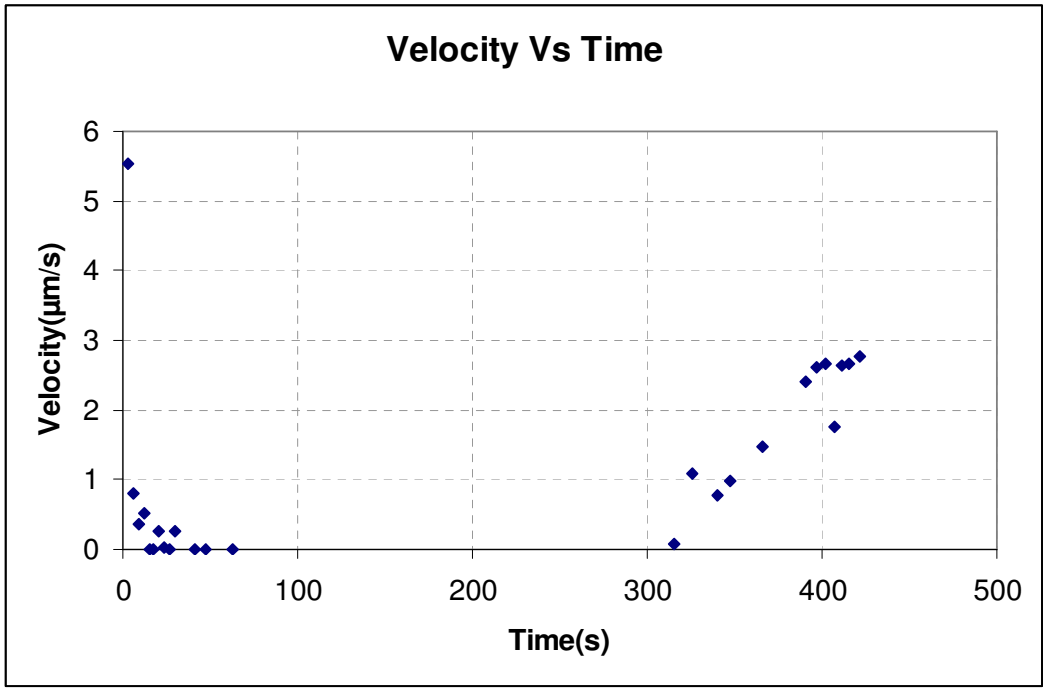

Figure 50 Propagation velocity of γ into the δ-ferrite matrix during the δ-ferrite/γ phase transformation at a cooling rate of 5°C/min

During the second stage of the δ/γ interface movement, the velocity of the interface increases linearly with a constant acceleration of approximately 23nm/s^2, Figure 51.

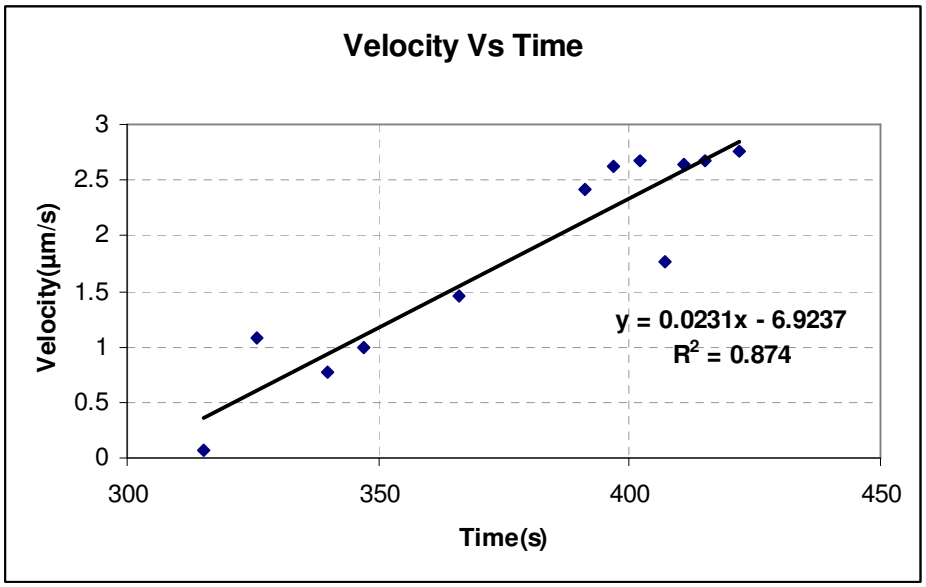

Figure 51 The propagation velocity of γ into the δ-ferrite matrix during the second stage of austenite propagation at 5°C/min cooling rate

4.1.5 Simulation of the δ-ferrite/γ phase transformation at a cooling rate of 5°C/min

In order to support the experimental observations, the growth of an austenite grain that nucleated on a delta-ferrite grain boundary and being cooled at a cooling rate of 5°C/min has been analysed using the phase-field model, MICRESS. Figure 52 shows a simulated microstructure comprising three delta-ferrite grains that form a triple point. The simulation is initiated by defining two nucleation sites on a delta-ferrite grain boundary. The phase-field model then allows the two austenite grains to grow at a rate determined by the thermodynamic driving force and the rate of diffusion. The parameters used in the simulation are shown in Table 7. It is important to emphasize that the MICRESS phase-field model merely provides a mathematical solution to the coupled differential equations describing the thermodynamic driving force for the phase transformation and the equation of diffusion of carbon. All the parameters and boundary conditions are externally defined.

Table 7 Thermodynamic Data

Parameter	Value	Unit	Reference
T_0 reference temp.	1810.15002	K	Thermocalc
Entropy of Trans.	1.10000002	J/cm^{3}K	Thermocalc
T_0 reference temp.	1799.15002	K	Thermocalc
Entropy of Trans.	1.10000002	J/cm^{3}K	Thermocalc
T_0 reference temp.	1665.15002	K	Thermocalc
Entropy of Trans.	1.10000002	J/cm^{3}K	Thermocalc

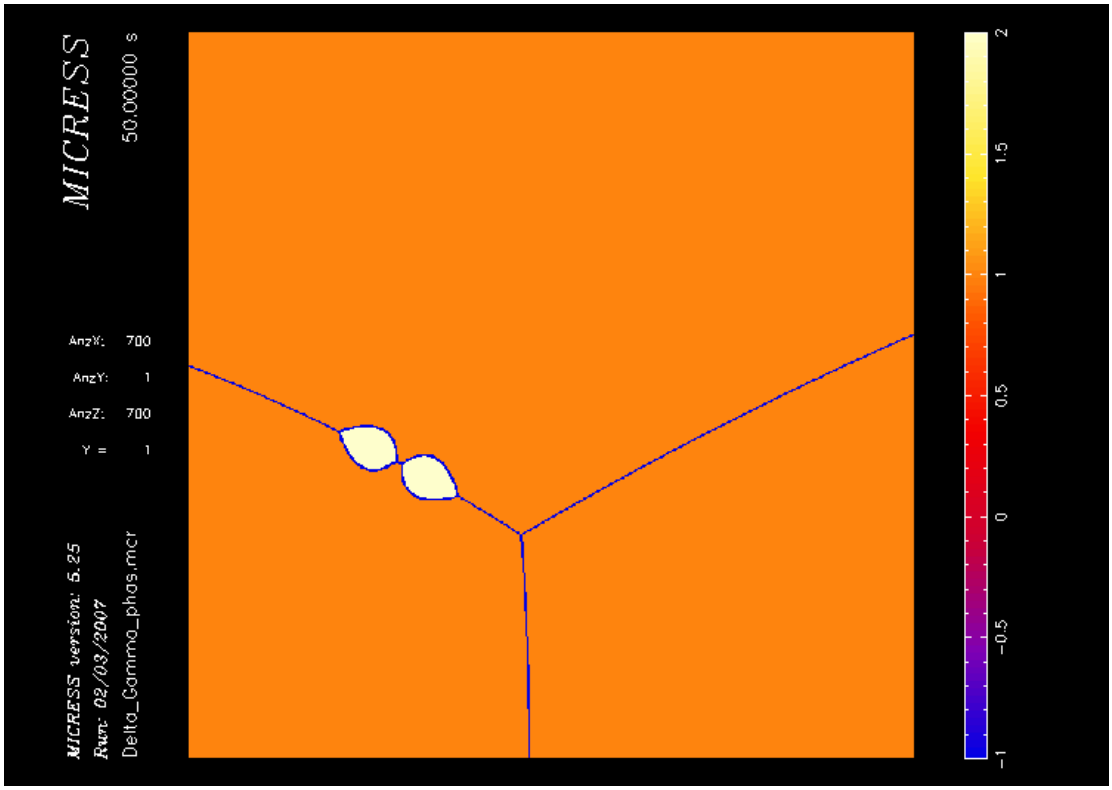

Figure 52 MICRESS simulation of the δ-ferrite/γ phase transformation showing early growth of the austenite grains that nucleated on a delta-ferrite grain boundary

The γ-phase gradually grows along δ grain boundaries and into the matrix with a slightly curved but planar growth front similar to the experimental observations shown in Figure 46.

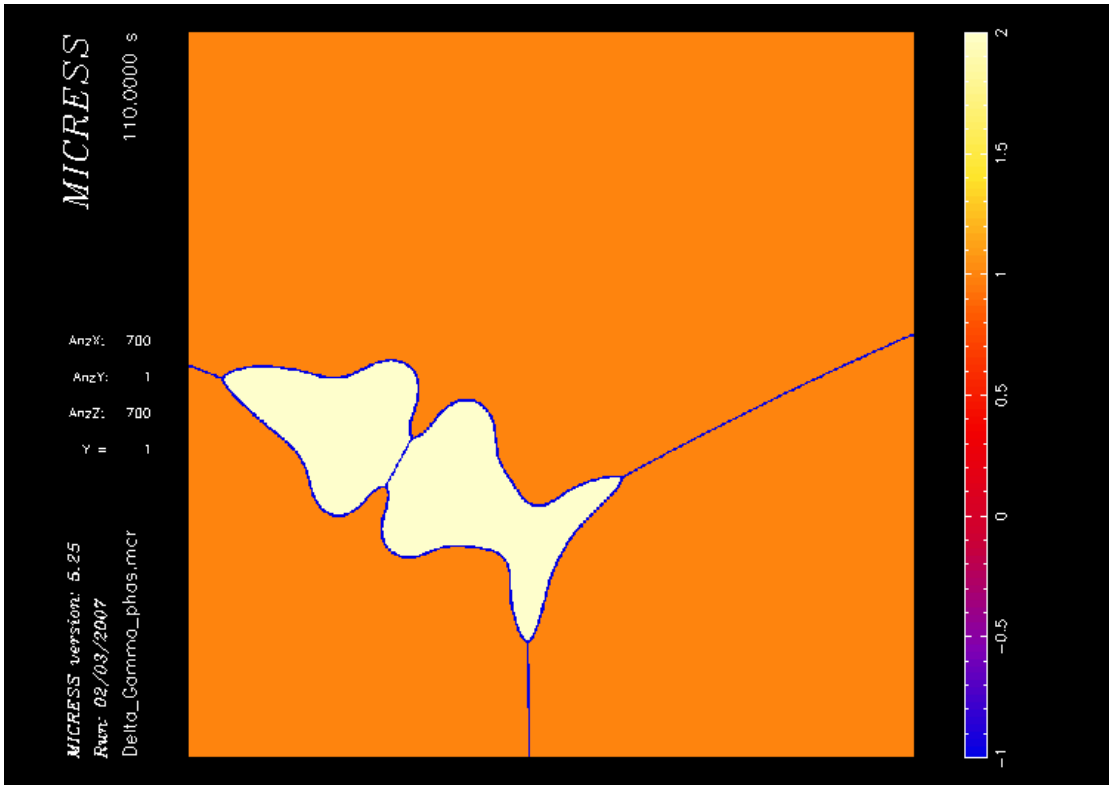

Figure 53 MICRESS simulation of the propagation of austenite phase into the δ-ferrite matrix.

The MICRESS-predicted morphology and growth of the newly formed austenite is in agreement with the experimental findings. However it is more difficult to explain why an austenite grain that has nucleated and grew to a certain size would suddenly terminate growth although the system is being cooled at 5ºC/min and only grow further after being stationary for 300 seconds. Closer examination of the Fe-C diagram reveals that the first austenite nucleus that forms might contain about 0.09%C. The ferrite in the adjoining matrix therefore has to be significantly depleted in carbon to allow the austenite to grow. With further cooling, the equilibrium carbon content of the austenite decreases until it eventually becomes the same as the bulk ferrite composition. It therefore seems that the growth of the initial austenite grain is arrested by a lack of supply of carbon. As the temperature is decreased, less carbon is required to ensure thermodynamic stability of the austenite, the kinetic barrier of insufficient carbon supply diminishes and the austenite will start to grow again at an ever increasing rate, driven by the thermodynamic driving force. This explanation of the experimental observations is essentially in agreement with the model proposed by Yin *et al.*[32], as discussed earlier.

In order to test this premise, further phase-field modelling was conducted. Figure 54a shows the carbon concentration profile through and in the vicinity of a small austenite nucleus. Following nucleation at a delta-ferrite grain boundary, the austenite nucleus is allowed to grow and the carbon profile, 105 seconds later is shown in Figure 54b. It is evident that there is a significant carbon gradient in the adjoining ferrite matrix. On further cooling less and less carbon is required to ensure thermodynamic stability of the austenite and when the temperature drops into the single-phase austenite region, the austenite has the same carbon content as the bulk ferrite matrix and hence, can grow purely under the thermodynamic driving force, unimpeded by the kinetic restraints of carbon supply.

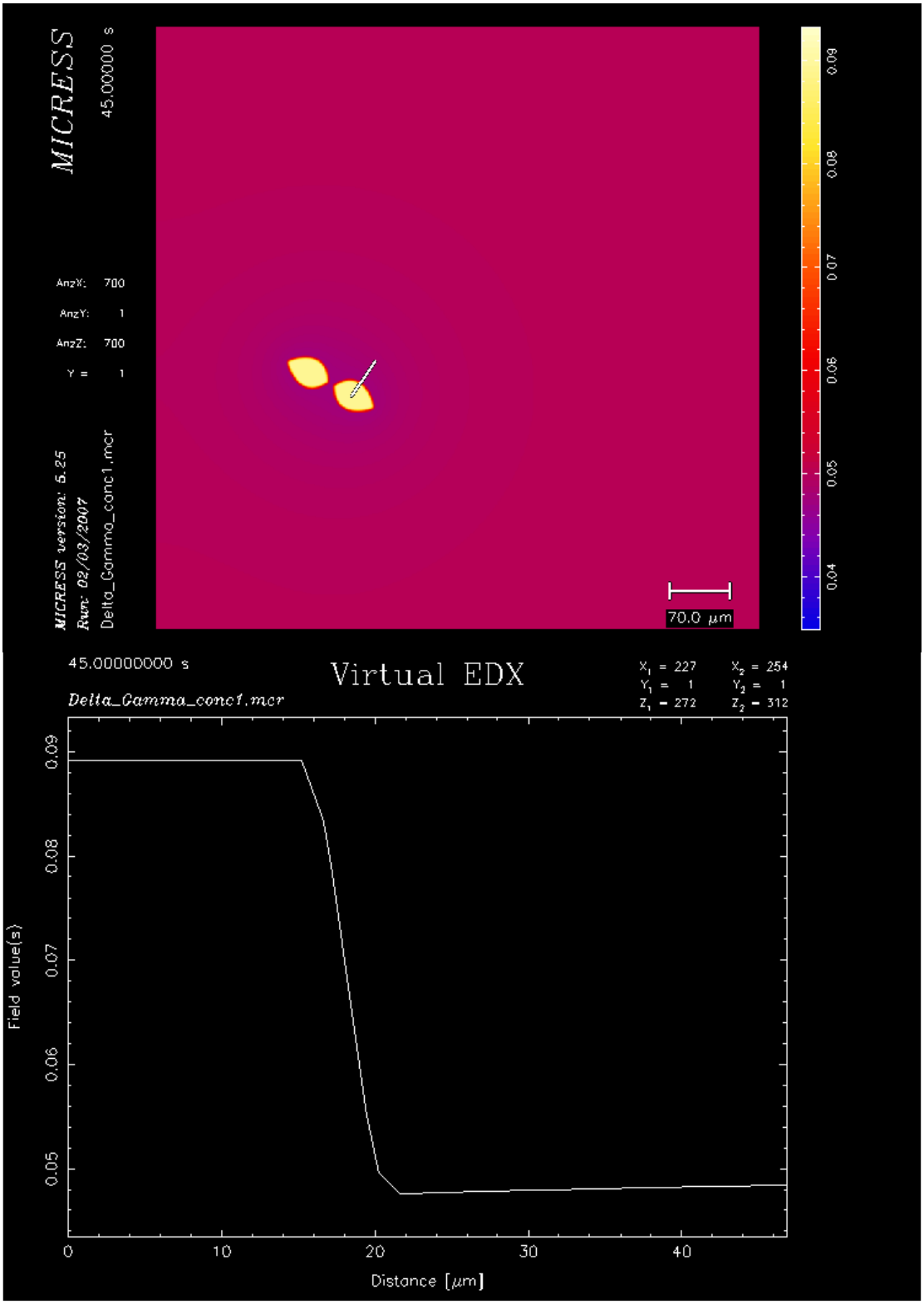
MICRESS
45.00000 s
AnzX: 700
AnzY: 1
AnzZ: 700
Y = 1
MICRESS version: 5.25
Run: 02/03/2007
Delta_Gamma_conc1.mcr
70.0 µm
0.09
0.08
0.07
0.06
0.05
0.04
45.00000000 s
Virtual EDX
Delta_Gamma_conc1.mcr
X1 = 227
Y1 = 1
Z1 = 272
X2 = 254
Y2 = 1
Z2 = 312
Field value(s)
0.09
0.08
0.07
0.06
0.05
0
10
20
30
40
Distance [µm]

(a)

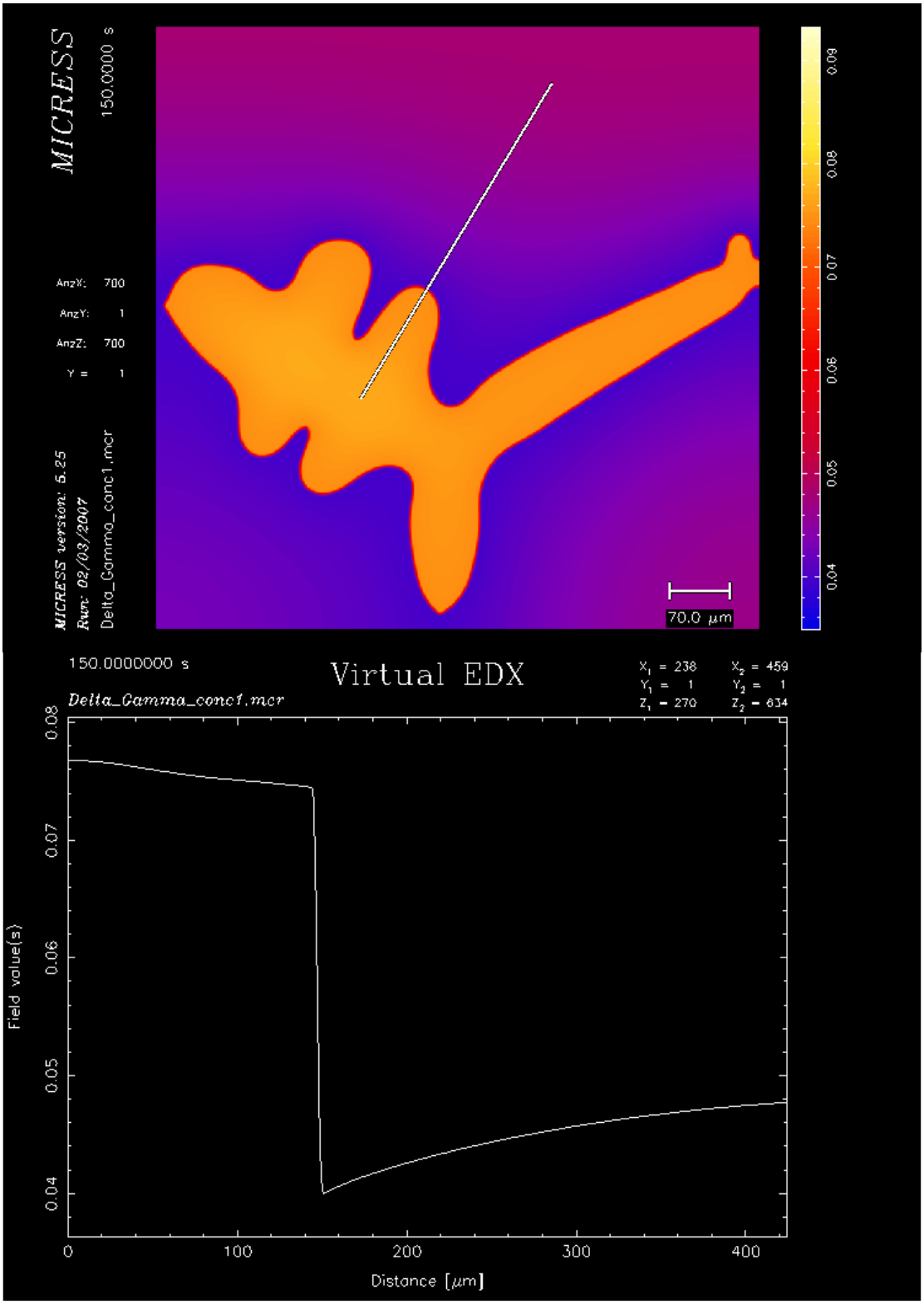

(b)

Figure 54 MICRESS simulation of carbon concentration gradient during the δ-ferrite/γ phase transformation at 5°C/min cooling rate

(Refer to Appendix 3 for more Micress simulations of the carbon concentration gradient during the δ-ferrite/γ phase transformation at 5°C/min cooling rate)

Figure 55 shows that, when the first austenite nucleus forms at temperature T_a , it would contain about 0.089 percent carbon. In order for the austenite to reach this carbon content, the adjacent delta-ferrite domain must be depleted of carbon. While the austenite grain grows, more carbon is required to be transferred from the delta-ferrite matrix. Accordingly, the delta-ferrite becomes more and more depleted of carbon. The carbon supply becomes insufficient to sustain austenite growth and hence, the growth of austenite is inhibited. On further cooling, say to temperature T_b, the carbon concentration difference between thermodynamically stable austenite and delta-ferrite is reduced. As shown in the Fe-C phase diagram, it will thus be easier for the remaining delta-ferrite to supply sufficient carbon for austenite to grow. At temperature T_c, the carbon content of thermodynamically stable austenite is 0.05%C (the same as that of the bulk delta-ferrite matrix) and hence, the supply of carbon from the matrix to the growing austenite grain is no longer the rate-determining step.

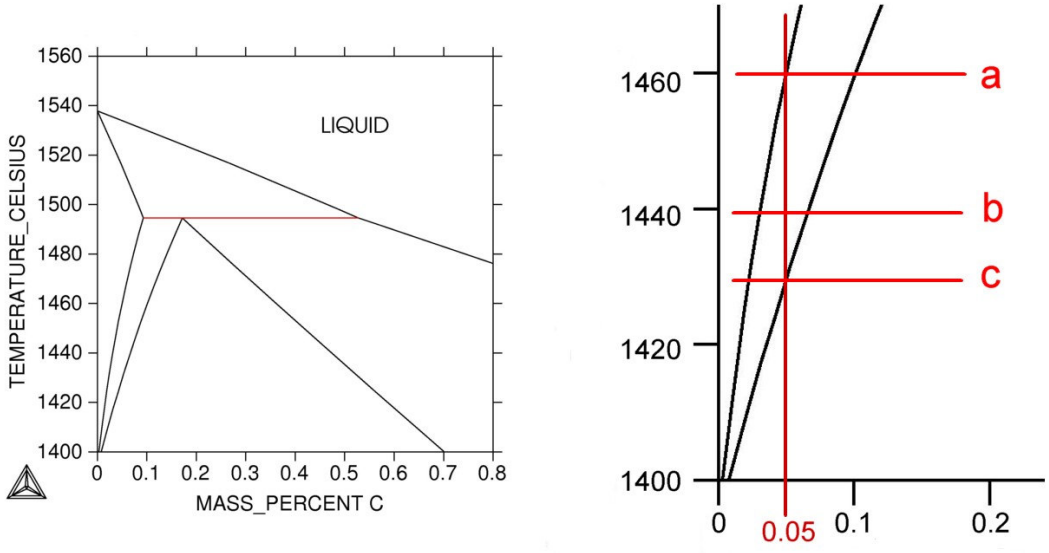

Figure 55 Iron-Carbon phase diagram, horizontal lines suggest that during the δ/γ phase transition, the initial delta-ferrite nuclei forms with a high carbon content. As the further cooling continuous the carbon content difference between the delta-ferrite and austenite decreases

4.2 Group 1 - 10°C/min cooling rate

Liu *et al.* [55] observed that the morphology of the δ to γ phase transition is a function of the cooling rate. At a cooling rate of 19.8ºC/min, austenite nucleated and grew in a manner expected of diffusion controlled mechanisms. However, at a cooling rate of 600ºC/min, the nucleation and growth of austenite resembled a diffusionless behaviour. In this study we firstly wished to benchmark our observations against those of *Liu et al.* and secondly attempted to determine at what cooling rate the apparent change from diffusion-controlled to diffusionless behaviour occurs. The morphology of the δ to γ phase transition at a cooling rate much lower than that used by *Liu et al.* (5ºC/min as opposed to around 20ºC/min) was discussed in the previous photograph. Little change in the morphology of the precipitating γ at a cooling rate of 10ºC/min was observed. Figure 56 shows the propagation of one austenite grain into the delta-ferrite matrix with a curved front at a higher cooling rate of 10ºC/min. In Figure 56 the delta ferrite triple point has moved from point A to point B (leaving a groove) where it is being pinned by a group of small grains, before the austenite grain nucleated on a the delta-ferrite grain boundary. Another austenite grain now propagates (from the left of the photograph) along the delta-ferrite grain boundary with a sharp front and linear sides.

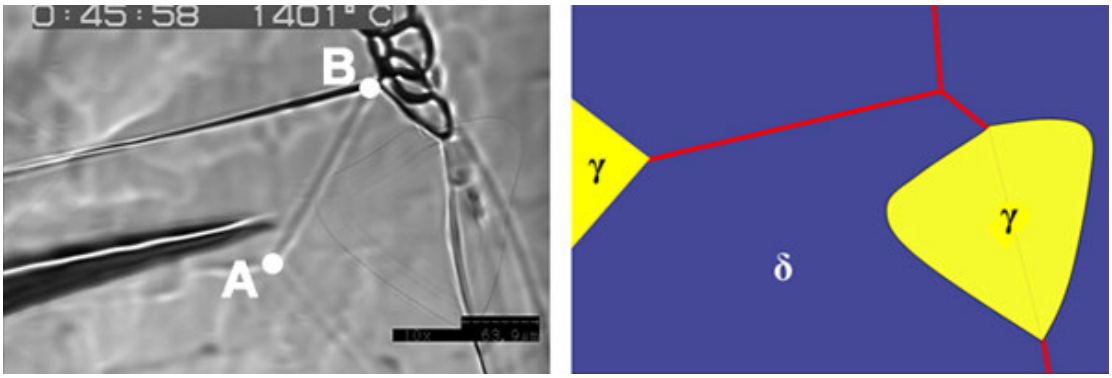

Figure 56 The delta-ferrite to austenite phase transformation morphology at a cooling rate of 10°C/min

The progression of the austenite grain that has nucleated on the δ-ferrite grain boundary and its growth into the delta-ferrite matrix is more clearly shown by the arrows in Figure 57.

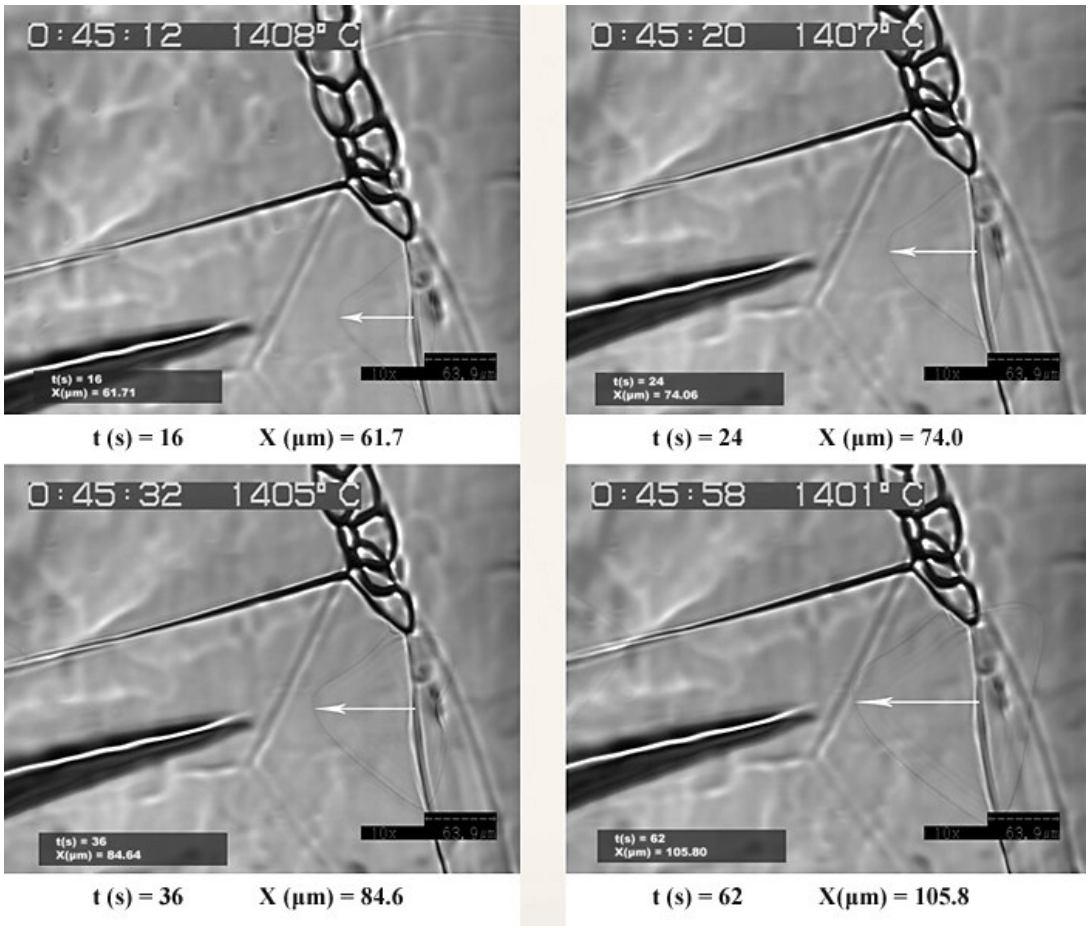

Figure 57 The position of the phase transformation interface during δ-ferrite to austenite phase transformation

The position of the progressing front (indicated by the arrow tips) is plotted as a function of time in Figure 58 and Figure 59 shows the velocity of this progressing interface as a function of time.

It is evident that the δ/γ interface progress initially at a rate of about 12µm/s but this rate of progression gradually decreases until a steady growth rate of about 1µm/s is attained. This behaviour is distinctly different from that observed at a cooling rate of 5ºC/min where the δ/γ interface progressed in a stop-start fashion.

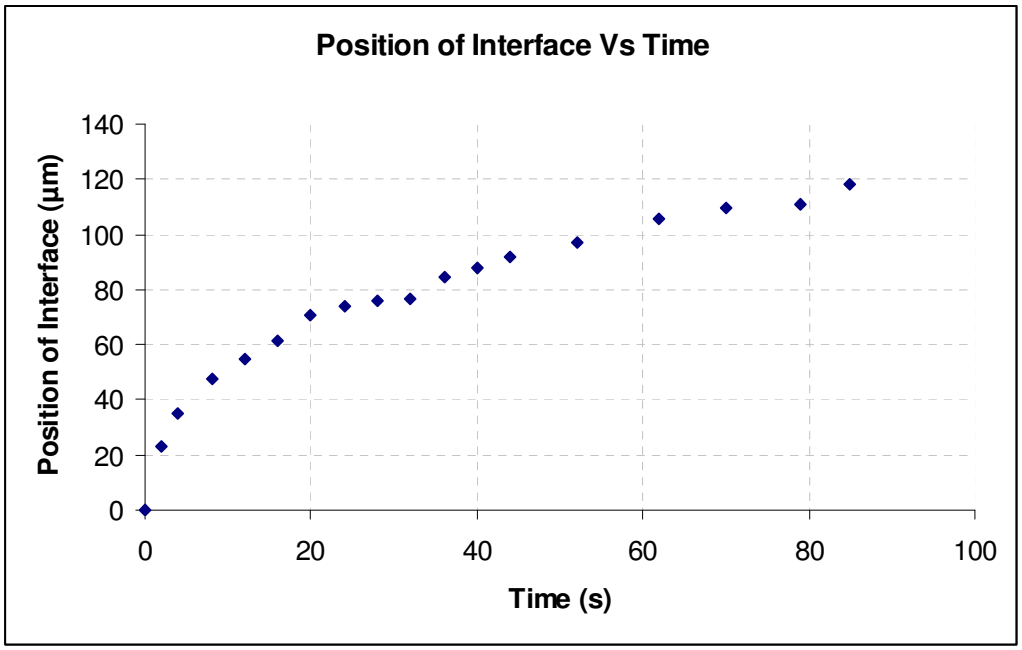

Figure 58 Progression of the δ-ferrite/γ interface of a grain that nucleated on an austenite grain boundary and grows into the δ-ferrite matrix. Cooling rate: 10°C/min

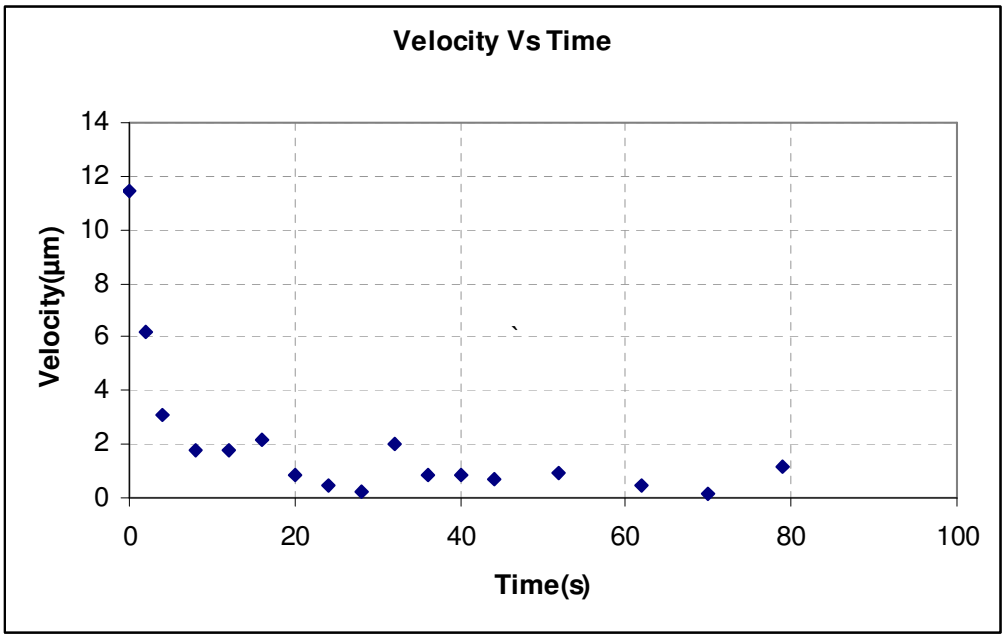

Figure 59 The propagation velocity of the δ-ferrite interface (refer to Figure 58)

The austenite grains that grow along the δ-ferrite grain boundary, shown in Figure 56, progress at different rate rates. For the sake of clarity, the simultaneous growth of these two grains is shown in Figures 60 and 61. The relative positions of the interfaces are normalized and the zero point of the measurements is shown in the Figure 60.

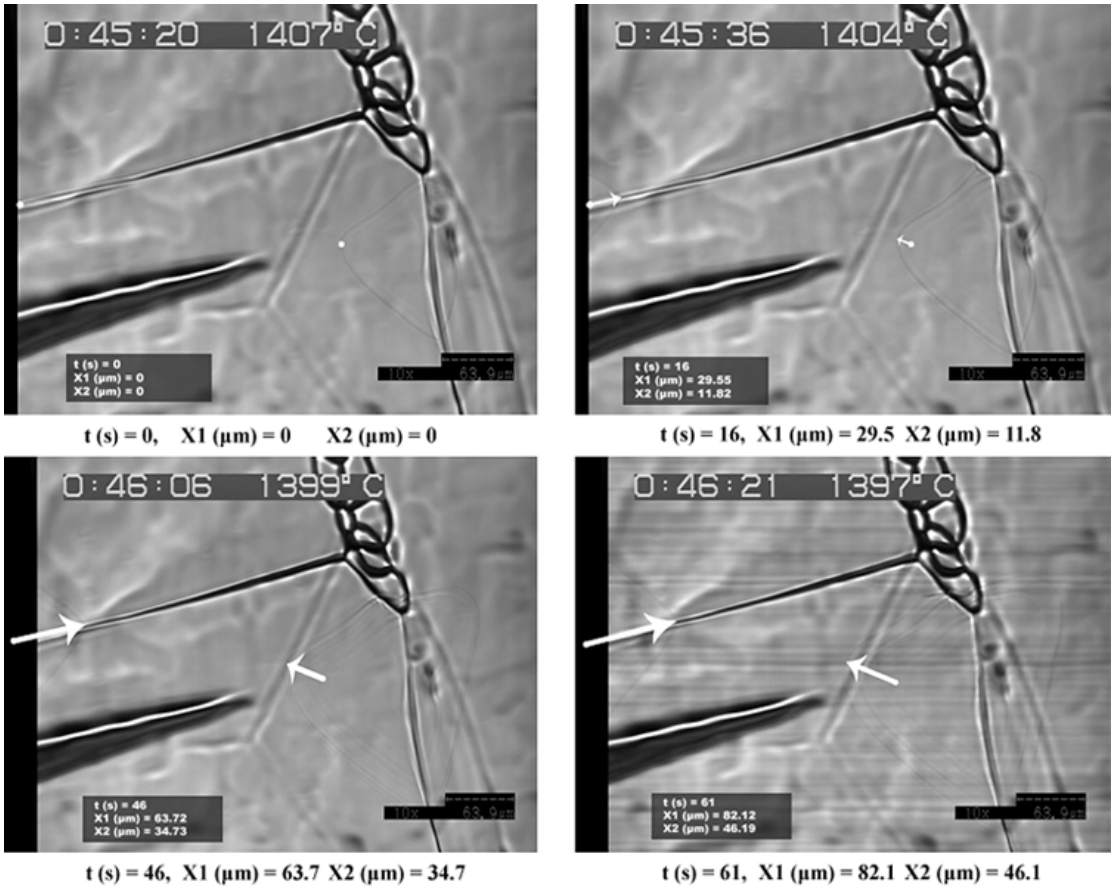

Figure 60 The progression of austenite along the delta-ferrite GBs and into the δ-ferrite matrix

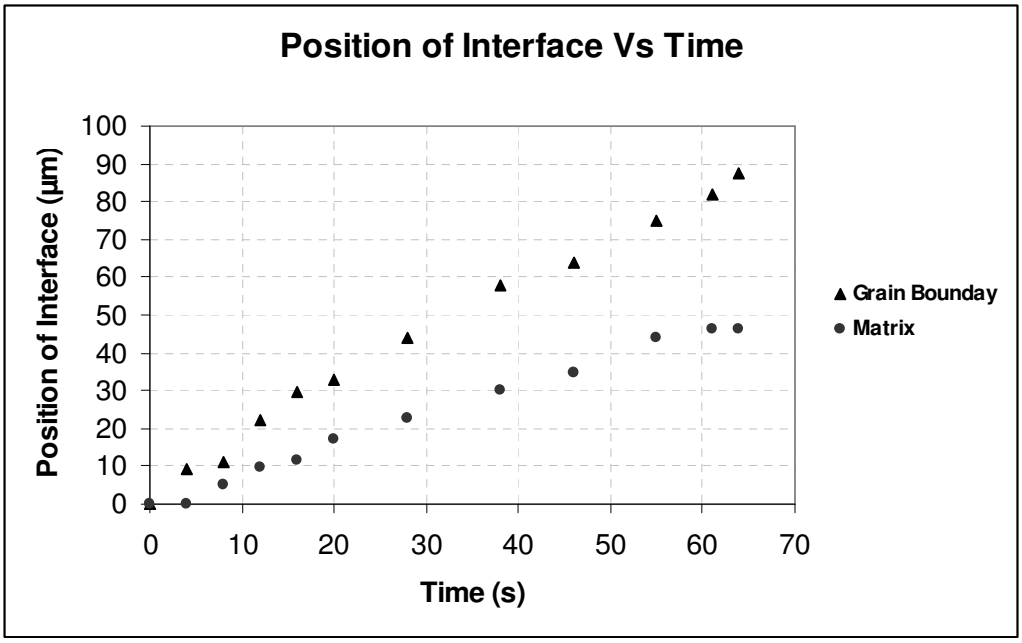

Figure 61 Progression of the δ/γ interface along the delta-ferrite GBs and into its matrix (note the zero point of the measurement shown in Figure 60)

Figure 61 clearly shows that the austenite grows at a higher rate along the δ-grain boundaries than within the matrix. Initially, γ-grains propagate along δ-grain

boundaries at a much higher rate than into the matrix, but the relative propagation velocities stabilize after about 20 seconds, as shown in Figure 62. However, the growth rate of austenite along delta-ferrite grain boundaries remains about twice as high as into the matrix.

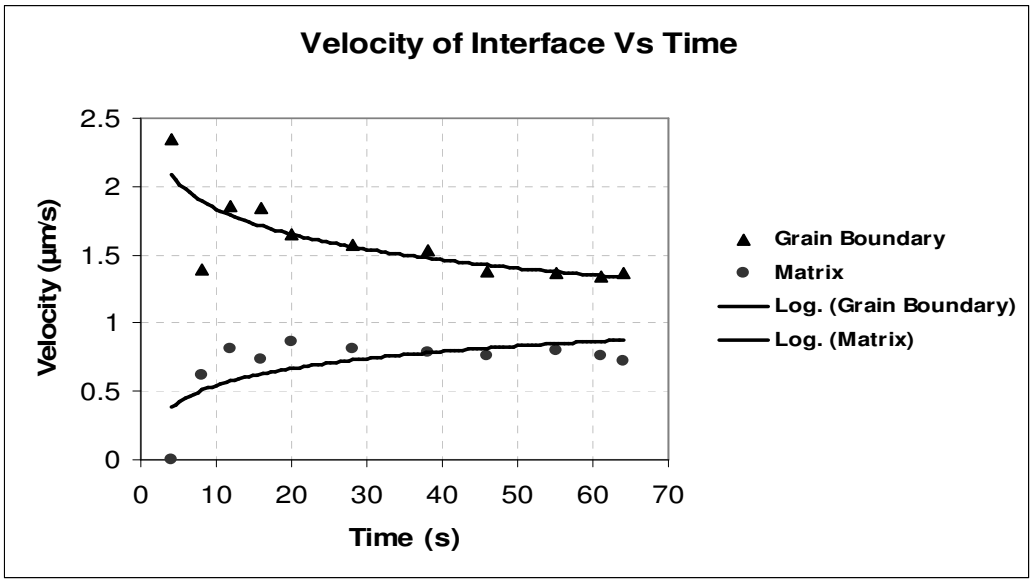

Figure 62 Velocity of the δ/γ interface along the grain boundary and into the matrix

4.3 Group 1 - 15°C/min cooling rate

At a cooling rate of 15°C/min, austenite grains nucleate on delta ferrite grain boundaries with a combination of dihedral morphology (the same as at the lower cooling rates) and finger-type morphology, Figure 63. The δ-ferrite grain boundary is slightly curved, indicating that the grain boundary has moved from its stable (deeply grooved) position, just prior to the nucleation of the austenite grain.

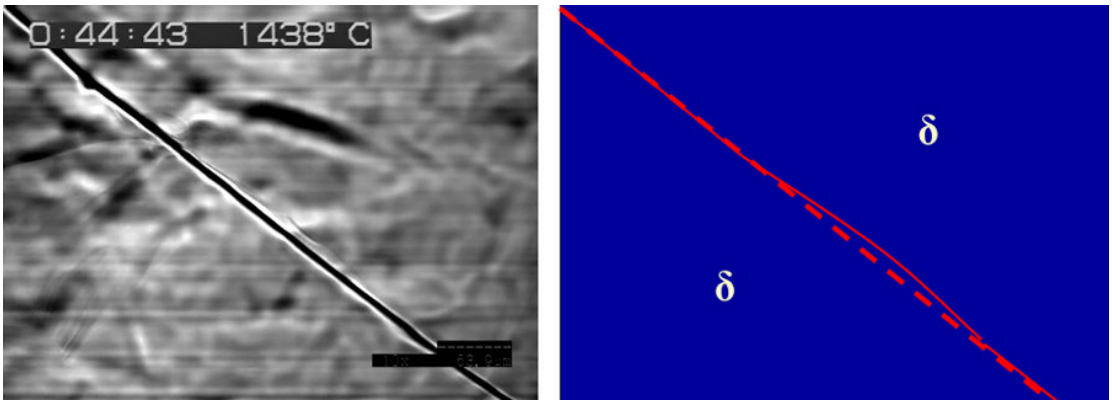

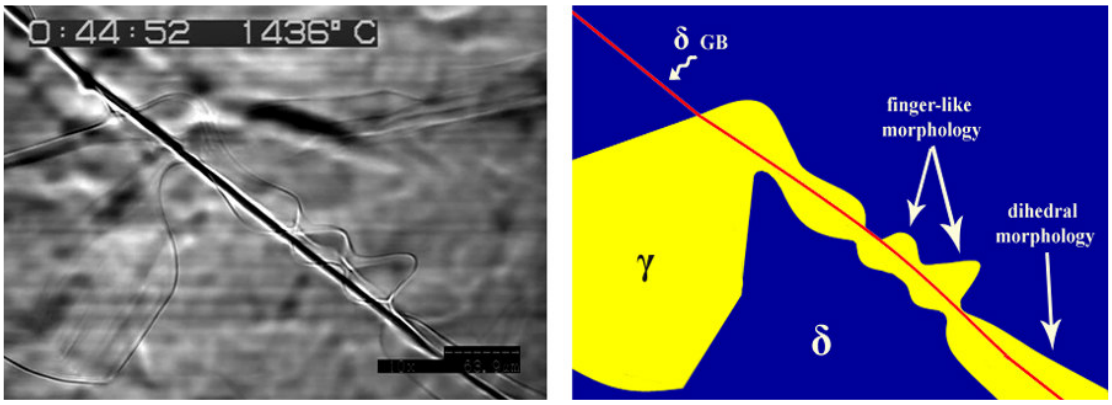

Figure 63 The delta-ferrite to austenite phase transformation morphology at a cooling rate of 15°C/min

On further cooling the austenite grains that formed on δ-ferrite grain boundaries eventually impinge and a fully austenitic microstructure is stabilized. Grooves of the prior δ-ferrite can still be observed on the surface of the newly formed austenite and the relation between the δ-ferrite grains and the newly formed austenite grains is clearly delineated in Figure 64a. On further cooling Widmanstätten ferrite plates nucleate and grow from the austenite grain boundaries as shown in Figure 64b providing convincing evidence that the triple point shown in Figure 64a is indeed a γ triple point.

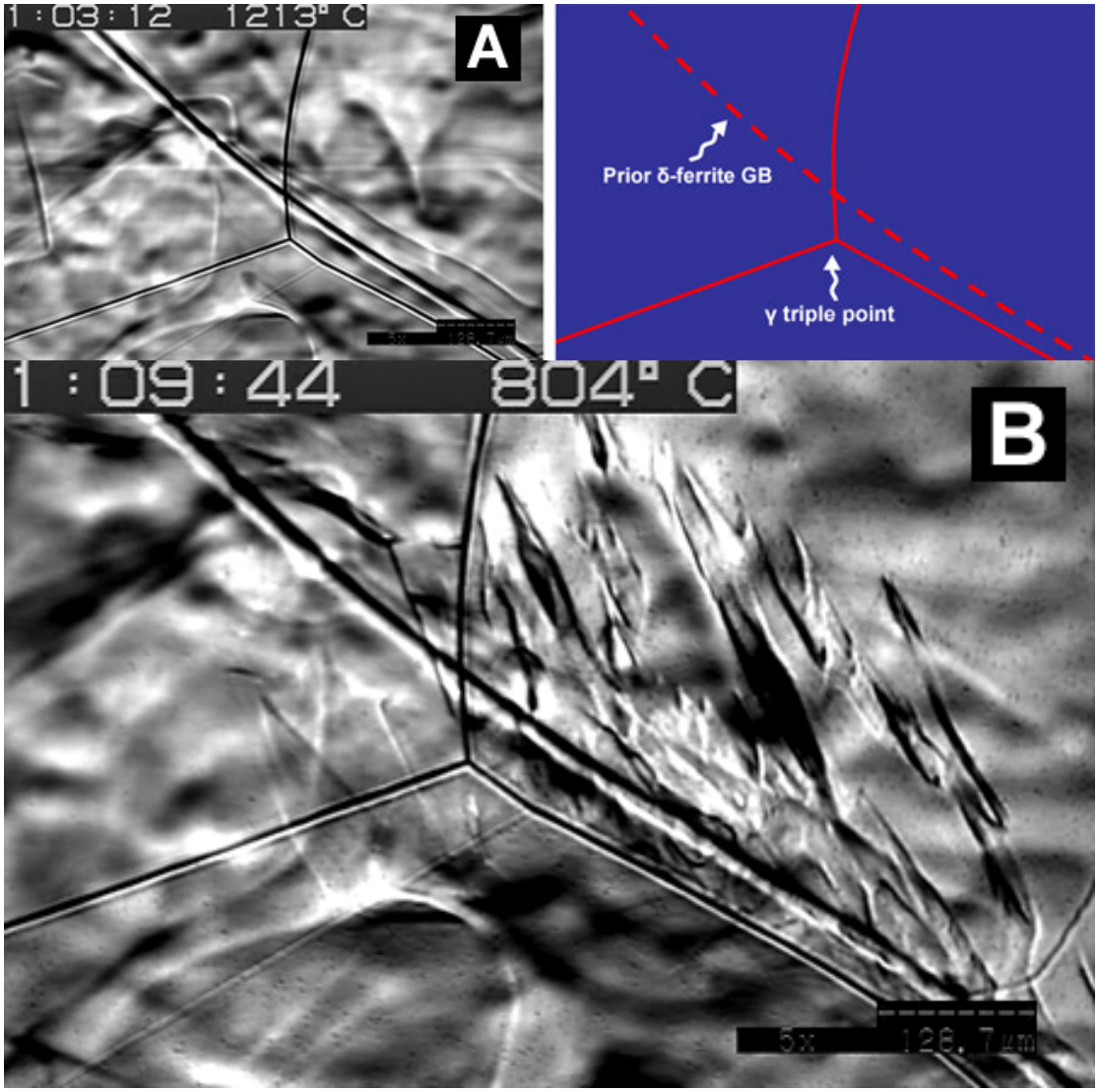

Figure 64 (a) Stabilized austenite structure and grooves of a prior δ-ferrite growing boundary (b) growth of Widmanstätten ferrite plates from the austenite grain boundaries

4.4 Group 1 - 30°C/min cooling rate

At a cooling rate of 30ºC/min, austenite nucleates at and grows from delta-ferrite triple points and grain boundaries. An example of such nucleation and growth is shown in Figure 65.

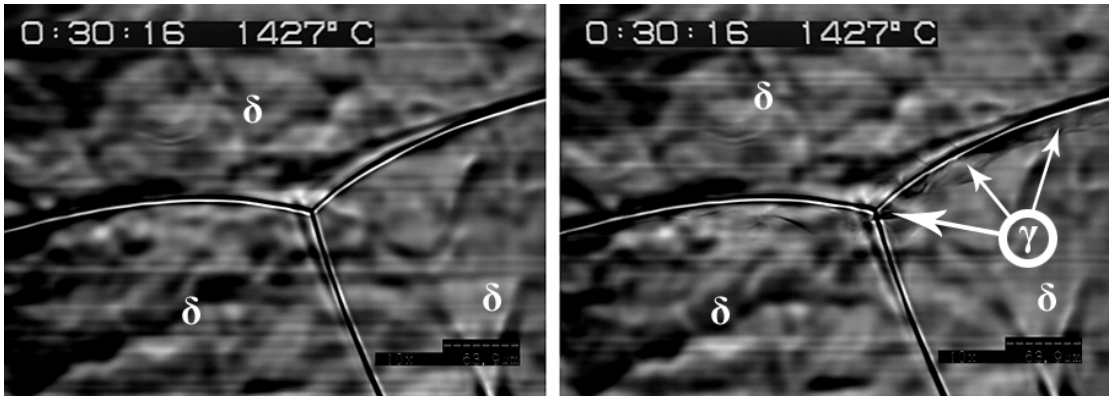

Figure 65 Nucleation of austenite from a delta-ferrite triple point and grain boundaries

Dihedral and finger-like austenite morphologies are present at the initiation of the δ/γ phase transformation. Austenite also nucleates within the delta-ferrite matrix on the surface of the specimen in an island-like morphology and these nucleation suites are not associated with any delta-ferrite grain boundaries or triple points on the surface, as shown in Figure 66. Island-like nuclei are likely to have nucleated from grain boundaries and triple points below the surface.

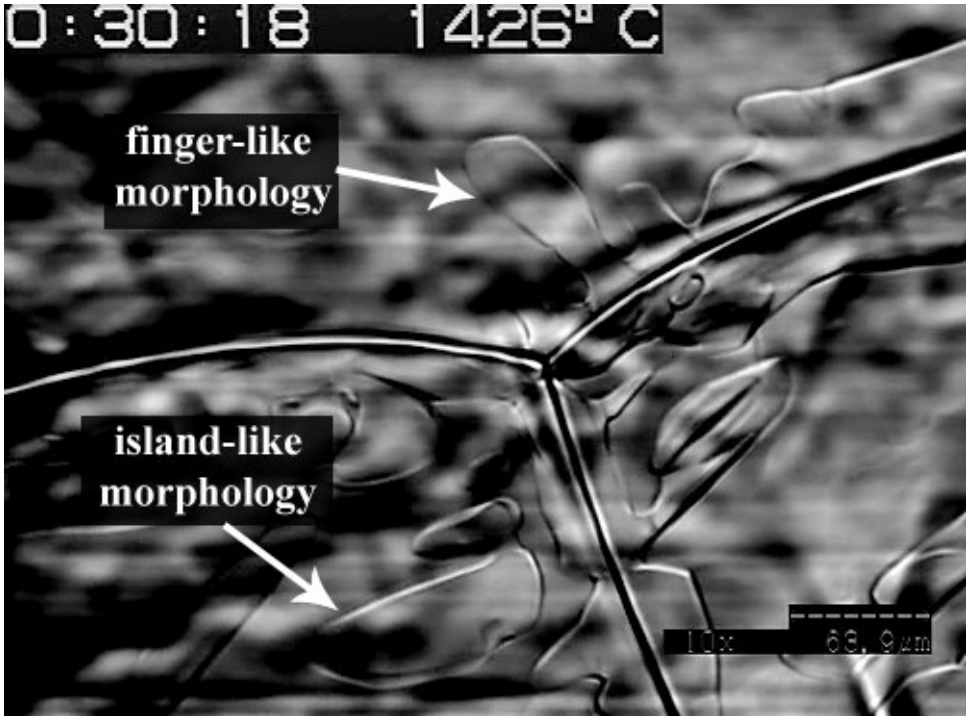

Figure 66 The delta-ferrite to austenite phase transformation morphology at a cooling rate of 30°C/min

When the specimen enters the δ+γ two phase region, the finger-like austenite precipitates form very rapidly, within a second following the initiation of the phase transformation. Figure 67 illustrates one of the austenite fingers which have

developed into the delta-ferrite matrix with a length of about 96µm. The length of the austenite fingers or island-like austenite domains does not change on further cooling. Figure 68 shows that the position of the tip of the finger, shown with an arrow in Figure 67, remains constant with time. The δ to γ phase transformation goes to completion by the growth of dihedral morphologies and planar fronts.

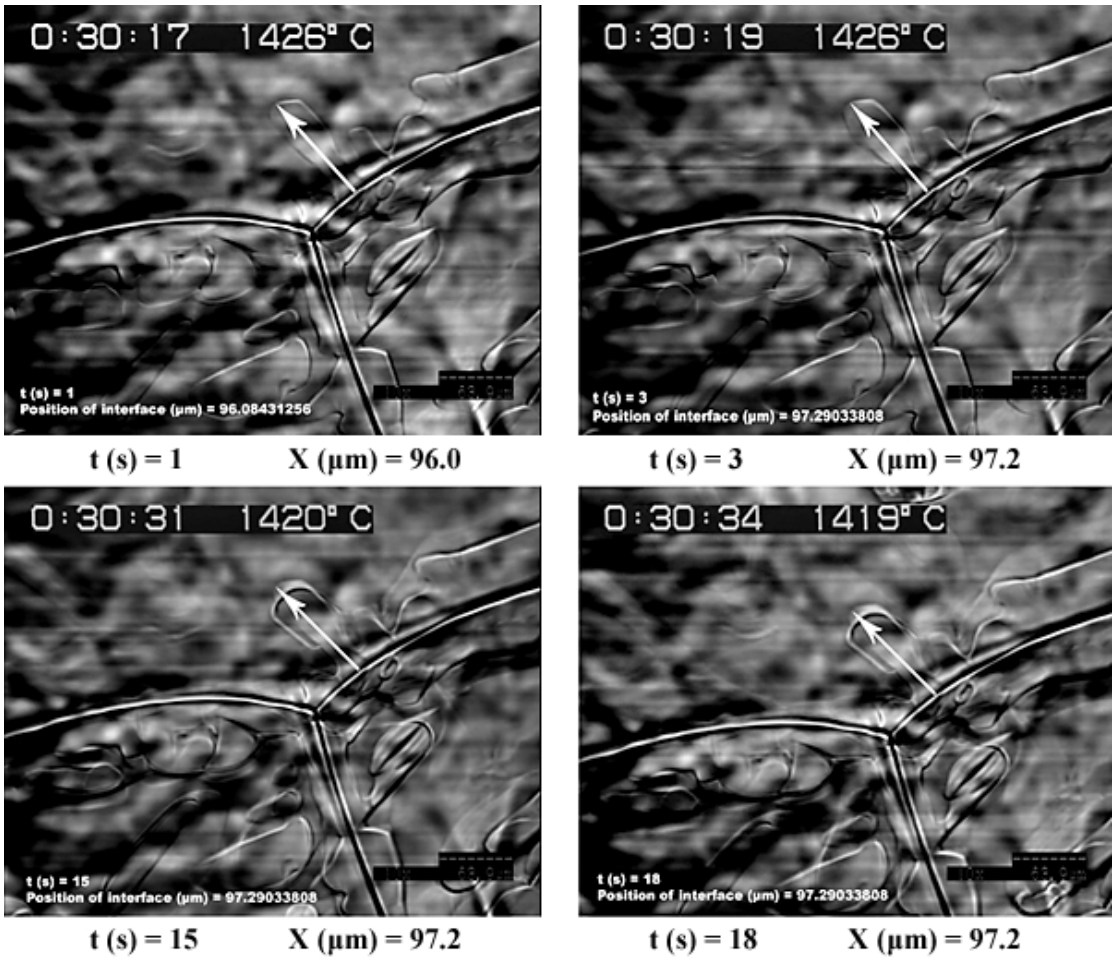

Figure 67 Formation and stabilization of austenite finger-like structures at the cooling rate of 30°C/min

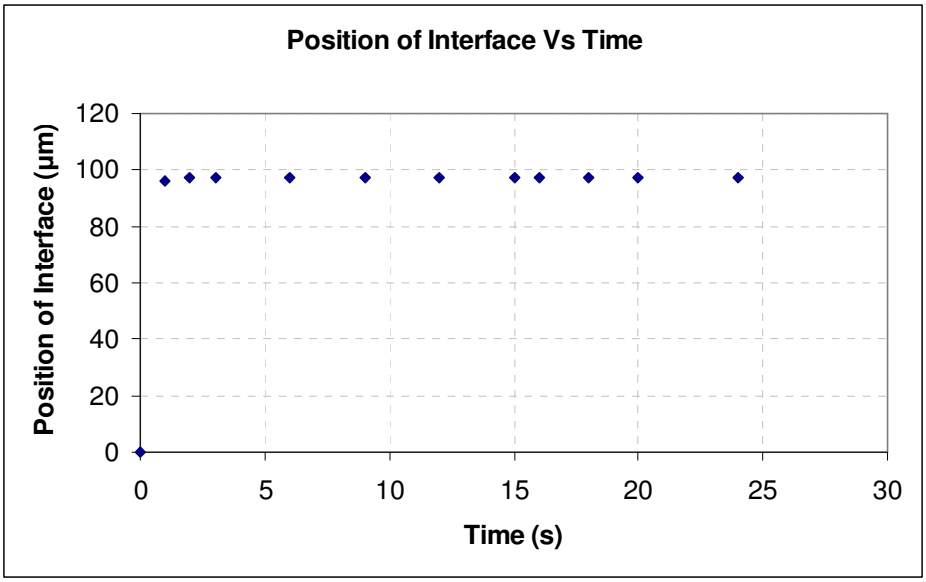

Figure 68 Stabilization of austenite finger-like structures at the cooling rate of 30°C/min

4.5 Group 1 - 40°C/min cooling rate

At a cooling rate of 40°C/min from the δ-ferrite phase field, finger-like austenite structures develop. Figure 69 shows an example of a delta-ferrite triple point which has moved just before initiation of the δ to γ phase transformation. Austenite forms at the delta-ferrite triple point and the associated grain boundaries and austenite fingers grow rapidly into the matrix. Dihedral austenite morphologies also form.

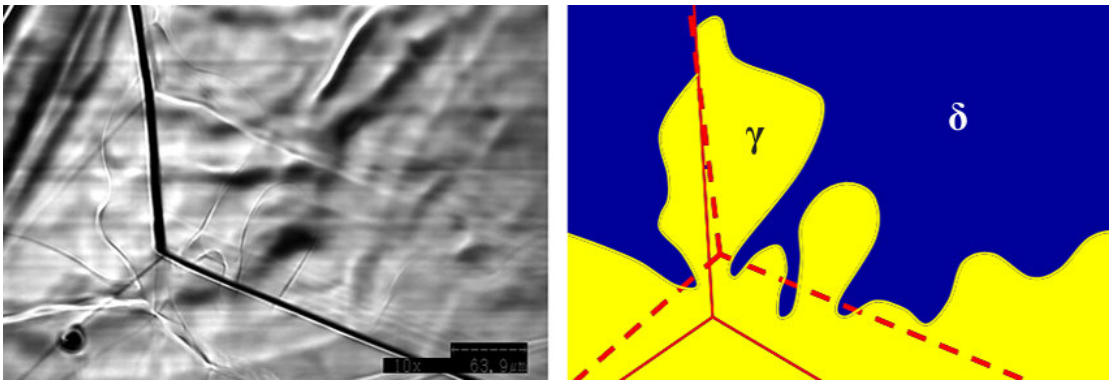

Figure 69 The delta-ferrite to austenite phase transformation morphology at a cooling rate of 40°C/min (dashed line shows the delta-ferrite grain boundary groove)

4.6 Group 1 - 70°C/min cooling rate

The current experimental arrangement in the high temperature microscope limits the cooling rate to 70°C/min. Figure 70 shows that at this cooling rate, the δ to γ transformation initiates at a δ-ferrite triple junction. This initial nucleation at the triple point is followed by further nucleation events along the grain boundaries. Within 2 seconds the whole sample is transformed through a "massive-type" of phase transformation (in the present context the terminology "massive-type" is used merely to distinguish this type of phase transition from the dihedral and planar growth morphologies observed at lower cooling rates).

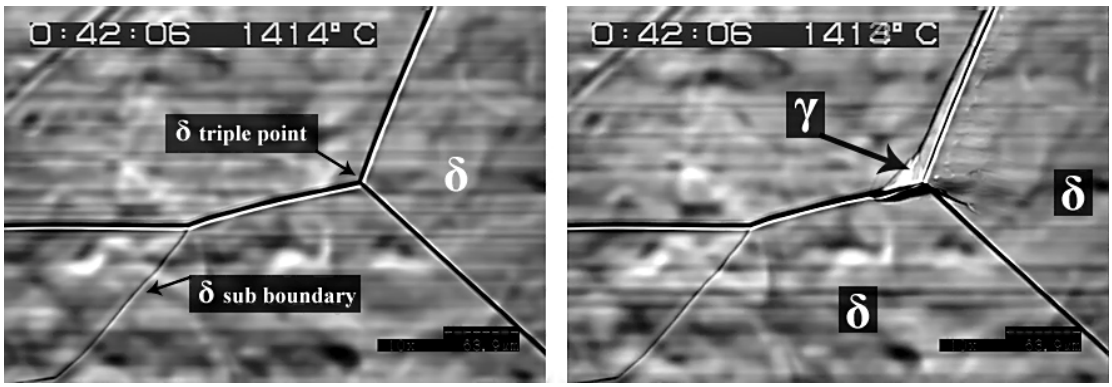

Figure 70 The nucleation of the delta-ferrite from the austenite triple junctions and GBs at a cooling rate of 70°C/min

Dihedral phase transformation morphologies are not present at this cooling rate and the finger-like structures are replaced by sword-like structures that propagate through the delta-ferrite matrix within a fraction of a second. Island-like morphologies such as observed at a cooling rate of 30°C/min are also present as shown in Figures 71-73.

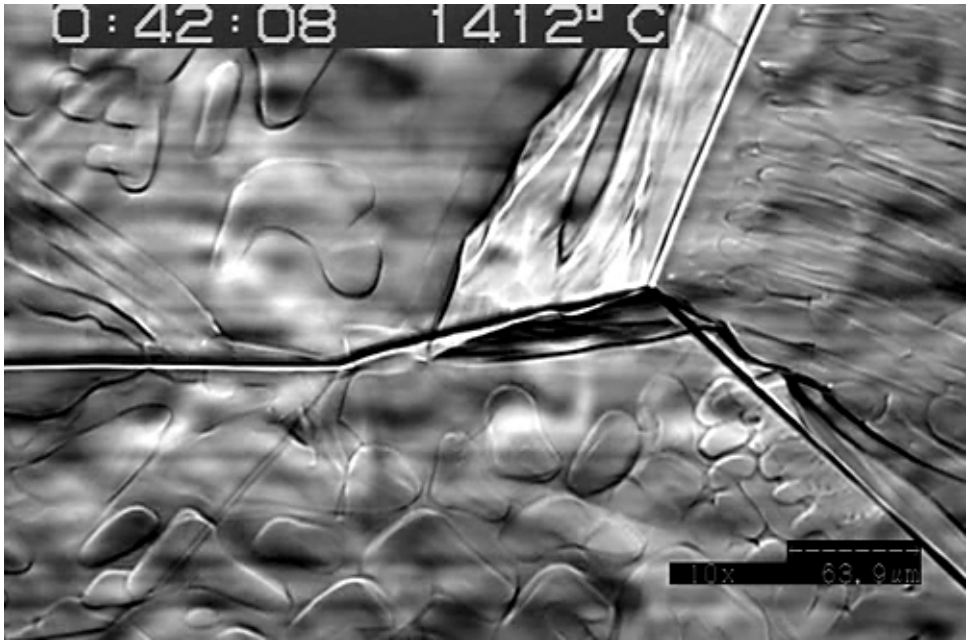

Figure 71 The delta-ferrite to austenite phase transformation morphology at a cooling rate of 70°C/min

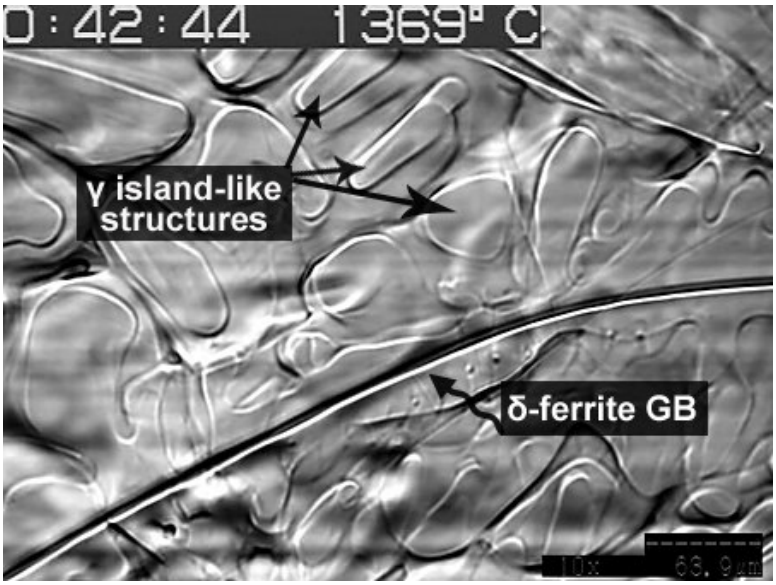

Figure 72 Another example of the formation of austenite island-like structures at a cooling rate of 70ºC/min

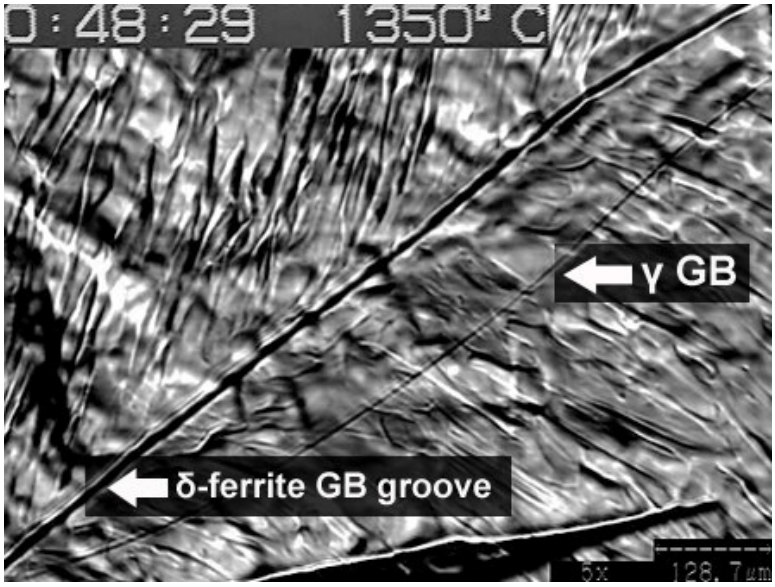

Figure 73 Formation of austenite sword-like structures at a cooling rate of 70°C/min

Following the completion of the δ/γ phase transformation, new austenite grain boundaries form and austenite grains grow as a function of time. The growth of certain and disappearance of other austenite grains continues during the grain growth phase until the austenite grain structure attains equilibrium, as shown in Figure 74.

It is interesting to note that a triple point of the newly-formed austenite structure can be observed relative to the position of the former δ-ferrite structure (delineated by the δ grooves formed by the prior δ-ferrite grain boundaries). It is also interesting to note that the austenite grain size appears to be very similar to that of the former δ-ferrite structure.

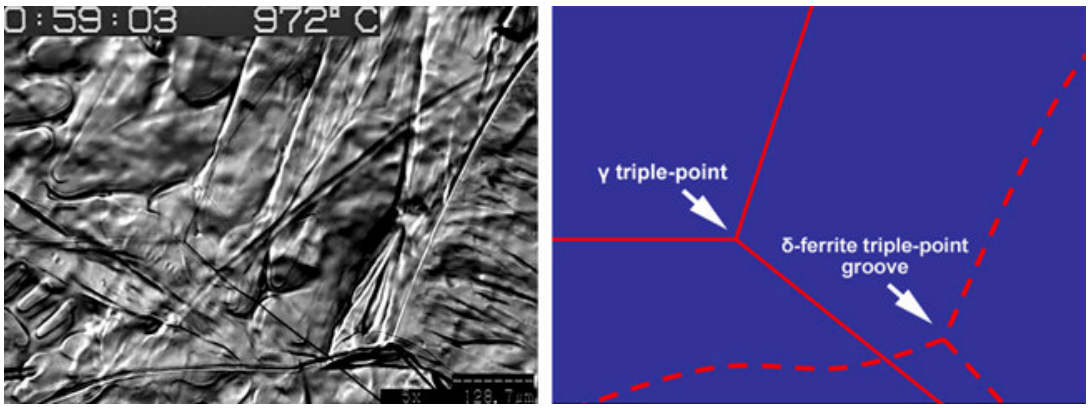

Figure 74 Austenite triple point at equilibrium following the δ/γ phase transformation

Upon further cooling of the austenite, alpha-ferrite nucleates at the austenite triple point, as shown in Figure 75a, followed by the growth of α-ferrite Widmanstätten plates into the austenite matrix as shown in Figure 75b.

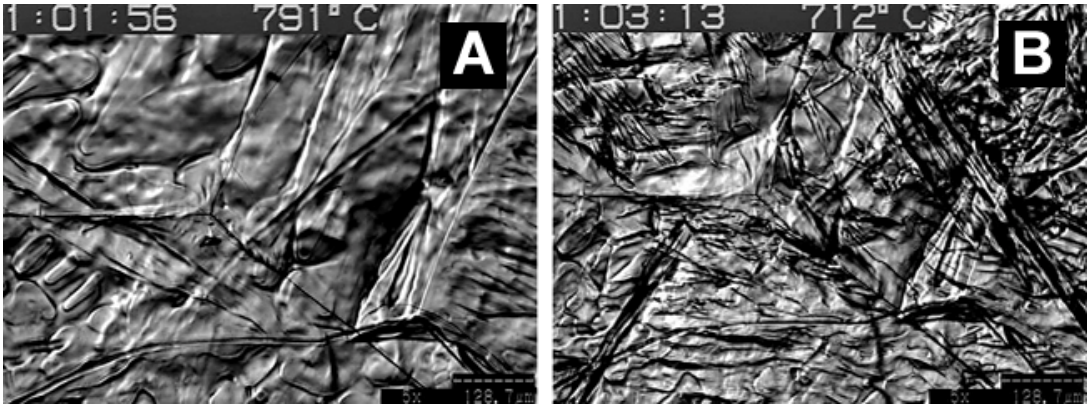

Figure 75 (a) Initiation of austenite to alpha-ferrite phase transformation (b) Typical structure of Widmanstätten colony

4.7 Group 2

Samples in Group 2 were 150μm thick as opposed to the 2mm thick specimens of Group 1. These experiments were conducted firstly in order to determine whether grain growth will be inhibited when the specimen thickness is of the same order or smaller than the grain size and secondly, whether the morphology of the phase transformation is a function of specimen thickness. However, both continuous and staggered grain boundary movements have been observed in the thin specimens, just as in the thick ones. Figure 76 depicts the continuous movement of a delta-ferrite triple point just before the start of the δ/γ phase transformation at a cooling rate of 15ºC/min. The time difference between the frames is about 2 seconds. Moreover, the morphology of the phase transformation seems to be the same in the thin and thick specimens and this observation leads to the conclusion that the surface observations on the surface of specimens in the high-temperature laser-scanning confocal-microscopy are a true representation of bulk behaviour.

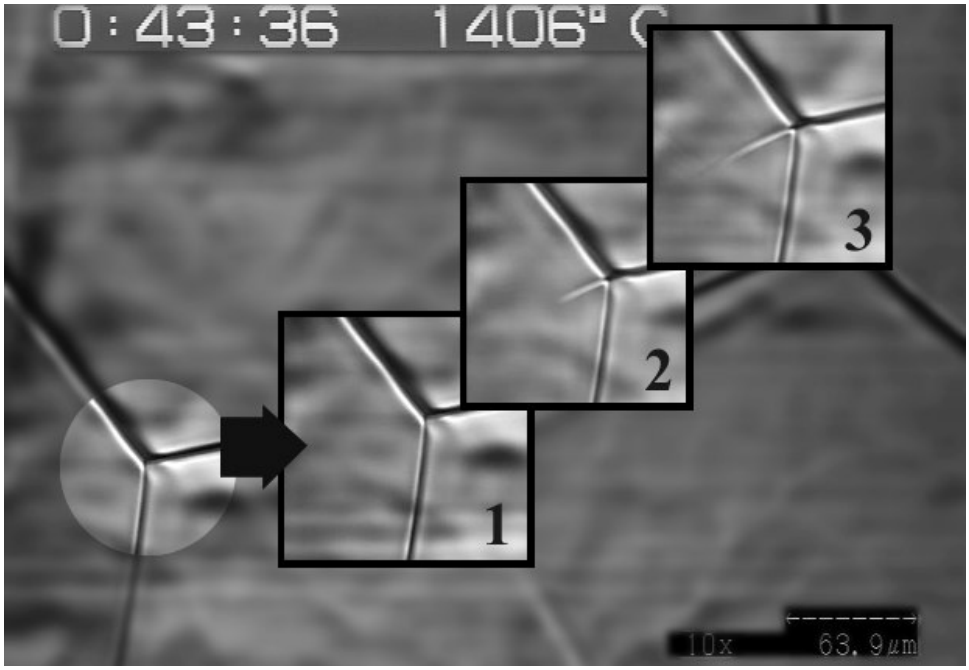

Figure 76 Continuous movements of delta-ferrite grain boundaries and triple point at the cooling rate of 15°C/min on thin sample

4.8 Preserving the delta-ferrite structure at room temperature

Although it is possible to observe delta-ferrite grains and grain boundaries at high temperature in the confocal microscope, it is more difficult to construct a map of the grain structure because of the limited field of view in the microscope. For this reason, an attempt has made to delineate delta-ferrite grain boundaries at room temperature. This was achieved by bleeding in a small amount of air into the specimen chamber of the microscope while the specimen was in the delta-ferrite region. The amount of oxygen was kept low enough just to form a thin oxide layer on the surface, preserving the grain boundaries of the delta-ferrite structure. The resulting microstructure of one such sample is shown in Figure 77 and it is evident that abnormal grain growth has occurred.

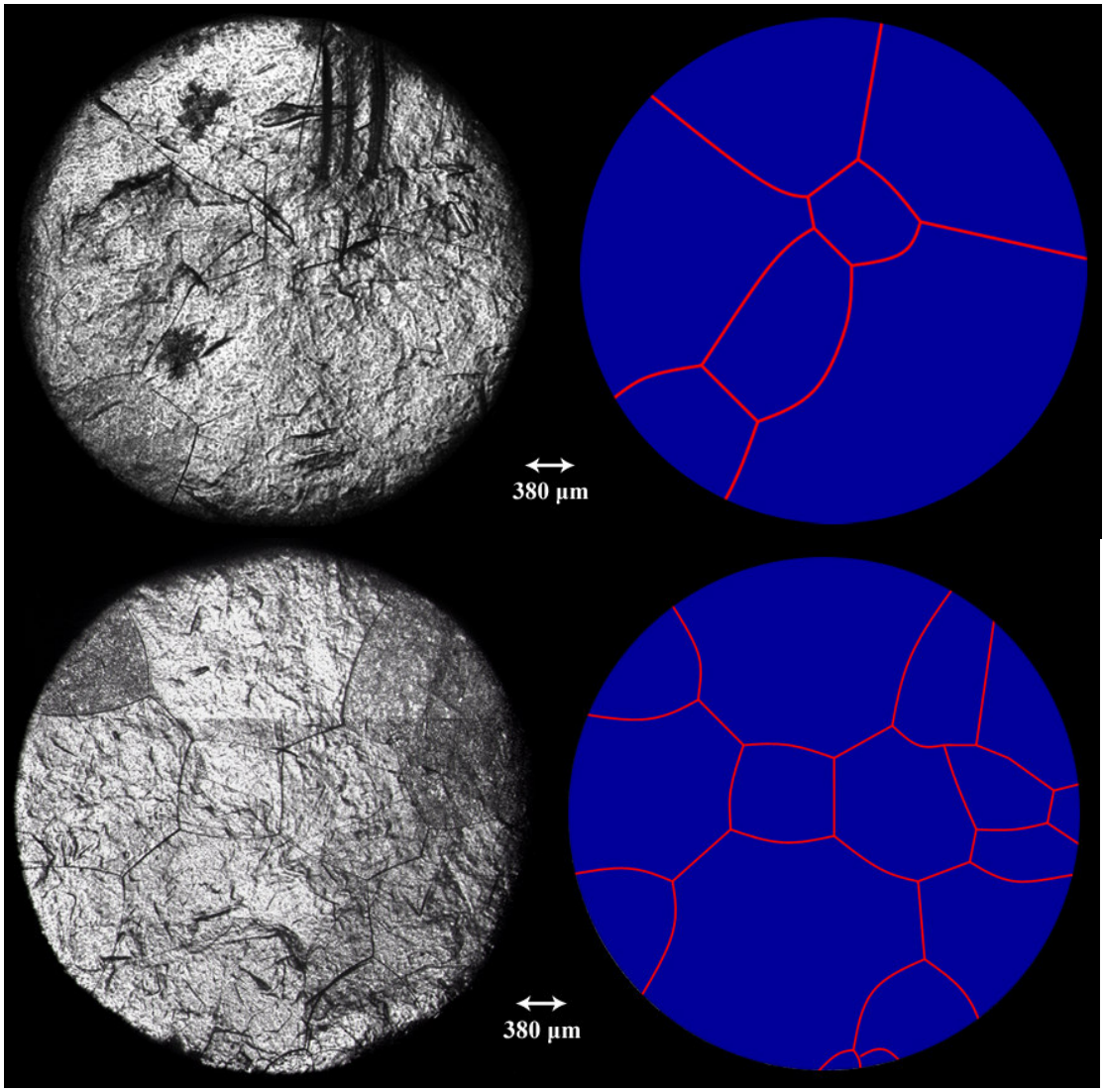

Figure 77 Preserved delta-ferrite structure in room temperature showing abnormal grain growth of some grains

Melfo [61] introduced air onto the surface of steel samples within the high-temperature microscope at temperature (in the austenite region). She suggests that when oxygen is introduced directly onto the surface of the steel surface, a relatively thick layer of iron oxide can form on the specimen surface before the grain boundaries are covered. Hence, a technique to delineate at room temperature, the positions of grain boundaries that exist at high-temperature is to introduce a small amount of air so that the surface is oxidized but the grain boundaries remain delineated. This technique was used to prepare the specimens as shown schematically in Figure 78.

Please see print copy for figure 78

Figure 78 Schematic illustration of oxide formation during the progressive or direct air insertion [61]

4.9 Grain growth observations

Figure 79 shows a hexagonal delta-ferrite grain observe in a thin sample and pictured at a temperature of 1446ºC. Making the assumption of a circular shape, the grain exhibits a diameter of about 800µm.

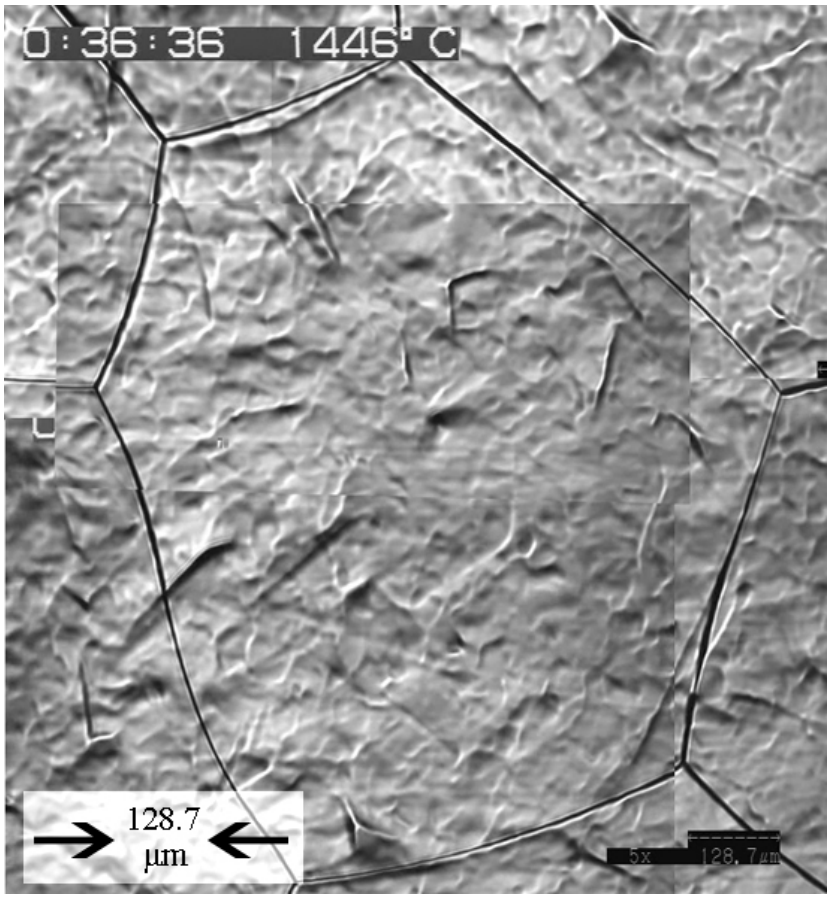

Figure 79 A delta-ferrite grain with a diameter of about 800µm (assuming a circular morphology)

After the transformation to the austenite at a cooling rate of 15ºC/min, the austenite grains are approximately 500µm in diameter, as shown in Figure 80. This relationship between the size of the delta-ferrite and austenite grains has been observed in many instances and suggests austenite grain size is in large measure determined by the grain size of the prior delta-ferrite grains. This is a significant finding because it means that the abnormally-large austenite grains often observed along the oscillation marks in a continuously cast steel slab and which leads to transverse surface cracks during the straightening operation, may well result from very large delta-ferrite grains.

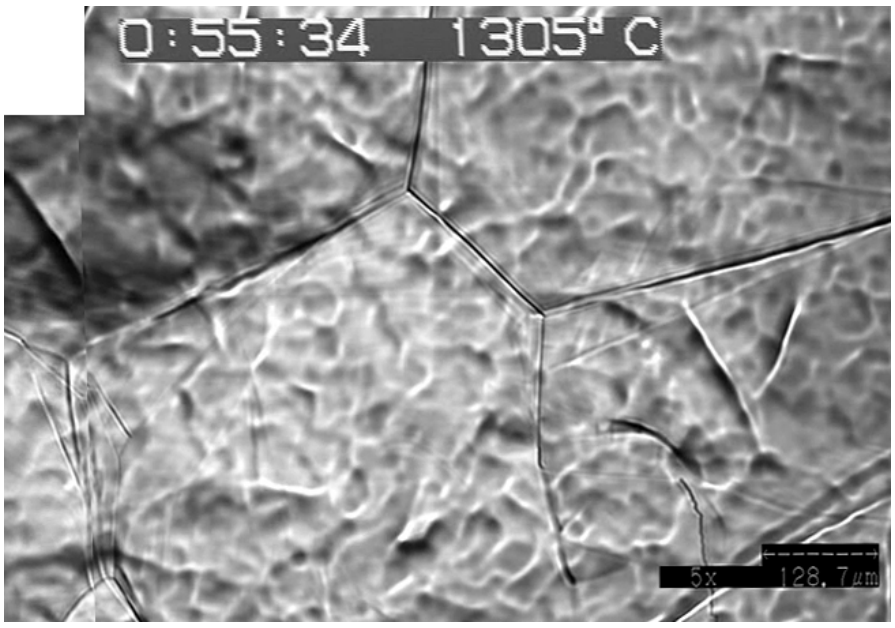

Figure 80 an austenite grain with a diameter of about 500µm (assuming a circular morphology)

In order to prove beyond reasonable doubt that the observed boundaries in the austenite are actually austenite grain boundaries (and not the grooves of the delta-ferrite), samples were cooled to the temperatures of around 700ºC so that the austenite transforms to ferrite. Figure 81 shows clearly that during the austenite to ferrite phase transformation, Widmanstätten plates nucleate on austenite grain boundaries, proving that the boundaries are austenite grain boundaries indeed.

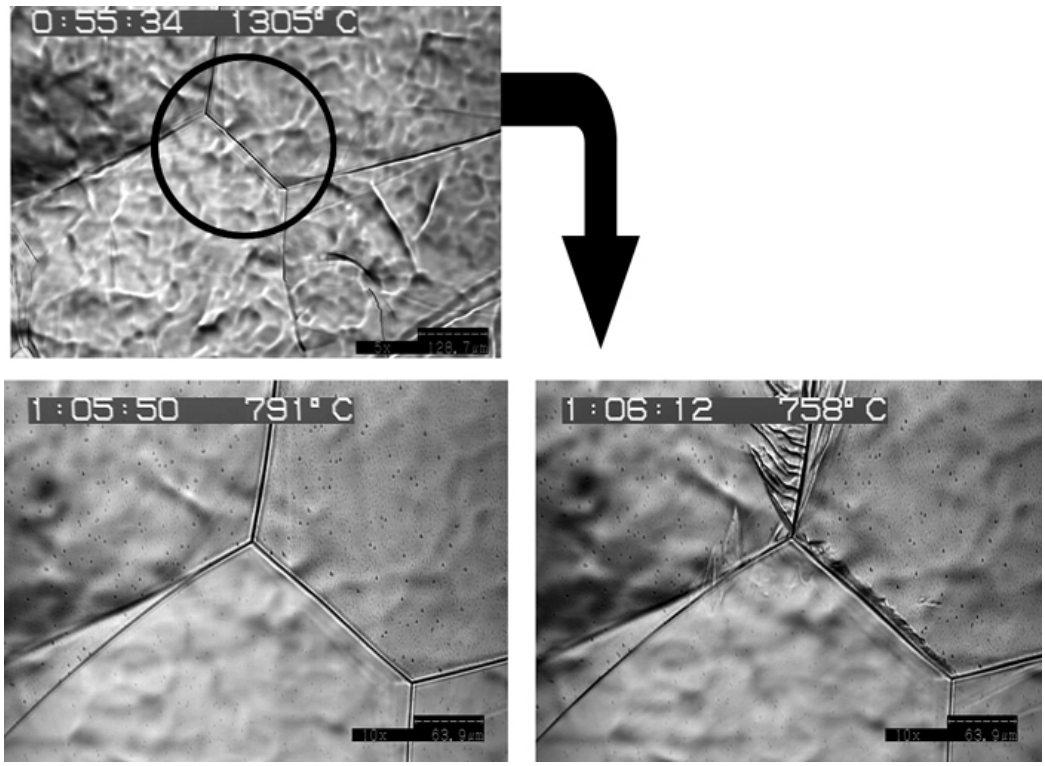

Figure 81 Formation of Widmanstätten plates at the austenite grain boundaries

The same sequence of events was repeated for the thicker (Group 1) samples. Although the initial delta-ferrite grains in the thick samples are bigger than in the thin samples (as expected and discussed in the literature), large delta-ferrite grains resulted in large austenite grains, just as in the thin samples. Figure 82 shows austenite grains as well as a delta-ferrite grain boundary groove and it is clear that the relationship between delta-ferrite and austenite grain size can be easily established.

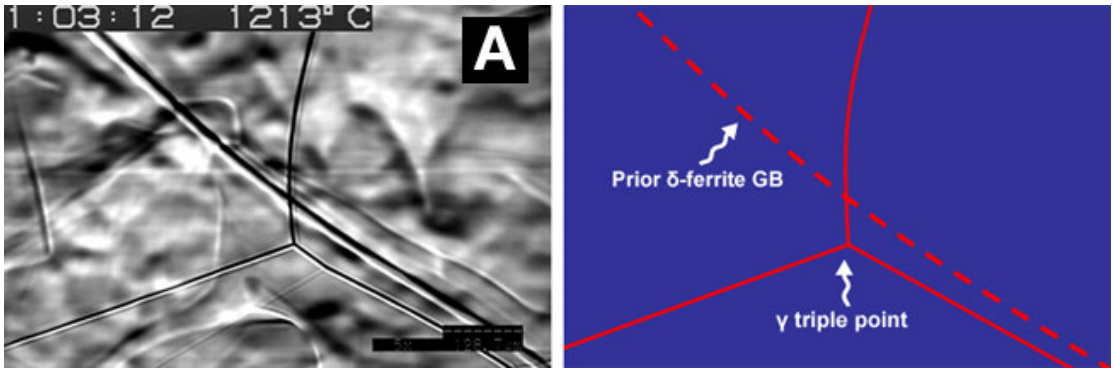

Figure 82 Austenite structure and grooves of the prior δ-ferrite showing an approximately same grain size (repeated)

At a cooling rate of 70ºC/min, delta-ferrite transformed to austenite in a massive-type fashion and it was of interest to establish whether the growth of austenitic grains

would be different in this structure compared to the morphologies obtained at lower cooling rates. Figure 83 shows that notwithstanding the fact that austenite formed through a massive type of phase transformation, when austenite grains grow, they form the same kind of network, related in size to the original delta-ferrite grains, as observed in specimens that were cooled at lower cooling rates.

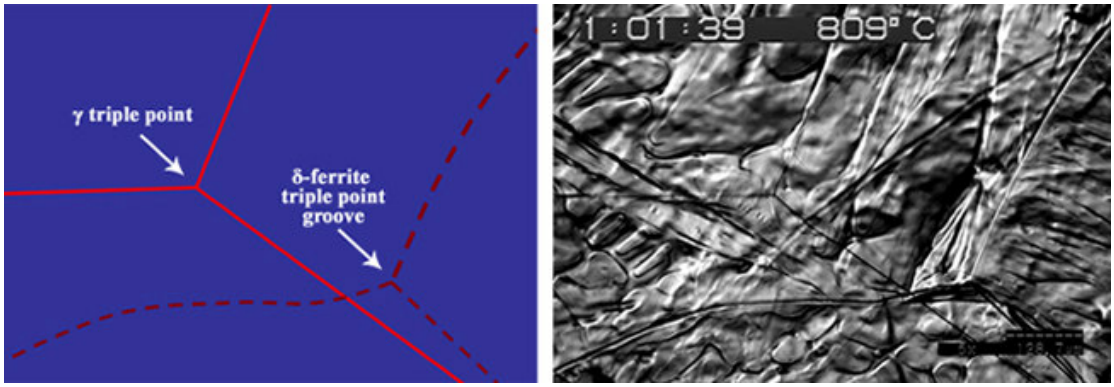

Figure 83 Austenite grain boundaries as well as the prior delta-ferrite grain boundaries, observed at the cooling rate of 70ºC, showing no significant change in the size of grains after the δ/γ phase transformation (repeated)

Chapter 5- Conclusions

Delta-ferrite grain boundaries change their location by three different mechanisms: staggered motion, consistent continuous motion and rapid motion.

Staggered motion is encountered when grain boundaries are pinned on the surface. This pinning effect is due to the positioning of the controlling boundary (the grain boundary beneath the triple point) relative to the critical angle formed between the vertical and the normal to the notch surface.

Consistent continuous motion results when there is a significant difference in the surface energy of adjacent grains.

Rapid motion occurs when an austenite grain nucleates at the bottom surface of the thin specimen, and grows along the grain boundary connected to the triple point. As the growing austenite grain approaches the triple point on the surface, the grain boundary energy balance is disturbed and the triple point moves rapidly to re-adjust this energy balance.

The progression of the δ/γ inter-phase interface displays distinct behaviour under different experimental conditions:

- The growth of austenite can be arrested at low cooling rates
- At medium cooling rates, the newly formed austenite grains can grow relatively fast by the progression of planar interfaces
- At high cooling rates, a massive type of phase transformation morphology is encountered.

Regardless of the transformation morphology, the newly formed austenite structure develops a grain boundary structure approaching an equilibrium configuration

When δ-ferrite is cooled from 1723°K at a rate of 10 °C/min or less, austenite nucleates at δ-ferrite triple points and propagates with a dihedral morphology.

At a cooling rate of 15 °C/min the morphology changes to a combination of dihedral and finger-like structures.

At a cooling rate of 30 °C/min, island-like morphologies form but finger-like morphologies are still present.

At a cooling rate of 70°C/min, δ-ferrite transforms to austenite by a massive kind of phase transformation, characterized by a combination of sword-like and island-like structures.

The morphology of the delta-ferrite to austenite phase transformation is not altered by using very thin samples of such dimensions that the thickness is of the same order as the grain size.

The in-situ observations in the high-temperature microscope are a true representation of bulk behaviour.

Grain boundaries of the delta-ferrite structure can be preserved at room temperature by introducing a controlled amount of oxygen into the microscope chamber while the specimen is in the delta-ferrite phase field. This technique can be used to confirm the observations made in-situ in the high-temperature microscope

Although the initial delta-ferrite grains in the thick samples are bigger than those in the thin samples, The relative change in the grain size during the δ/γ is neglectable.

Convincing experimental evidence was found that the grain size of austenite resulting from the delta-ferrite to austenite phase transition is determined by the delta-ferrite grain size.

Phase-field modelling provides a good simulation of the experimentally observed morphology and growth of the newly formed austenite phase as it precipitates in and grows from delta-ferrite.

Appendix 1

Vogel [62], Bragg [29] and Harker *et al.* [63] have pointed out that the boundaries between undistorted grains should behave as if they had a surface tension. In the solid state the grain boundary are without any voids, which follows $r_1 = r_2$ and therefore:

$$\left(\frac{1}{r_1} - \frac{1}{r_2}\right) = 2\left(\frac{1}{r_1}\right)$$

When grain boundaries melt r_1 and r_2 are not necessarily equal. They may even have the same sign, Figure 84.

Please see print copy for figure 84

Figure 84 The radii of curvature (r_1 and r_2) of the grains between which the atoms are transferred [37]

Therefore $\left(\frac{1}{r_1} - \frac{1}{r_2}\right) << \left(\frac{1}{r_1}\right)$ which leads to a much smaller driving force in liquid state compared to the solid state.

Further research by Burke and Turnbull concluded that the driving force for the grain growth after recrystallization is to decrease the grain boundary energy and not to decrease the residual strain within grains. Burke and Turnbull then analysed the kinetics of grain growth. They derived a general expression for G and compared the computed values with experimental measurements. If the surface energy of the boundary were the driving force, then the rate of the grain boundary migration can be expressed by: [37]

$$G = e(kT/h)\lambda(K\sigma V/rRT)\exp[\Delta S_A/R]\exp[-Q_G/RT]$$

R: Boundary radius of curvature *V: gram atomic volume of the metal*

K and k: Constants *T: Temperature*

σ: Surface energy of the boundary *R: Gas constant*

Q_G: Activation energy for boundary migration

ΔS_A: Difference in entropy between the atom in its activated state and in site B

If the condition is isothermal, then the equation above can be simplified as:

$$G = K'\sigma V / r$$

The rate constant K' is dependent on temperature according to the relationship:

$$K' = K'_0 \exp(-\frac{Q_G}{RT})$$

In the equation above, K'_0 is a constant.

Appendix 2

Second phase particles and grain boundary pinning

Miodownik [64] argues that the presence of the second phase particles control nucleation rate and grain growth and grain boundary sliding in metal alloys and ceramics. Figure 85 shows the interaction of a grain boundary with a radius of curvature, ρ, with a spherical particle of radius.

Please see print copy for figure 85

Figure 85 A schematic of the formation of a dimple during grain boundary bypass of a particle [64]

Three surface tensions: the boundary surface tension, γ, and the two particle/boundary surface tensions, γ_{AP} and γ_{BP} are evident in Figure 73. These surface tensions dictate the equilibrium shape of the boundary near the particle, which is a catenoid of revolution often called a dimple. Based on the Figure 73 the pinning force can be calculated by the expression below:

$$F = 2\pi r y \sin\theta \cos(\pi/2 - \alpha + \theta)$$

θ is the bypass angle and $\gamma_{AP} - \gamma_{BP} = \gamma \cos\alpha$. When a large number of pinning particles interact with a grain boundary, then the pinning stress on the boundary is a sum of the forces exerted by each particle and so depends on the position of each particle relative to the boundary**.**

Appendix 3

MICRESS simulation of carbon concentration gradient and its evolution during the δ-ferrite/γ phase transformation at the cooling rate of 5°C/min

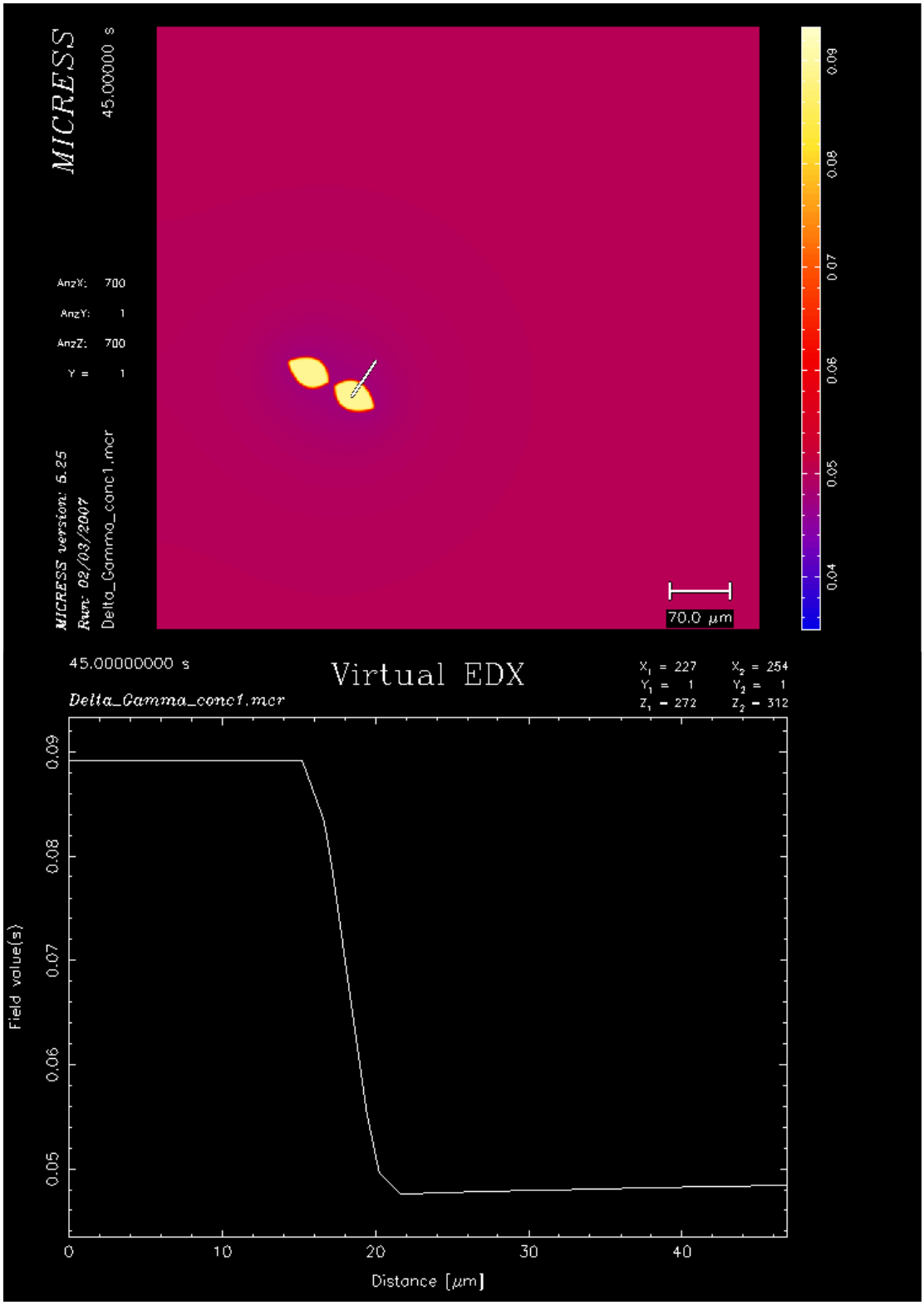

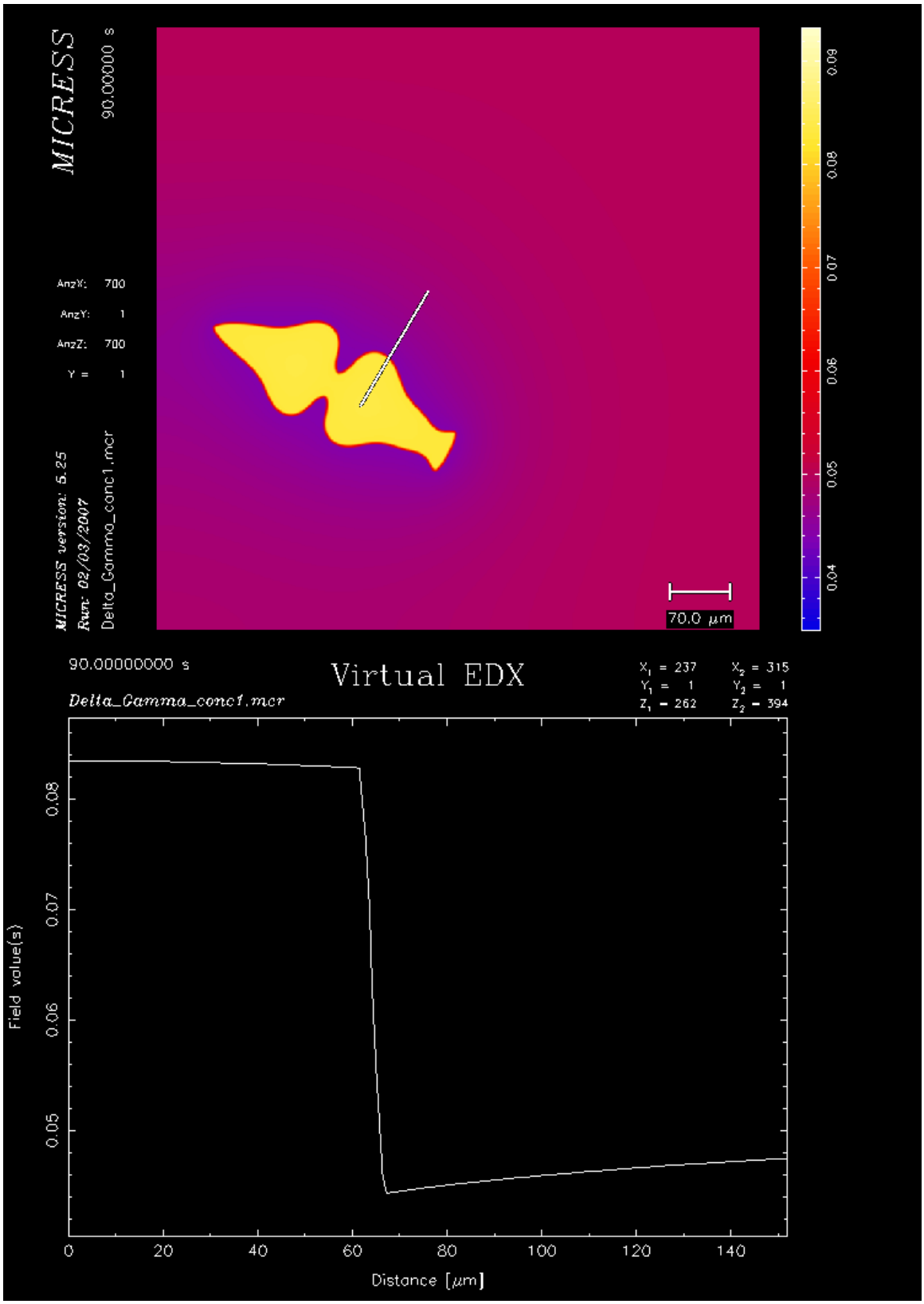
MICRESS
90.000000 s
AnzX: 700
AnzY: 1
AnzZ: 700
Y = 1
MICRESS version: 5.25
Run: 02/03/2007
Delta_Gamma_conc1.mcr
70.0 µm
0.09
0.08
0.07
0.06
0.05
0.04
90.00000000 s
Virtual EDX
Delta_Gamma_conc1.mcr
X1 = 237
Y1 = 1
Z1 = 262
X2 = 315
Y2 = 1
Z2 = 394
Field value(s)
0.08
0.07
0.06
0.05
0
20
40
60
80
100
120
140
Distance [µm]

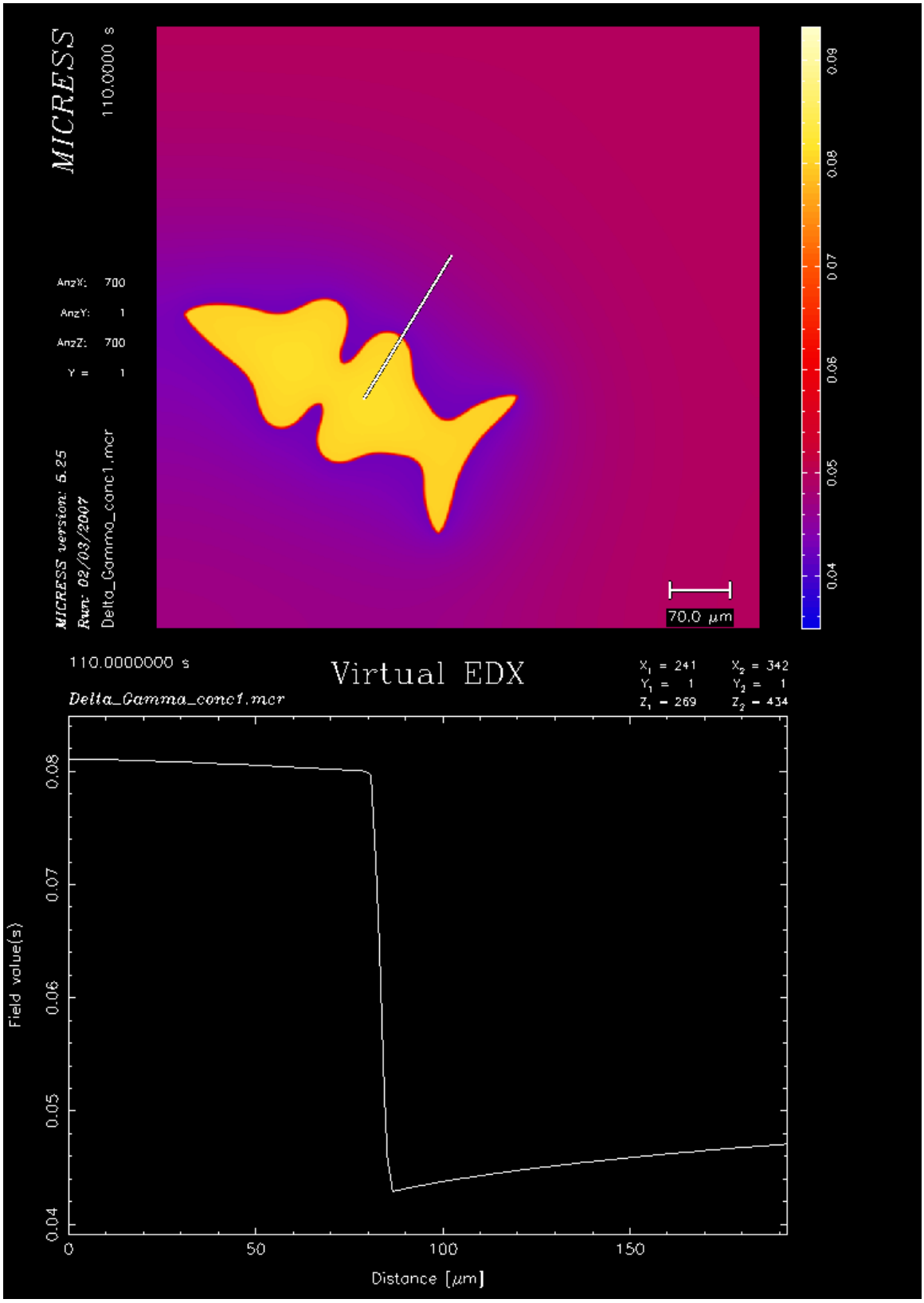
MICRESS
110.0000 s
AnzX: 700
AnzY: 1
AnzZ: 700
Y = 1
MICRESS version: 5.25
Run: 02/03/2007
Delta_Gamma_conc1.mcr
70.0 µm
0.09
0.08
0.07
0.06
0.05
0.04
110.0000000 s
Virtual EDX
Delta_Gamma_conc1.mcr
X1 = 241
Y1 = 1
Z1 = 269
X2 = 342
Y2 = 1
Z2 = 434
Field value(s)
0.08
0.07
0.06
0.05
0.04
0
50
100
150
Distance [µm]

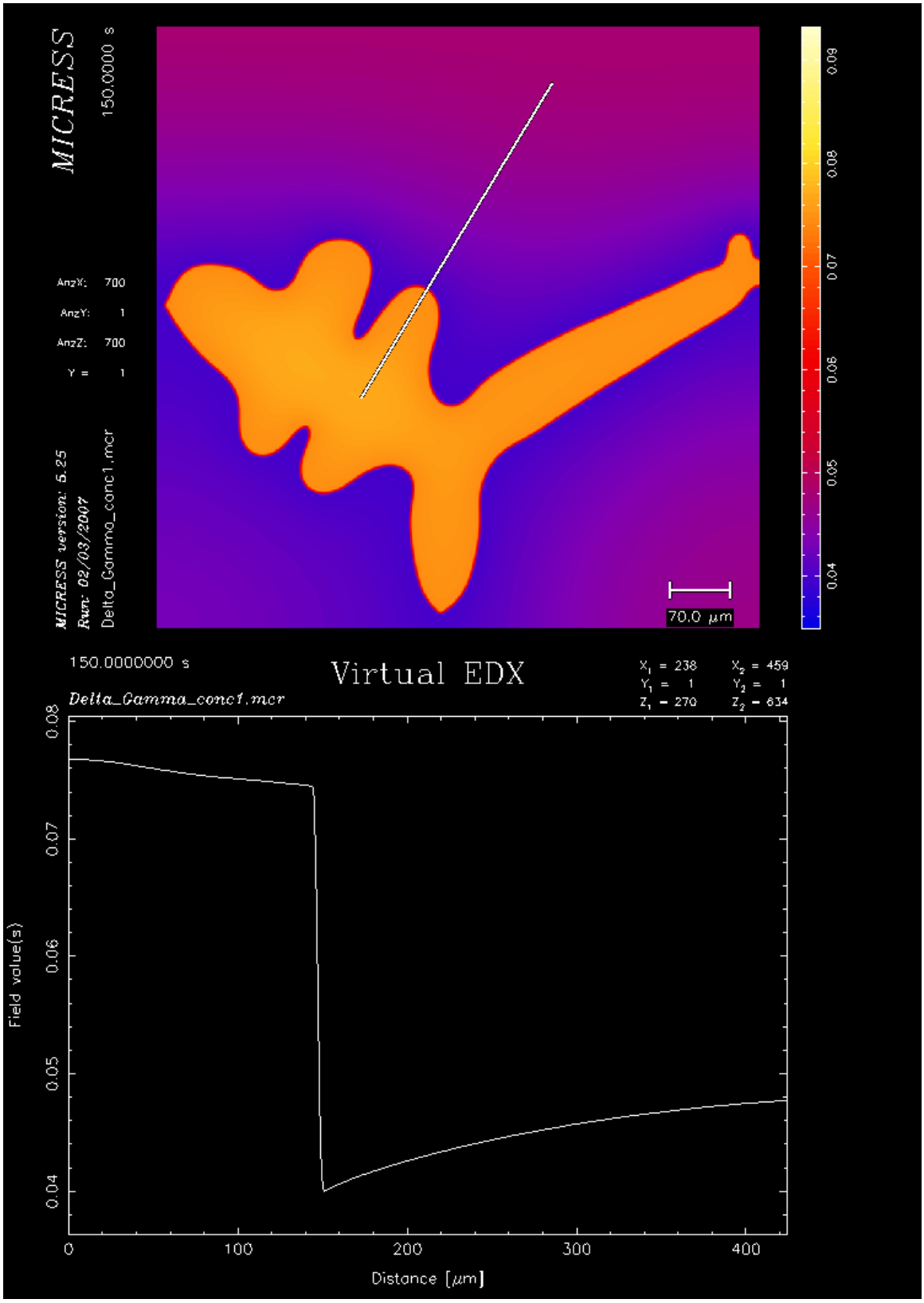
MICRESS
150.0000 s
AnzX: 700
AnzY: 1
AnzZ: 700
Y = 1
MICRESS version: 5.25
Run: 02/03/2007
Delta_Gamma_conc1.mcr
70.0 µm
0.09
0.08
0.07
0.06
0.05
0.04
150.0000000 s
Virtual EDX
Delta_Gamma_conc1.mcr
X1 = 238
Y1 = 1
Z1 = 270
X2 = 459
Y2 = 1
Z2 = 634
Field value(s)
Distance [µm]
0
100
200
300
400

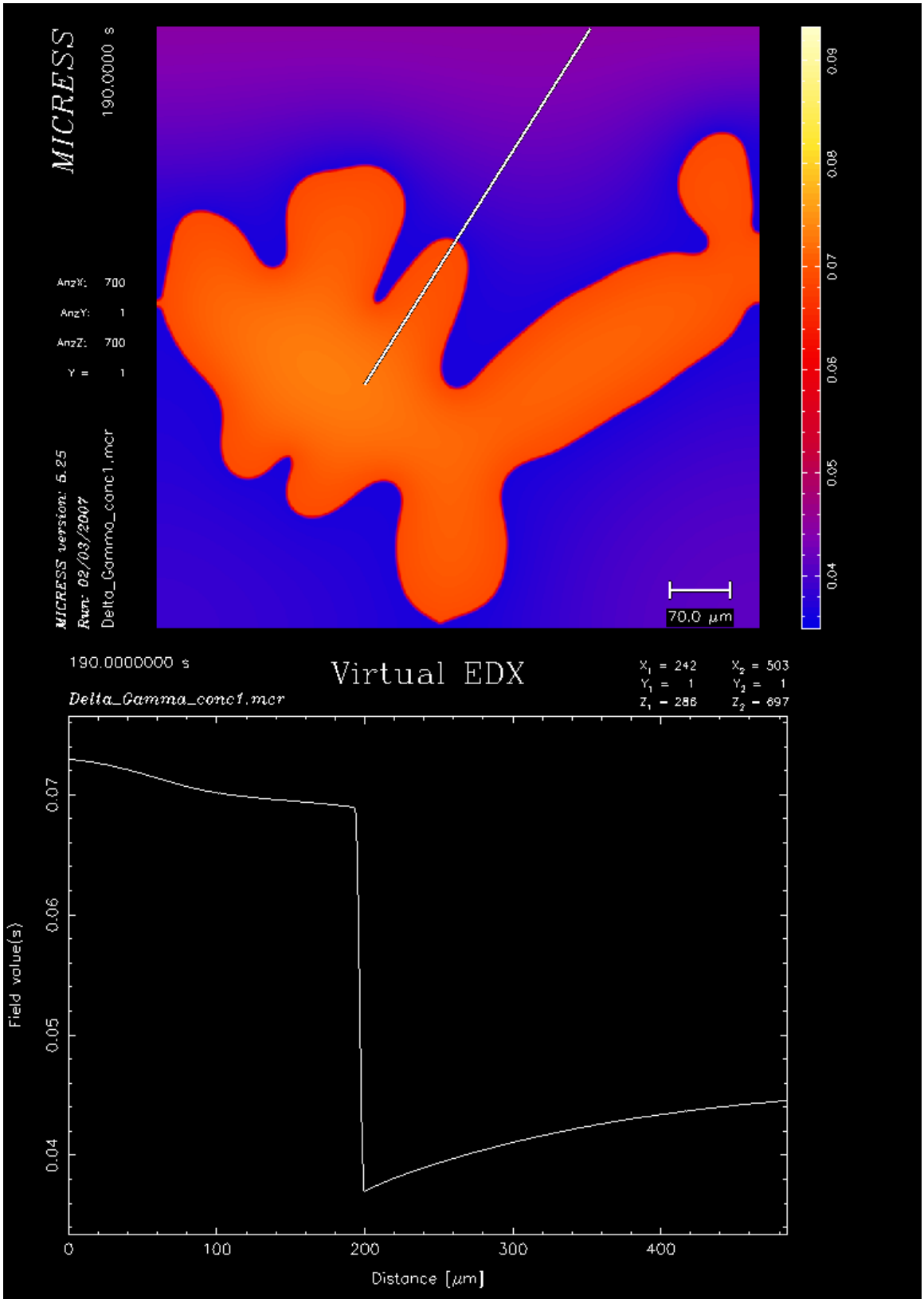
MICRESS
190.0000 s
AnzX: 700
AnzY: 1
AnzZ: 700
Y = 1
MICRESS version: 5.25
Run: 02/03/2007
Delta_Gamma_conc1.mcr
70.0 µm
0.09
0.08
0.07
0.06
0.05
0.04
190.0000000 s
Virtual EDX
Delta_Gamma_conc1.mcr
X1 = 242
Y1 = 1
Z1 = 288
X2 = 503
Y2 = 1
Z2 = 697
Field value(s)
0.07
0.06
0.05
0.04
0
100
200
300
400
Distance [µm]

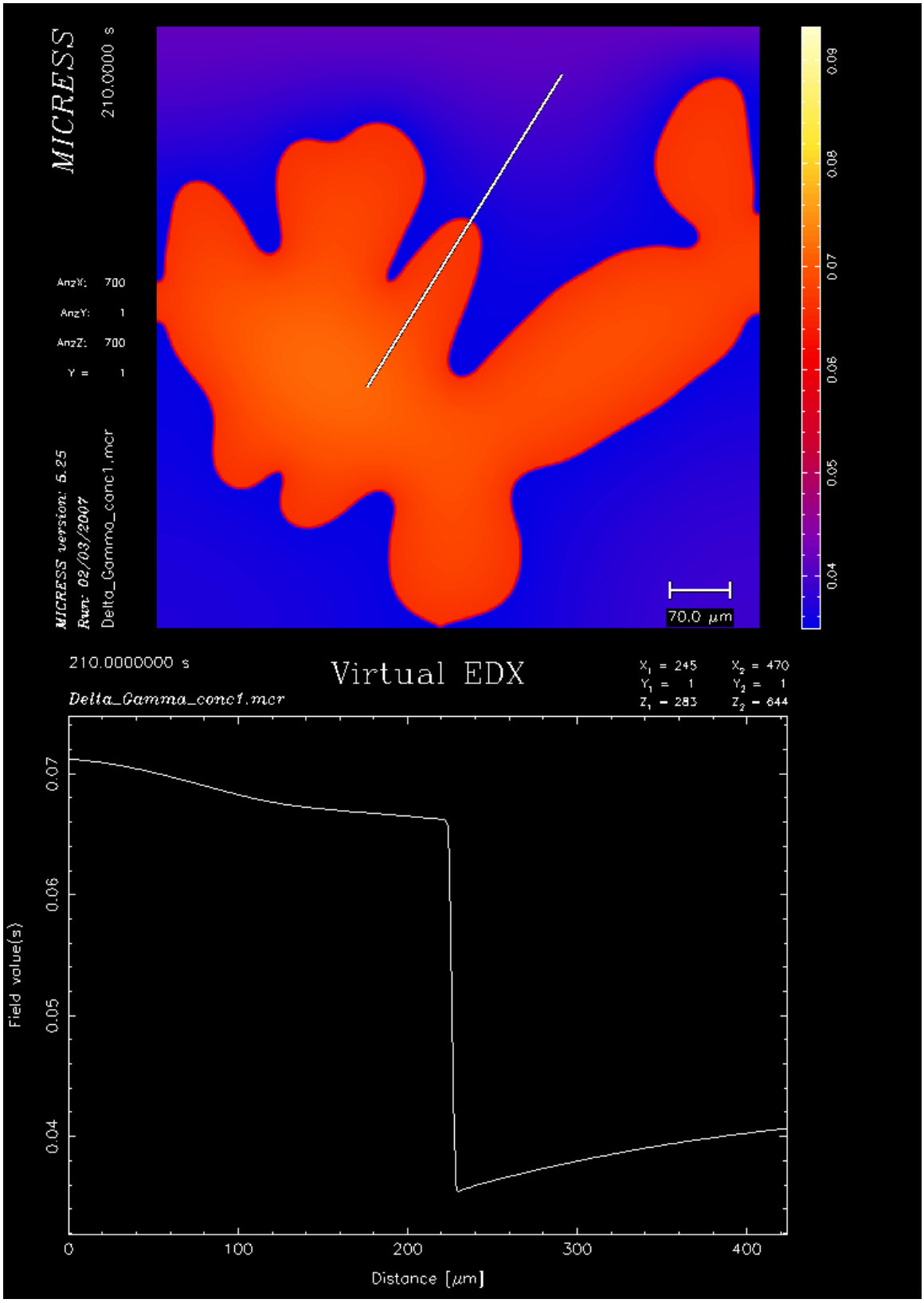
MICRESS
210.0000 s
AnzX: 700
AnzY: 1
AnzZ: 700
Y = 1
MICRESS version: 5.25
Run: 02/03/2007
Delta_Gamma_conc1.mcr
70.0 µm
0.09
0.08
0.07
0.06
0.05
0.04
210.0000000 s
Virtual EDX
Delta_Gamma_conc1.mcr
X1 = 245 X2 = 470
Y1 = 1 Y2 = 1
Z1 = 283 Z2 = 644
Field value(s)
0.07
0.06
0.05
0.04
0
100
200
300
400
Distance [µm]

References

1. Baumann, H.G., G. Holleis, K. Schwaha, and M.M. Wolf. Metallurgy of Iron (Berlin, 1992).
2. Wolf, M.M. Future of Iron and Steelmaking. 12, 214a-232a 161b-194b (1992).
3. Wolf, M.M. History of continuous casting. Steelmaking Conference Proceedings 75, Iron & Steel Society, Warrendale, PA, 83-137 (1992).
4. Phelan, D.J. In-situ studies of phase transformations in iron alloys (School of Materials Engineering, University of Wollongong, Wollongong, 2002).
5. Wolf, M.M. Initial solidification and strand surface quality of peritectic steels. 9, Continuous casting. ISS/AIME, Warrendale, PA, 211 (1997).
6. http://www.me.iitb.ac.in/~bravi/ME333/L06.pdf.
7. http://www.steel-trp.org/Briefing05Pres/03-TRP9943_CMU_oscillation.pdf.
8. Mukunthan, K., L. Strezov, R. Mahapatra, and W. Blejde. Evolution of microstructures and product opportunities in low carbon steel strip casting. Brimacombe Memorial Symposium, Vancouver, BC, Canada, Oct. 1-4, 2000, Canadian Institute of Mining, Metallurgy and Petroleum, 421-437 (2000).
9. Tsai, H.T., H. Yin, M. Morales, and S. Morales. Journal, AISTech, Charlotte, NC, (2005)
10. Dippenaar, R., S.-C. Moon, and E.S. Szekeres. Strand Surface Cracks -The Role of Abnormally-Large Prior-Austenite Grains. Journal, AISTech, Cleveland OH, 833-843, (2006)
11. Szekeres, E.S. A review of strand casting factors affecting transverse cracking. Journal, Pres'n, Proceedings of the Sixth International Conference on Clean Steel, Balatonfüred, Hungary, 324–338, (2002)
12. Badri, A., T.T. Natarajan, C.C. Snyder, K.D. Powers, F.J. Mannion, M. Byrne, and A.W. Cramb. A mold simulator for continuous casting of steel: Part II. The formation of oscillation marks during the continuous casting of low carbon steel. Metallurgical and Materials Transactions B: Process Metallurgy and Materials Processing Science 36B, 373-383 (2005).
13. Takeuchi, E. and J.K. Brimacombe. The formation of oscillation marks in the continuous casting of steel slabs. Metallurgical Transactions B: Process Metallurgy 15B, 493-509 (1984).
14. Thomas, B.G., D. Lui, and B. Ho. Effect of transverse depressions and oscillation marks on heat transfer in the continuous casting mold. Sensors and Modeling in Materials Processing: Techniques and Applications, Proceedings of a Symposium on the Application of Sensors and Modeling to Materials Processing, Orlando, Fla., Feb. 9-13, 1997, The Minerals, Metals, & Materials Society, 117-142 (1997).
15. Emling, W.H. and S. Dawson. Mold instrumentation for breakout detection and control. Steelmaking Conference Proceedings 74, 197-217 (1991).
16. Sato, R. Powder fluxes for ingot making and continuous casting. Proceedings - National Open Hearth and Basic Oxygen Steel Conference 62, 48-67 (1979).
17. Matsushita, A., K. Isogami, M. Temma, T. Ninomiya, and K. Tsutsumi. Trans. Iron Steel Inst. Jpn. 28, 531-34 (1988).
18. Tomono, H., P. Ackermann, W. Kurz, and W. Heinemann. Solidification Technology in the Foundry and Cast House (Metals Society, 1983).
19. Jimbo, I. and A.W. Cramb. Trans. Iron Steel Soc. 14, 55-64 (1993).

20. Laki, R.S., J. Beech, and G.J. Davies. Curved-boundary heat-transfer model and its application to meniscus zone during casting. Ironmaking and Steelmaking 11, 283-91 (1984).
21. Saucedo, I.G. Initial Solidification and Strand Surface Quality of Peritectic Steels. Journal, ISS-AIME, Continious Casting, Warrendale, PA, 131-41, (1997)
22. Savage, J. and W.H. Pritchard. Iron Steel Inst. 178, 269-277 (1954).
23. Nakato, H., T. Nozaki, Y. Habu, H. Oka, T. Ueda, Y. Kitano, and T. Koshikawa. Improvement of surface quality of continuously cast slabs by high frequency mold oscillation. Steelmaking Conference Proceedings 68th, 361-5 (1985).
24. Wolf, M.M. Mold oscillation guidelines. Steelmaking Conference Proceedings 74, 51-71 (1991).
25. Nakamori, Y., Y. Fujikake, K. Tokiwa, T. Kataoka, S. Tsuneoka, and H. Misumi. Journal Of The Iron And Steel Institute Of Japan (Tetsu-to-Hagané) 70, 1262-68 (1984).
26. Wray, P.J. Metall. Trans. B. 12B, 167-76 (1981).
27. Singh, S.N. and K.E. Blazek. J. Met. 26, 17-27 (1974).
28. Thomas, B.G. and H. Zhu. Thermal Distortion of Solidifying Shell Near Meniscus in Continuous Casting of Steel. Journal, Solidification Science and Processing Conference, Honolulu, 197–208, (1996)
29. Bragg, W.L. Proc. Phys. Soc. 52, 105 (1940).
30. Szekeres, E.S. Overview of mold oscillation in continuous casting. Iron and Steel Engineer 73, 29-37 (1996).
31. Schwerdtfeger, K. and H. Sha. Depth of oscillation marks forming in continuous casting of steel. Metallurgical and Materials Transactions B: Process Metallurgy and Materials Processing Science 31B, 813-826 (2000).
32. Yin, H., T. Emi, and H. Shibata. Morphological instability of d-ferrite/g-austenite interphase boundary in low carbon steels. Acta Materialia 47, 1523-1535 (1999).
33. Dippenaar, R. On the interrelationship between oscillation marks, austenite grain size and transverse surface cracks in continuously cast steel slabs. Journal, Proceedings of The first Australia-China-Japan Symposium on Iron and Steelmaking, Northeastern University, Shenyang, China, (2006)
34. Brimacombe, J.K. and K. Sorimachi. Crack formation in the continuous casting of steel. Metallurgical Transactions B: Process Metallurgy 8B, 489-505 (1977).
35. McPherson, N.A. and A. McLean. Journal, ISS, Continuous Casting, Warrendale, PA, (1977)
36. Maehara, Y., K. Yasumoto, Y. Sugitani, and K. Gunji. Effect of carbon on hot ductility of as-cast low alloy steels. Transactions of the Iron and Steel Institute of Japan 25, 1045-52 (1985).
37. Burke, J.E. and D. Turnbull. Recrystallization and grain growth. Progr. in Metal Phys. (Interscience Publishers Inc.) 3, 220-92 (1952).
38. Burke, J.E. Trans. Am. Inst. Min. 180, 73 (1949).
39. Smith, C.S. Grain shapes and other metallurgical applications in topology. Metal Interfaces (ASM, Cleveland), 65-113 (1952).
40. Hunderi, O. and N.J. Ryum. Mat. Sci. 15, 1104 (1980).
41. Atkinson, H.V. Theories of normal grain growth in pure single phase systems. Overview no. 65. Acta Metallurgica 36, 469-91 (1988).

42. Hillert, M. The theory of normal and abnormal grain growth. Acta Met. 13, 227-38 (1965).
43. Feltham, P. Grain growth in metals. Acta Met. 5, 97-105 (1957).
44. Greenwood, G.W. Growth of dispersed precipitates in solutions. Acta Met. 4, 243-8 (1956).
45. Louat, N.P. Theory of normal grain growth. Acta Metallurgica 22, 721-4 (1974).
46. Rhines, F.N., K.R. Craig, and R.T. DeHoff. Mechanism of steady-state grain growth in aluminum. Metallurgical Transactions 5, 413-25 (1974).
47. Doherty, R.D. Metall. Trans. A 6, 588 (1975).
48. Detert, K. Recrystallization of Metallic Materials (Dr. Riedrer-Verlag GmbH, Stuttgart (F. Haessner, ed.), 1978).
49. Gladman, T. Journal, Proc. Roy. Soc. Lond. A, 298, (1966)
50. Thompson, C.V., H.J. Frost, and F. Spaepen. The relative rates of secondary and normal grain growth. Acta Metallurgica 35, 887-90 (1987).
51. Beck, P.A., J.C. Kremer, L.J. Demer, and M.L. Holzeorth. Trans. Amer. Inst. Min. (Metall.) Engrs. 175, 372 (1948).
52. Mullins, W.W. The effect of thermal grooving on grain boundary motion. Acta Metallurgica 6, 414-427 (1958).
53. Phelan, D. and R. Dippenaar. Instability of the delta-ferrite/austenite interface in low carbon steels: The influence of delta-ferrite recovery sub-structures. ISIJ International 44, 414-421 (2004).
54. Phelan, D.J. and R. Dippenaar. Delta-ferrite recovery in low carbon steels. Metall. Trans. B 34, 495 (2003).
55. Liu, Z., Y. Kobayashi, J. Yang, K. Nagai, and M. Kuwabara. "In-situ" observation of the δ/γ phase transformation on the surface of low carbon steel containing phosphorus at various cooling rates. ISIJ International 46, 847-853 (2006).
56. Moon, S.C. The influence of austenite grain size on hot ductility of steels (School of Materials Engineering, University of Wollongong, 2003).
57. Mahapatra, R.B., J.K. Brimacombe, and I.V. Samarasekera. Mold behavior and its influence on quality in the continuous casting of steel slabs: Part II. Mold heat transfer, mold flux behavior, formation of oscillation marks, longitudinal off-corner depressions, and subsurface cracks. Metallurgical Transactions B: Process Metallurgy 22B, 875-88 (1991).
58. Herring, C. In Structure and Properties of Solid Surfaces ((eds Gomer, R. & Smith, C. S.) University of Chicago, 1952).
59. Adams, B.L., D. Kinderlehrer, W.W. Mullins, A.D. Rollett, and S. Ta'asan. Extracting the relative grain boundary free energy and mobility functions from the geometry of microstructures. Scripta Materialia 38, 531-536 (1998).
60. Reid, M., D.J. Phelan, and R. Dippenaar. Concentric solidification for high temperature laser scanning confocal microscopy. ISIJ International 44, 565-72 (2004).
61. Melfo, M. (University of Wollongong, Wollongong, 2006).
62. Vogel, R.Z. Chem. 126, 1 (1923).
63. Harker, D. and E.A. Parker. Trans. Amer. Soc. Met. 34, 156 (1945).
64. Miodownik, M.A. Grain boundary engineering with particles. Scripta Materialia 54, 993–997 (2006).